Summer 2018

Controlled drug delivery systems and integration into 3D printing

Anh-Vu Tran Do
University of Iowa

CONTROLLED DRUG DELIVERY SYSTEMS AND INTEGRATION INTO 3D PRINTING

by

Anh-Vu Tran Do

A thesis submitted in partial fulfillment
of the requirements for the Doctor of Philosophy
Degree in Chemical and Biochemical Engineering in the
Graduate College of
The University of Iowa

August 2018

Thesis Supervisor: Professor Aliasger K. Salem

Graduate College
The University of Iowa
Iowa City, Iowa

CERTIFICATE OF APPROVAL

PH.D. THESIS

This is to certify that the Ph.D. thesis of

Anh-Vu Tran Do

has been approved by the Examining Committee for
the thesis requirement for the Doctor of Philosophy Degree
in Chemical and Biochemical Engineering at the August 2018 graduation.

Thesis Committee: _____
Aliasger K. Salem, Thesis Supervisor

_____
Tonya Peeples

_____
Jonathan A. Doorn

_____
Liu Hong

_____
Ramprakash Govindarajan

To my loving family, my parents: Duyanh Do and Thom Tran and my brothers: Binh, Duc and Phiet Do

Perfection is not attainable, but if we chase perfection we can catch excellence.

- Vince Lombardi

ACKNOWLEDGEMENTS

As one of the most intensive and enjoyable endeavors that I have taken on thus far come to an end, my time as a doctoral student at the University of Iowa in Chemical and Biochemical Engineering would not have been possible without the support of my friends, family, colleagues, and professors. I am profoundly grateful and indebted to my advisor, Dr. Aliasger Salem, for his willingness to take a chance on me at the beginning of my graduate tenure and his never-ending support, guidance, and encouragement all the way until the end of my graduate studies. His unwavering encouragement and mentorship were contagious and helped to constantly set me up for success. I am truly thankful for the opportunities that Dr. Salem has afforded me and know that I would not be where I am today without his help in terms of my personal, professional, and academic development.

I would also like to thank my dissertation committee members Dr. Tonya Peeples, Dr. Liu Hong, Dr. Jonathan Doorn, and Dr. Ramprakash Govindarajan for their time and effort in helping provide guidance and feedback towards my doctoral milestones. A special thank you goes out to Dr. Sean Geary for being one of the best mentors that I could have ever asked for. My research would have been impossible without his invaluable help in all aspects of research. He was always available to help with any issues in the lab or my personal life and for that I am infinitely thankful for. A big thanks would also need to be given to Dr. Kristan Worthington for helping carry me towards the end of my graduate research. She provided me with an endless amount of support and advice and helped to play an integral part in the completion my thesis.

I would like to thank my former and current faculty members from the department of Chemical and Biochemical Engineering and the staff at Central

Microscopy Research Facility, especially Dr. Chantal Allamargot who offered valuable courses relevant to my research. I would like to acknowledge the Graduate College and The Center for Biocatalysis and Bioprocessing for providing me with funding for four years to allow me to pursue my own projects of working with 3D Printing.

My heartfelt thanks go to my family, who at times would provide the much needed inspiration for me to continue my graduate career. I want to thank my father, Duyanh Do, my mother, Thom Tran, and my brothers, Binh Do, Duc Do, and Phiet Do who provided me with endless support, love, and patience as I pursued this monumental milestone. I do not think I could have remained sane without the help from my friends, fellow graduate students and of course, my lab mates. They provided unending humorous banter to keep me going through my trial and tribulations with research. My mentors Dr. Vijaya Joshi and Dr. Amaraporn Wongrakpanich were essential in acclimating me in the field of pharmaceutical research. I want to thank my fellow graduate students, Brian Green, Benjamin King, and Michael Delcau who gave me an overwhelming amount of support throughout my 5 years. I would like to also thank Angie, Anh, Behnoush, Brittany, Cristina, Emad, Jaidev, Jib, Julianna, Kanawat Kareem, Kawther, Keerthi, Meow, Rasheid, Tip, Tim, Sandeep, Zach, Zaid, Youssef for being awesome friends and colleagues and helping to provide unlimited support/resources whenever I needed it.

My achievement as a graduate student, the research, the oral and poster presentations, the fellowships, and the publications would not have been possible without the help of the aforementioned people. As I finish my PhD degree, I am forever grateful to everyone who has played a vital role in shaping me into the scientist I am today and want to make sure these people are appreciated for their role in my life.

ABSTRACT

Controlled drug delivery systems have been utilized to enhance the therapeutic effects of many current drugs by effectively delivering drugs in a time-dependent and repeatable manner. The ability to control the delivery of drugs, whether through sequential, instantaneous, sustained, delayed and/or enhanced release has the potential to provide effective dosing regimens with enhanced therapeutic effects for a plethora of diseases and injuries. For instance, such systems can enhance anti-tumoral responses or, alternatively, promoting tissue regeneration. The current need for organ and tissue replacement, repair and regeneration for patients is continually growing such that supply is not meeting the high demand primarily due to a paucity of donors as well as biocompatibility issues that lead to immune rejection of the transplant. To overcome this problem, scientists working in the field of tissue engineering and regenerative medicine have investigated the use of scaffolds as an alternative to transplantation. These scaffolds are designed to mimic the extracellular matrix (ECM) by providing structural support as well as promoting attachment, proliferation, and differentiation with the goal of yielding functional tissues or organs.

Continued advancement and hybrid approaches using different material combinations and printing methodologies will further advance the progress of 3D printing technologies toward developing scaffolds, and other implantable drug delivery devices, capable of being utilized in the clinic. Such advancements will not only make inroads into improving structural integrity of implantable devices but will also provide platforms for controlled drug delivery from such devices. The primary focus of this thesis will be on controlled drug delivery as well as the integration of

controlled drug delivery into 3D printed devices aimed at promoting tissue regeneration.

We initially assessed the efficacy of a controlled drug delivery system for the treatment of cancer using on-demand, and sustained, release of an anticancer drug, doxorubicin (DOX), for the treatment of melanoma in a murine model. Using a melanoma model, we investigated the antitumor potential of combining ultrasound (US) with poly(lactic-co-glycolic acid) (PLGA) microspheres loaded with DOX. An *in vitro* release assay demonstrated an ability of US to affect the release kinetics of DOX from DOX-loaded PLGA microspheres by inducing a 12% increase in rate of release where this treatment resulted in synergistic tumor cell (B16-F10 melanoma cells) killing. Melanoma-bearing mice treated intratumorally with DOX (8 μg)-loaded microspheres and subjected to US treatment at the tumor site were shown to significantly extended survival compared to untreated mice or mice subjected to either treatment alone. The synergistic increase in survival of melanoma-challenged mice treated with the combination of US and DOX-loaded microspheres implicates a promising additional tool for combatting an otherwise currently incurable cancer.

We then further investigated other novel control drug delivery systems which included a 3D printed device (tube) for the purposes of sequential drug delivery. 3D printed hollow alginate tubes were fabricated through co-axial bioprinting and then injected with PLGA to provide sequential release of distinct fluorescent dyes (model drugs), where fluorescein was initially released from alginate followed by the delayed release (up to 55 h) of rhodamine B in PLGA. With an alginate shell and a PLGA core, the fabricated tubes showed no cytotoxicity when incubated with the human embryonic kidney (HEK293) cell line or bone marrow stromal stem cells (BMSC).

Microscale printing through two-photon polymerization (2PP) was then investigated for controlled drug delivery potential. Poly(ethylene glycol) dimethacrylate (PEGDMA) devices were fabricated using a Photonic Professional GT two-photon polymerization system while rhodamine B was homogenously entrapped inside the polymer matrix during photopolymerization. These devices were printed with varying porosity and morphology and using varying printing parameters such as slicing and hatching distance. Overall, tuning the hatching distance, slicing distance, and pore size of the fabricated devices provided control of rhodamine B release due to resulting changes in the motility of the small molecule and its access to structure edges. In general, increased spacing provided higher drug release while smaller spacing resulted in some occlusion, preventing media infiltration and thus resulting in reduced drug release. 2PP was further explored for its ability to tailor topographical cues in addition to controlled drug release. These physical cues, similar to those of the ECM, have been seen to promote differentiation. With 2PP, we explored microscale topographies with nanoscale precision, where different star size topographies were fabricated. It was observed that the smallest star size topographies differentiated human iPSCs towards the endoderm and mesoderm germ layer.

Integrating the facility for controlled drug release into 3D printed devices provides a demand for constructs that not only need to fulfill their purpose of temporarily substituting for the missing tissue at the site of injury, but also providing the necessary cues to promote appropriate tissue regeneration. With 3D printing technology, novel drug delivery constructs were fabricated and tested to appraise functionality such as the ability to control drug delivery and the ability to function as a non-toxic medium for cellular attachment, proliferation, and forced differentiation.

PUBLIC ABSTRACT

Controlled drug delivery systems have been utilized to enhance the therapeutic effects of many current drugs by effectively delivering drugs in a time-dependent and repeatable manner. The ability to control the delivery of drugs, whether through sequential, instantaneous, sustained, delayed and/or enhanced release has the potential to provide effective dosing regimens with enhanced therapeutic effects for a plethora of diseases and injuries. For instance, such systems are capable of enhancing anti-tumoral responses or, alternatively, promoting tissue regeneration. The need for organ and tissue replacement, repair and regeneration for patients is continually growing such that supply is not meeting the high demand primarily due to a paucity of donors as well as biocompatibility issues that lead to immune rejection of the transplant. In an effort to overcome this problem, scientists working in the field of tissue engineering and regenerative medicine have investigated the use of scaffolds as an alternative to transplantation. These scaffolds are designed to mimic the natural tissue environment by providing structural support as well as promoting cellular attachment, growth, and maturation with the ultimate goal of yielding functional tissues or organs. With the emergence and continued advancement of 3D printing technologies, the fabrication of various constructs and devices to tailor the drug delivery criteria for personalized medicine becomes more feasible. Such advancements will not only make inroads into improving structural integrity of implantable devices but will also provide platforms for controlled drug delivery from such devices.

The need for the delivery of these cues has led to attempts to design devices with the capacity to release the necessary drugs in a controlled manner in order to

elicit effective therapeutic effects. To test for the effects of controlled drug delivery systems, we initially utilized controlled drug delivery systems for the treatment of cancer through on-demand and sustained release of an anticancer drug for the treatment of melanoma. These systems led us to further investigate more novel controlled drug delivery systems compared to conventional microparticle controlled drug delivery. Bioprinting and stereolithographic 3D printing was investigated for potential controlled drug delivery due to their prevalence in tissue engineering and disease application. With the aid of 3D printing technology, novel drug delivery constructs were fabricated and tested to appraise functionality such as the ability to control drug delivery and the ability to function as a non-toxic medium for cellular attachment, growth, and maturation. Through careful designs and printing parameter manipulations, 3D printing technologies were able to provide sustained and sequential drug release along with the ability to promote maturation through topographical cues. The primary focus of this thesis will be on controlled drug delivery as well as the integration of controlled drug delivery into 3D printed devices aimed at promoting tissue regeneration.

TABLE OF CONTENTS

LIST OF TABLES xiii

LIST OF FIGURES xiv

LIST OF ABBREVIATIONS xix

PREFACE xxi

CHAPTER 1 : INTRODUCTION 1

Background 6
Controlled drug release 6
Conventional vs. current 3D printing 9
Materials used for 3D printing of scaffolds 12
3D Printing techniques for scaffold fabrication 14
Computer aided design and digital imaging 16
Direct 3D printing 18
Bioprinting 20
Stereolithography (SLA) 23

Research Objective 30

Rationale and Specific Aims 30

CHAPTER 2 : COMBINING ULTRASOUND AND INTRATUMORAL ADMINISTRATION OF DOXORUBICIN-LOADED MICROSPHERES TO ENHANCE TUMOR CELL KILLING 33

Introduction 33
Poly(lactic-co-glycolic acid) (PLGA) 35
Melanoma 37

Materials and Methods 41
Microsphere fabrication 41
Determining size, DOX-loading, and DOX-loading efficiency of PLGA microspheres 42
Device configuration for US generation 42
Ultra-morphology of blank particles after the application of US 43
Evaluating the effect of blank and DOX-loaded microspheres plus US on cell viability 46
Cell lines and cell culture 46
Assessing the effect of blank and DOX-loaded microspheres plus US on cell viability in vitro 46
US/DOX-loaded microsphere treatment of tumor challenged mice 47
Data Analysis 48

Results 49
Characterization of DOX-loaded and blank microspheres 49
Evaluation of US effects on ultra-morphology of blank microspheres 49

Effect of US on the drug release profile of DOX-loaded microspheres 52
Effect of the combination of US and DOX-loaded microspheres on killing melanoma cells in vitro 54
Effect of the combination of US and DOX-loaded microspheres on survival in a mouse melanoma model 56
Discussion 60
Conclusion 64

CHAPTER 3 : CONTROLLED AND SEQUENTIAL DELIVERY OF FLUOROPHORES FROM 3D PRINTED ALGINATE-PLGA TUBES 67
Introduction 67
Sodium alginate 69
Materials and Methods 71
Alginate-PLGA tube fabrication 71
Morphology imaging of alginate-PLGA tube 74
Fluorophore release study 74
Individual release of fluorophore from polymers 76
Evaluating cell viability and cytotoxicity 77
Cell lines and cell culture 77
Evaluation of Alginate-PLGA Tubes on Cell Viability 77
Mechanical analysis 78
Data analysis 78
Results 79
Visualization and dimensions of alginate-PLGA tubes 79
Release kinetics of fluorophores from alginate-PLGA tubes 80
Cytotoxicity of alginate-PLGA tube 82
Compression moduli of alginate-PLGA tubes 83
Discussion 84
Conclusion 86

CHAPTER 4 : CONTROLLED DRUG DELIVERY FROM 3D TWO-PHOTON POLYMERIZED POLY(ETHYLENE GLYCOL) DIMETHACRYLATE DEVICES 88
Introduction 88
Poly(ethylene glycol) dimethacrylate 91
Materials and Methods 92
Device design 92
Device fabrication 93
Device morphology 95
Release of rhodamine B 95
PEGDMA biocompatibilty 98
Statistical analysis 99
Results and Discussion 100
Cylinder diameter 100

Cylinder spacing 104
Slicing and hatching distance 105
PEGDMA biocompatibility 111
Conclusion 112
CHAPTER 5 : TWO-PHOTON POLYMERIZATION OF TOPOLOGICAL CUES FOR HUMAN IPSC DIFFERENTIATION 114
Introduction 114
Materials and Methods 118
Topography design 118
Two-photon polymerization 119
Topography characterization 120
Topography preparation 120
Cell culture and seeding 121
Material cytotoxicity 123
Gene expression 124
Cellular differentiation analysis and statistical analysis 125
Results and Discussion 126
Characterization of topography using SEM and AFM 127
Cellular differentiation from topological cues 128
Conclusion 138
CHAPTER 6 : CONCLUSION AND FUTURE DIRECTIONS 139
REFERENCES 144

LIST OF TABLES

Table 1-1 : Table summarizing preclinical progress of 3D printing techniques used to print scaffolds for tissue engineering. 28

Table 2-1 : Mean survival times for tumor-challenged mice receiving indicated treatment. 59

Table 4-1 : Design parameters for two-photon polymerized PEGDMA woodpile and cuboid devices. 94

Table 5-1 : Specifications for the varying shapes at constant size. 119

Table 5-2 : Gene expression fold change averages for each germ layer compared to the pluripotent scorecard control. 135

Table 5-3 : Gene expression fold change averages for each germ layer compared to the glass control. 136

Table 5-4 : Target name and their gene names. 137

LIST OF FIGURES

Figure 1-1 : Schematic of direct 3D printing of a CAD scaffold. Adapted from "Porous scaffold design for tissue engineering" by Scott Hollister, Nature Materials 2005, 4, 518.[20] 20

Figure 1-2 : Schematic of bioprinting printer set-up. 21

Figure 1-3 : Schematic of stereolithographical technique for manufacturing scaffolds. Adapted from "Porous scaffold design for tissue engineering" by Scott Hollister, Nature Materials 2005, 4, 518.[20] 24

Figure 2-1 : Chemical structure of poly(lactic-co-glycolic acid) polymer. 37

Figure 2-2 : US generation instrument set up. 43

Figure 2-3 : Schematic of the application of US to blank microspheres. 45

Figure 2-4 : US-mediated damage to the surface of PLGA microspheres. (A-F) SEM images of blank PLGA microspheres either untreated (A,B), or treated with US without degassing (C,D) or with degassing (E,F). (G) Graph illustrating the percent of particles displaying surface damage (E). **** $p < 0.0001$. Error bars represent standard deviation of the mean. 51

Figure 2-5 : Cumulative release of DOX from DOX-loaded particles with or without US exposure. US was either applied or not applied to DOX-loaded microspheres (loading of 1.94 µg DOX/mg PLGA microspheres), as described in the methods section "Ultra-morphology of blank particles after the application of US". A) Release was subsequently monitored over the indicated time period and showed an enhance burst release of 6% (3 h) and a total increase in 12% over the span of the release study (1008 h). B) Pooled data from 2 experiments ($n = 13$) comparing percent release DOX from US treated and non-treated microspheres at $t = 3$ h. *** $p < 0.001$. Error bars represent standard deviation of the mean. Also shown are curves of best fit based on the extra sum-of-squares F-test. * $p < 0.05$. 53

Figure 2-6 : Cell viability of B16-F10 cells treated with particles (w/wo DOX) and/or US. Cells were subjected to treatment and incubated for 48h prior to analysis by counting (see methods section "Assessing the effect of blank and DOX-loaded microspheres plus US on cell viability in vitro"). Statistical analysis was performed using one-way ANOVA with a Tukey's multiple comparison test and showed statistical significance between all groups (only a selection is indicated) except for US vs. blank microspheres and US vs. DOX-loaded microspheres. ($n = 4$, ** $p < 0.01$, **** $p < 0.0001$). Error bars represent standard deviation of the mean. 55

Figure 2-7 : Survival study of in vivo tumor therapy. A) Tumor challenge and treatment regimen. B) Survival curve (pooled data) of tumor (B16-F10) challenged mice that received the following treatments on indicated days: PBS only (n = 14), PBS + US (n = 18), blank particles + US (n = 15), DOX-loaded particles (4 μg) alone (n = 9), DOX-loaded particles (2 μg) + US (n = 5), DOX-loaded particles (4 μg) + US (n = 10), and DOX-loaded particles (8 μg) alone (n = 5), DOX-loaded particles (8 μg) + US (n = 15). A Mantel-Cox test was performed to analyze the survival distribution yielding a p-value of 0.0110. This global significance was then followed by a Tukey-Kramer post-test with multiple comparisons * $p < 0.05$, ** $p < 0.01$, *** $p < 0.001$. C) Survival curve comparing mice treated with DOX-loaded particles (8 μg) + US and/or anti-PD1, where all anti-PD1 groups were n = 5. 59

Figure 3-1 : Chemical structure of sodium alginate. 71

Figure 3-2 : Schematic of the extrusion printing systems. A) Schematic of the coaxial extrusion printing system utilizing a mechanical pump to extrude sodium alginate (blue fluid) and a dispensing unit to introduce $CaCl_2$ (yellow fluid). B) Illustration of the coaxial nozzle used to print alginate conduits tubes, where the hydrogel flow contains the sodium alginate and $CaCl_2$ solutions in the sheath and core sections, respectively. 73

Figure 3-3 : Degradation curves for: A) fluorescein (λex494, λem521) and B) rhodamine B (λex540, λem625). 76

Figure 3-4 : Images of 3D printed alginate-PLGA tubes. A) A photograph of an alginate-PLGA tube. B) A light microscope image of an alginate-PLGA tube with the alginate sheath and PLGA core indicated with arrows. C) A light microscope image (clear shell showing alginate, light-purple core showing PLGA containing rhodamine) of an alginate-PLGA tube B). D) A SEM image of alginate-PLGA tube. 80

Figure 3-5 : Cumulative release from alginate-PLGA tubes. Tubes had varying fluorescent dye and material composition with A) alginate-PLGA tubes containing 0.8 mg/ml of rhodamine B in the PLGA core and 0.025 mg/ml of fluorescein in the alginate sheath (n = 3) and B) alginate-PLGA tubes containing 0.4 mg/ml of rhodamine B in the PLGA core and 0.025 mg/ml of fluorescein in the alginate sheath (n = 3). 81

Figure 3-6 : Cumulative release of individual composition of fluorophore and polymer. Cumulative release of fluorophores from: A) PLGA loaded with fluorescein (0.025 mg/ml), B) PLGA loaded with rhodamine B (0.8 mg/ml), C) alginate loaded with fluorescein (0.025 mg/ml), and D) alginate loaded with rhodamine B (0.8 mg/ml) (n = 4 for A, B and C). 82

Figure 3-7 : Cell viability assays: A) HEK293 or B) BMSCs were incubated with alginate- PLGA tubes of indicated varying lengths. Statistical analysis was performed using one-way ANOVA with Dunnett's multiple comparison test at n = 4 (* signifies p < 0.05, ** p < 0.01).....83

Figure 3-8 : Compression moduli of coaxial extrusion printed tubes. The moduli of blank alginate-PLGA tubes, alginate-PLGA tubes loaded with 0.025 mg/ml fluorescein (in alginate) and 0.80 mg/ml (R1) or 0.40 mg/ml (R2) rhodamine B (in PLGA), and alginate tubes alone were measured through a dynamic mechanical analyzer. Statistical analysis was carried out using one-way ANOVA with Dunnett's multiple comparison test at n=4 (* signifies p<0.05, ** p<0.01, and *** p<0.001).....84

Figure 4-1 : Chemical structure of Poly(ethylene glycol) dimethacrylate. 92

Figure 4-2 : Method of detecting release from 2PP PEDMA scaffolds. A) Image of scaffolds taken from the EVOS microscope depicting slicing, hatching, and cylinder size with their respective change in distance and cylinder sizes from 2PP at 10% intensity and 15 ms using an EVOS RFP light cube. B) Control samples of PEGDMA without rhodamine B at 10% intensity and 15 ms, (no fluorescence detected). C) An example of the loss of fluorescence of a single scaffold over time (0-48 h). Full sets of scaffolds have a scale bar of 400 µm (A, B), while single scaffolds have a scale bar of 200 µm (C)...96

Figure 4-3 : Standard curve of rhodamine B concentrations loaded on PEGDMA printed 5mm discs. A standard curve was constructed from printed PEGDMA discs containing different concentrations of rhodamine B (n=3).....98

Figure 4-4 : Effect of cylinder size on rhodamine release from 2PP woodpile structures. A-C: 3D models of woodpile structures with designed cylinder diameters and cylinder spacing of 5, 10 or 15 µm, respectively. D-F: Representative scanning electron micrographs of the corresponding poly(ethylene glycol) woodpile structures. Scale bars represent 25 µm. G: Release profiles (data points) and best-fit non-linear regression curves (lines) of rhodamine B diffusion from the devices shown in A-F. Error bars represent standard error of the mean; significance denoted is based on comparison of non-linear regression parameters, ***p < 0.001 (n=6). 103

Figure 4-5 : Effect of cylinder spacing on rhodamine B release from 2PP woodpile structures. A-B: 3D models of woodpile structures with designed space between cylinders of 5 or 9.29 μm, respectively, with constant cylinder diameter of 5 μm. C-D: Representative scanning electron micrographs of the corresponding PEGDMA woodpile structures. Scale bars represent 25 μm. E: Release profiles (data points) and best-fit non-linear regression curves (lines) of rhodamine B diffusion from the devices shown in A-D. Error bars represent standard error of the mean; significance denoted is based on comparison of non-linear regression parameters, ***p < 0.001 (n=6). 105

Figure 4-6 : Effect of slicing and hatching distance on rhodamine B release from 2PP cuboid structures. A: 3D model of cuboid structure. B: Representative scanning electron micrograph of the corresponding poly(ethylene glycol) cuboid structure. Scale bar represents 25 μm. C-D: Release profiles (data points) and best-fit non-linear regression curves (lines) of rhodamine B diffusion from cuboid devices with varying slicing or hatching distance, respectively. Error bars represent standard error of the mean; significance denoted is based on comparison of non-linear regression parameters, **p < 0.01 and ***p < 0.001 (n=3). 108

Figure 4-7 : Effect of slicing and hatching distance on rhodamine B release from 2PP woodpile structures. A-F: Representative scanning electron micrographs of PEGDMA woodpile structures with 10 μm cylinders created using a slicing distance of 0.05, 0.1 or 0.15 μm at constant hatching distance or a hatching distance of 0.05, 0.1 or 0.15 μm at a constant slicing distance, respectively. Scale bars represent 25 μm. G-H: Release profiles (data points) and best-fit non-linear regression curves (lines) of rhodamine B diffusion from the devices shown in A-F with varying slicing (G) or hatching (H) distances. Error bars represent standard error of the mean; no significant differences between non-linear regression parameters were detected (n=3). 110

Figure 4-8 : Biocompatibility of photopolymerized poly(ethylene glycol). The viability of human embryonic kidney cells (HEK293), bone marrow stromal stem cells (BMSC) or mouse induced pluripotent stem cells (iPSC) was analyzed through an MTS assay after 24h of incubation in "conditioned" media. The cells were incubated with "conditioned" media that was made by incubating photopolymerized poly(ethylene glycol) dimethacrylate samples in cell culture media for 24 h . Error bars represent standard deviation (n=4). 112

Figure 5-1 : Biocompatibility of photopolymerized photoresist. Cell viabilities of iPSCs incubated with conditioned media that was incubated for 1 through 7 days with 2PP printed photoresist in differentiation media. Error bar represents standard deviation (n= 4). 127

Figure 5-2 : SEM (A-B, D-E, G-H) and AFM (C, F, I) images of topographical arrays of stars with varying size. Scale bars in A-B, D-E and G-H represent 30 μm, with inset scale bars representing 2 μm. Scale bars in C, F and I represent 6 μm and the color corresponds to the sample height, as shown in the scale.....128

Figure 5-3 : Germ layer gene expression of cells grown on topographies consisting of different sized stars. Human iPSCs were incubated with varying size topographies and analyzed using a TaqMan hPSC Scorecard to determine germ layer gene expression. A) Self-renewal, B) Ectoderm, C) Mesoderm, and D) Endoderm differentiation were analyzed and samples were compared to the internal standard of the pluripotent scorecard control which was normalized to a value of 1. Groups of genes expressed above a 2-fold change were considered to be upregulated while expression below a 0.5-fold change was considered as down regulation of the group of genes. Samples were graphed based upon gene expression filtration (method Cellular differentiation analysis and statistical analysis). Wilcoxon Signed Rank test showed statistical significance in the mesoderm and endoderm gene groups. * $p < 0.05$, ** $p < 0.01$, ****$p < 0.0001$. Error bars represent standard deviation.....133

Figure 5-4 : Germ layer gene expression of cells grown on topographies with different sized stars. Human iPSCs were incubated with varying sized topographies and analyzed using a TaqMan hPSC Scorecard to determine germ layer gene expression. A) Self-renewal, B) Ectoderm, C) Mesoderm, and D) Endoderm differentiation were analyzed and samples were compared to glass control, which were normalized to a value of 1. Groups of genes expressed above a 2-fold change were considered to be upregulated while expression below a 0.5-fold change was considered as down regulation of the group of genes. Samples were graphed based upon gene expression filtration (method Cellular differentiation analysis and statistical analysis). Error bars represent standard deviation.....134

LIST OF ABBREVIATIONS

2PP:	Two-Photon Polymerization
AFM:	Atomic Force Micrographs
B16-F10:	B16-F10 Melanoma Cells
BMP-2:	Bone Morphogenetic Protein 2
BMSC:	Bone Marrow Stromal Cells
CAD:	Computer Aided Designs
CT:	Computer Tomography
DCM:	Dichloromethane
DMEM:	Dulbecco's Modified Eagle's medium
DOX:	Doxorubicin
ECM:	Extracellular Matrix
FBS:	Fetal Bovine Serum
FDA:	Food & Drug Administration
HEK293:	Human Embryonic Kidney 293
hiPSC:	human induced Pluripotent Stem Cells
hPSC:	Human Pluripotent Stem Cells
iPSC:	induced Pluripotent Stem Cells
MiPSCs:	Murine Induced Pluripotent Stem Cells
MRI:	Magnetic Resonance Imaging
PBS:	Phosphate Buffered Saline
PCL:	Poly(e-caprolactone)
PD-1:	anti- Programmed Cell Death Protein-1
PDGF:	Platelet-Derived Growth Factor
PD-L1:	Anti Programmed Cell Death Ligand 1
PEG:	Polyethylene Glycol
PEGDMA:	Poly(ethylene glycol) dimethacrylate
PLGA:	Poly (lactic-co-glycolic acid)

PLGA:	Poly(lactic-co-glycolic acid)
PVA:	Poly (vinyl alcohol)
RPM:	Revolutions Per Minute
SA/HA	Sodium Alginate/Hydroxyapatite
SC:	Subcutaneous
SD:	Standard Deviation
SE:	Standard Error
SEM:	Scanning Electron Microscopic
SLA:	Stereolithography
US:	Ultrasound
VEGF:	Vascular Endothelial Growth Factor

PREFACE

Publications from this thesis research:

1. Do, A. V.; Geary, S. M.; Seol, D.; Tobias, P.; Carlsen, D.; Leelakanok, N.; Martin, J. A.; Salem, A. K., Combining Ultrasound and Intratumoral Administration of Doxorubicin-loaded Microspheres to Enhance Tumor Cell Killing. International Journal of Pharmaceutics 2018, 539 (1-2), 139-146.
2. Do, A.-V.; Akkouch, A.; Green, B.; Ozbolat, I.; Debabneh, A.; Geary, S.; Salem, A. K., Controlled and Sequential Delivery of Fluorophores from 3D Printed Alginate-PLGA Tubes. Annals of Biomedical Engineering 2017, 45 (1), 297-305.
3. Do, A.V and Worthington K.; Tucker B.; Salem A.K., Controlled Drug Delivery from 3D Two-Photon Polymerized Poly (Ethylene Glycol) Dimethacrylate Devices.(Submitted to Journal of Controlled Release)
4. Do, A.V; Tucker B.;Salem A.K.; Worthington K. Two-Photon Polymerization of Topological Cues for Human iPSC Differentiation. (In Preparation)

CHAPTER 1 : INTRODUCTION

Controlled drug release systems were developed to overcome many problems currently faced by conventional methods, including toxicity, lack of patient compliance, high financial costs, and excessively rapid liver and renal clearance.[1-3] Controlled drug release systems are designed to provide predetermined drug release rates so as to provide optimal efficacy with minimal side-effects. Thus drug levels can be maintained within a desired range whether it be a constant dose over time (sustained); cyclical, where the release of drug is regularly repeated following a lag time (pulsatile); differential, where the two or more drugs can be delivered at different times (sequential), or instantaneous release that is often triggered by external events (on-demand).[4-5] Regardless of the type of controlled release utilized, these approaches affecting drug release have allowed modern medicine to provide more effective dosage regimens. Not only do these systems increase the effectiveness and cost of current drugs, they help to address many patient compliance/adherence issues involving forgetfulness[6], complicated dosage schedules (e.g. warfarin)[7], and inability to physically access the drugs (rheumatoid arthritis).[8] Controlled drug delivery systems have been successful in many different applications but there has been limited studies to investigate the effects of controlled drug delivery systems in 3D printing. The integration of controlled drug delivery systems into 3D printing may provide a versatile tool in not only fabricating constructs capable of promoting higher levels of tissue regeneration but also creating drug-loaded implants for various disease applications.

Each year, the number of people in the United States suffering from organ dysfunction or organ failure due to damaged or diseased tissue is increasing because

of the aging population.[9] Illnesses or traumas, such as heart attacks[10], strokes[11], and joint degeneration[12] can drastically reduce the quality of life for the victims as well as causing levels of tissue damage that current medicine is incapable of adequately repairing. This lack of therapeutic efficacy is primarily due to the fact that current treatments are aimed at merely preventing or reducing further tissue damage rather than contributing to the repair or regeneration of the tissue. Medications such as anticoagulants (warfarin) and antiplatelet agents (aspirin) for heart attacks and strokes primarily function to prevent blood clots and do not contribute to any form of tissue regeneration.[13] Similarly, analgesics, such as acetaminophen (paracetamol)[14] and nonsteroidal anti-inflammatory drugs (e.g. aspirin and ibuprofen)[15], are given to patients suffering from osteoarthritis (degenerative joint disease) primarily for pain relief, and play a limited role in tissue regeneration/repair. As a result, patients are obliged to live with chronically damaged tissues which leads to a lower quality of life and contributes to an increased healthcare cost.[16] The aim of regenerative medicine is to restore or replace damaged or diseased tissues with healthy, functioning tissue. Tissue engineering requires an understanding of the biological processes required for cellular proliferation and differentiation.[17-20] The process of tissue engineering often begins with a scaffold, which is a three-dimensional support medium essential for the appropriate proliferation and differentiation of cells embedded in, or infiltrating, the scaffold. Tissue engineering provides a potential solution to drastically reduce the demand for tissues and organs. However, there are still major issues that must be addressed to ensure the feasibility of tissue engineering. These include: creating materials for cell transplantation; preservation of tissues and cells for long term storage; inducing blood vessel and nerve growth; and preventing tissue rejection.[21-22]

In efforts to address these issues, it is important to understand the properties of the materials used to print scaffolds and how they affect the behavior of cells infiltrating into, or seeded within, the scaffold; as well as their effects on growth factor/drug release kinetics and how this affects cell behavior. Improved understanding of these dynamic processes will help guide us in manipulating each component for optimal tissue regeneration. The key materials and tools for effective tissue engineering are cells, scaffolds, and growth factors.[22] Through modular cellular manipulation and continued advancement in stem cell research such as the use of induced pluripotent stem cells (iPSC)[21, 23], tissue engineering has been able to make great forward strides in terms of helping to combat immune rejection.[24] In regards to growth factors, researchers are establishing paradigms for which the incorporation of growth factors into scaffolds are required to aid in the differentiation of stem cells to a desired tissue type. For example, researchers employed scaffolds to provide controlled drug delivery of insulin-like growth factor-1 and transforming growth factor-β1 for optimal tissue regeneration of cartilage.[25-26]

3D printing technologies for scaffolding have fielded the interests of many scientists specializing in tissue engineering. The ideal role of 3D printing in tissue engineering is to fabricate a device (e.g. scaffold) that provides a microenvironment that mimics the intricate properties of the native extracellular matrix (ECM) and thereby favors the regulated development of infiltrating, or seeded, stem cells dedicated to the generation of a specific tissue type. It is important that scaffolds mimic the ECM as closely as possible in order to create a microenvironment conducive to optimal tissue regeneration.[27-29] The ECM is responsible for directing basic cellular functions such as migration, proliferation and differentiation, which are

all vital for effective tissue formation.[30] The advancement and creation of 3D printing technologies have provided researchers with a tool to create intricate replicable scaffolds that are capable of incorporating stem cells and growth factors, thus potentiating an improved mode of tissue regeneration.[31] The successes of 3D printing has been seen preclinically and the transition towards clinical based studies are already underway (**Table 1-1**).[32-33] In efforts to advance the versatility of 3D printed systems, the incorporation of controlled drug release properties is one important factor that may enhance rates or tissue regeneration for a range of implants targeting different diseases. The advancements in controlled drug delivery technologies are currently being employed to redefine conventional delivery systems to create more efficacious therapeutic responses.[34] The different drug technologies that will be focused on for the purposes of this proposal include sequential, sustained, and on-demand release. The approach to accomplishing the desired delivery will be dependent upon a number of factors including the chemical properties of the drug and polymer carrier complex, as well as the route of drug administration. Whilst all aspects of tissue engineering are important and need continual improvements [32, 35-36], the focus of this research is on the use of standard 3D printing technologies, such as bioprinting, and stereolithography by two-photon polymerization (2PP), and materials selected for the purposes of controlled drug delivery.

Our initial attempt at implementing a controlled drug release system was to utilize Poly (lactic-co-glycolic acid) (PLGA) microspheres for the delivery of the anticancer drug, doxorubicin, for the treatment of melanoma through ultrasound triggered release. We then further investigated more novel forms of controlled drug

delivery, using 3D printing in proof-of-principle studies, aimed towards generating scaffolds for tissue engineering or implants for drug delivery. In order to assess the feasibility of controlled drug delivery systems derived from 3D printing technology, we first designed constructs (comprising a PLGA core and a 3D printed alginate shell), using bioprinting, with the capability of sequential drug release. We then investigated 2PP 3D printing to understand controlled drug release on the microscale level in a proof of concept study by manipulating common printing parameters such as hatching, slicing, and spacing. The results would help to correlate 3D printing settings to controllable drug release, where previous work has demonstrated that, for any given material chemistry, the structural outcomes of 2PP devices are highly dependent on selected 2PP parameters, such as slicing and hatching distance. Parameters were chosen due to their prevalence in fabricated structures, where hatching (distance between individual lines), slicing (distance between vertical layers), and spacing are often changed to ensure that the final structures closely matched what was designed. With the ability to print with nanoscale precision, 2PP was utilized to investigate the roles of microscale printed surface topographies with varying shapes and sizes on cellular differentiation. The results of these experiments will provide additional tools for the advancement of tissue engineering using 3D printing.

This chapter aims to introduce controlled drug delivery systems with a strong emphasis on different aspects of 3D printing technologies. Future chapters will discuss the aforementioned experiments in greater detail as well as elaborate on the properties and rationale for using certain materials, such as PLGA, and PEGDMA.

BACKGROUND

Controlled drug release

Controlled drug delivery is a term that can apply to any formulation or device that has been designed to influence the timing and/or rate of drug release. Current and past research has aimed to understand and fabricate devices capable of different drug delivery mechanisms: 1) sequential, 2) sustained, and 3) on-demand drug release for the purposes of controlled drug releases. These drug delivery programs aim to provide more efficient therapeutic effects than current conventional treatment modalities by delivering the drug(s) in a more controlled fashion. The process of sequential drug delivery involves the release of an initial drug at a defined rate followed by the delayed release of a second drug preferably at, once again, a defined rate. In a sustained drug release system, the extended period of effective drug delivery helps to reduce the number of administrations which has the advantage of increasing patient compliance. On-demand drug delivery is an important release mechanism capable of providing a triggered release of drugs or molecules to combat certain side effects, such as pain, or to provide a more robust effect as needed, such as increasing insulin dosages based on blood glucose fluctuations. For this instance, the on-demand release system offers an advantage over sustained or pulsatile drug releasing implants. However, a desirable system would be one that would be able to release insulin in response to the patient's blood glucose level, which has not yet been effectively formulated.[4] The release may be triggered through various means such as pH change, infrared radiation, magnetic fields, or ultrasound. Such triggers disrupt film layers or polymer composition to allow for the enhanced release of the

desired drug. These release profiles can be combined in any iteration to form more complex release profiles for personalized medicine.

Sequential release utilizes a temporal dependence on when the drugs are released, where, as previously discussed, the release mechanism works by initially releasing a drug that is then followed by a delayed release of another drug. Sequential release has been demonstrated using titania nanotubes and polymer micelles to sequentially deliver both hydrophobic (indomethacin and itraconazole) and hydrophilic (gentamicin) drugs.[37] Sequential drug release has also been seen in the treatment of breast cancer where it has been reported that treating estrogen receptor-positive breast cancer cells with ibandronate before tamoxifen was 1.6-fold more effective than summing the effects of either drug alone, in terms of prohibiting cell growth.[38] Thus, a synergistic effect can be obtained through sequential release. Sustained drug release involves continuous release of a drug maintained at a constant drug concentration over a specific period of time in order to obtain a prolonged effect. Sustained drug delivery has been an important drug delivery system for the treatment of ocular pathologies since current treatment modalities suffer from a range of disadvantages that may include: poor uptake, systemic side effects, and poor patient adherence to the therapy. Intravitreal injections can help to enhance ocular drug delivery but the required repeated administration and potential injection-related side effects limits the utility of this technique.[39] Sustained release from intraocular implants demonstrated the ability to deliver ganciclovir as an alternative treatment for cytomegalovirus retinitis in patients with the acquired immunodeficiency syndrome. The ganciclovir tablet coated with polyvinyl alcohol, which is permeable to ganciclovir, was able to be more effective in treating

cytomegalovirus retinitis compared to intravenously delivered ganciclovir.[40] In another study, the sustained release of doxorubicin and CpG oligodeoxynucleotides from intratumorally administered PLGA particles yielded enhanced T cell responses leading to tumor-free mice.[41]

In a separate study, on-demand release of doxorubicin was accomplished in the form of magnetothermally responsive doxorubicin encapsulated supramolecular magnetic nanoparticles, where the application of an alternating magnetic field released doses of doxorubicin.[42] This triggered release of doxorubicin greatly reduced the colon tumors in mice compared to PBS and alternating magnetic fields alone.[42] In terms of tissue regeneration, the rapid formation of mature vascular networks was possible with the dual delivery of vascular endothelial growth factor (VEGF) and platelet-derived growth factor (PDGF), with distinct release kinetics, from a single polymer scaffold. In Lewis rats and non-obese diabetic mice, the PLGA scaffold was able to provide dual, sustained release of VEGF and PDGF to yield larger blood vessel areas and induce the maturation of mural cells more efficiently when compared to bolus administration of one or both proteins.[43] In another study, the Mooney group explored other methods of controlled drug release for the purposes of blood vessel formation, using a bilayer PLGA scaffold that was designed to release VEGF locally in one spatial region and then sequentially deliver VEGF and PDGF in an adjacent region. This delivery system helped to grow larger and more mature blood vessels compared to either treatment alone in SCID mice. It was reported that the size and maturation of the vessels were enhanced and dependent on the delivery of PDGF.[44] In a similar study, zonal release was shown to have concentrated levels of alkaline phosphatase within rhBMP-2 loaded microparticle zones. These scaffolds were

fabricated by sintering PLA microparticles plasticized with PEG to form scaffolds with layers varying according to whether or not they incorporated proteins, thus restricting the release of different bioactive molecules to specific regions within the scaffolds.[45] Thus, taking advantage of new and current drug delivery systems and biomaterial science, and incorporating them into 3D printed scaffolds to act as biometric, programmable and multidrug delivery devices will help to advance the versatility and efficacy of 3D printed systems.

Conventional vs. current 3D printing

Conventional techniques for scaffolding provided the first attempts at creating biomimetic scaffolds capable of tissue regenerations and it is from their shortcomings that have allowed for the need and creation of 3D printing technologies. Conventional techniques used for scaffold fabrication include solvent-casting particulate-leaching, gas foaming, fiber meshes/fiber bonding, phase separation, melt molding, emulsion freeze drying, solution casting, as well as freeze drying, and these are discussed further elsewhere.[46-47] However, the need for more replicable and biocompatible scaffolds for the purposes of tissue engineering have made some of these techniques outdated. These conventional methods have many limitations since they are often inadequate at fabricating precise pore size, pore geometry, high levels of interconnectivity, and high mechanical strength.[46-47] Other limitations of these conventional techniques also include suboptimal distribution of cells due to the inaccuracies inherent in the process of seeding cells manually. This becomes problematic since cells may need to be precisely arranged according to the need and function of the tissue such as endothelial cells aligning to form vessels, or

osteoblasts forming mineralized clusters.[47] For example, in melt molding, a finely powdered polymer is mixed with a porogen (removable particulates used to make pores), and is heated in a mold past the glass transition point. A physically cross-linked polymer is formed to the dimensions of the mold and the porosity can be controlled by varying the size and concentration of the porogens.[48] Porogens are then removed through leaching with water to form porous scaffolds.[49-50] Melt molding provides independent control of porosity and pore sizes, but has the disadvantages of needing high processing temperatures for non-amorphous polymers and incomplete elimination of porogens.[51] Fiber bonding can be used to manufacture scaffolds with potent mechanical integrity while retaining high porosity.[52-53] However, despite the structural integrity conferred on the bonded fibers, this technique requires organic solvents and elevated temperatures which may be toxic to cells and inhibit the use of heat labile biomolecules.[51] Instead, electrospun scaffolds have been fiber bonded and demonstrated significantly improved mechanical properties without affecting the surface properties.[54] Conventional scaffold fabrication techniques can construct porous scaffolds out of a variety of materials for use in tissue engineering. The simple design process and compatibility with other scaffold fabrication methods ensure conventional techniques will remain relevant for producing highly porous scaffolds for prototyping and proof of concept studies. In addition, other challenges that are faced when using these techniques include the lack of precise uniformity, limited interconnected pores, and structural shape limitations.[51]

Three-dimensional printing has been developed as an advanced technology to overcome the limitations of conventional methods of 3D printing and may ultimately

lead to the production of scaffolds capable of more effectively promoting the regeneration of functional tissue. With the assistance of computer-aided designs (CAD), scaffolds can be reproducibly fabricated and, depending on the 3D printing technology, performed with nanoscale precision. Three-dimensional printing technology has emerged as a promising tool to fabricate scaffolds with high precision and accuracy, creating intricately detailed biomimetic 3D structures.[55] The techniques currently being used to achieve 3D printing of scaffolds, which involve a layer-by-layer process, include, but are not limited to, direct 3D printing, fused deposition modeling, stereolithography, and selective laser sintering. These techniques have been used to produce scaffolds ranging from millimeter to nanometer sized scaffolds. It is also important to note that solid freeform fabrication, additive manufacturing, and 3D printing have become synonymous over the past decade and are now used interchangeably. Advantages of using 3D printing include the ability to fabricate versatile scaffolds with complex shapes capable of homogenous cell distribution, and the ability to imitate the extracellular matrix (ECM). However, the availability of biomaterials with the stability and desired properties for 3D printing of scaffolds is restricted depending on the printing technology used. Another disadvantage is the production time that it takes to fabricate scaffolds, which greatly increases as the scaffold design becomes more and more precise and intricate.[56] This is especially the case for conventional methods which involve a lot of manual labor compared to an automated process.[51] With increased research and understanding of 3D printing, the use of hybrid materials and multiple printing technologies may lead to the fabrication of ECM-like scaffolds capable of overcoming current disadvantages. Evolving from conventional techniques, 3D printing provides

tissue engineers with a way to design scaffolds capable of mimicking the microenvironment that supports cellular attachment, proliferation, distribution, and differentiation with the potential to form functional tissue. In this chapter, we will assess the most common 3D printing materials and technologies being implemented to design scaffolds for the purposes of controlled drug delivery.

Materials used for 3D printing of scaffolds

Important criteria to consider when fabricating suitable scaffolds for tissue regeneration are biocompatibility, biodegradability, pore interconnectivity, pore size, porosity, and mechanical properties. Biocompatibility and biodegradability are important properties for scaffold materials to possess, ensuring they are degraded into nontoxic products while leaving behind only the desirable living tissue. In addition, the material should not generate excessive inflammatory responses as this would hinder or even prevent angiogenesis and new tissue formation.[57] It would also be beneficial if scaffold materials could behave as substrates for cellular attachment, proliferation, and differentiation. Furthermore, as cells proliferate and differentiate, the scaffold must be able to withstand the forces being applied by the cells otherwise its collapse would result in poor diffusion of oxygen, nutrients, and waste, leading to inefficient tissue formation. Finally, the mechanical stability of the scaffold must be structurally sound so as to withstand daily activity and normal body movements.[58] Naturally derived materials such as alginate, chitosan, collagen, fibronectin, and hyaluronic acid have an advantage over synthetic materials as they provide more innately biological functions. Using naturally derived materials, that normally constitute or inhabit the ECM, results in a better mimicking of genuine ECM and this

therefore enhances cell attachment and regulates cellular proliferation more efficiently than synthetic polymers.[59] Although natural materials are beneficial for cellular processes, the use of synthetic polymers such as poly(e-caprolactone) (PCL) and poly(D, L-lactic-co-glycolic acid) (PLGA) for scaffolding has yielded higher mechanical strengths, higher processability, and controllable degradation rates.[59-60] However, these synthetic polymer scaffolds have relatively low biological activity, in terms of promoting tissue regeneration, compared to naturally derived-ECM polymers. In addition to being less biologically active, the intrinsic hydrophobicity of synthetic polymers, such as polyesters, generally results in poor cell adhesion[61], which results in suboptimal proliferation and differentiation, ultimately leading to substandard tissue formation.[59]

For 3D printing systems utilizing powder beds, grain size and grain size distributions must be taken into account to produce porous scaffolds[62], as these factors have a direct influence on microporosity which has been seen to influence cell distribution, attachment, proliferation, and differentiation.[63-64] To achieve biomimicry of the ECM, scaffolds need to be biologically active, have high mechanical strengths, be easy to process, and have controllable degradation rates. To create these complex scaffolds, hybrid systems comprising both synthetic and natural polymers have been used and are likely to be used in the future.[65-67] It is important to keep in mind that different powdered combinations, materials, and structure size have direct effects on the scaffold printability, as is the case for most materials in 3D printing. To be a viable option for tissue regeneration, it is important to keep in mind that the materials used for 3D printing of scaffolds for tissue engineering should be printable with a high degree of reproducibility. Such materials should also be cost-

effective and malleable to form the desired morphology of the design scaffold. The search for the optimal material or material blend for 3D printed scaffold fabrication is an ongoing challenge. This research is necessary, as different types of tissue replacements require different specifications such as specific pore sizes, scaffold morphologies, or mechanical strengths. Scientists are continuously searching for more effective scaffolds capable of mimicking the ECM for cellular attachment, proliferation, and differentiation resulting in the formation of functional tissue. To date, the majority of research on 3D printed scaffolds has been concerned with bone tissues, and therefore more research is necessary in the field of tissue engineering with respect to other tissues such as cardiac tissue. Newly designed composites and synthesized biomaterials may pave the way for 3D printed scaffolds with >99% precision, 100% interconnectivity, versatile pore size manipulation, and high mechanical strengths for a range of load-bearing and tissue formation applications.

3D Printing techniques for scaffold fabrication

In the last decade, many different techniques have been used to form porous 3D biomimetic scaffolds, and have included phase-separation, self-assembly, electrospinning, freeze drying, solvent casting/particulate leaching, gas foaming, and melt molding. Using scaffolds, the architecture of native extracellular matrices can be mimicked at the nanoscale level and therefore provide the primary base for the regeneration of new tissue.[68] Originally a “top-down” approach was used as a tissue engineering method for scaffold fabrication. In this method, cells are seeded onto a biodegradable and biocompatible scaffold, and are predicted to migrate and fill the scaffold hence creating their own matrix. By using this technique, several avascular

tissues such as bladder[69] and skin[70] have been engineered effectively. However, due to the limited diffusion properties of these scaffolds, this technique faces several challenges for fabrication of more complex tissues such as heart and liver.[71] Therefore, "bottom-up" methods have been developed to overcome this problem.[72] Bottom-up approaches include cell-encapsulation with microscale hydrogels, cell aggregation by self-assembly, generation of cell sheets, and direct printing of cells.[73] These tissue blocks can be assembled to form complex tissue constructs using various methods including microfluidics,[74] magnetic fields,[75] acoustic fields,[76] and surface tension.[76] These methods are relatively easy and have provided a solid foundation for the fabrication of scaffolds. However, as mentioned previously, these conventional methods suffer from several limitations including inadequate control over scaffold properties such as pore size, pore geometry, distribution of high levels of interconnectivity, and mechanical strength. As such, it is necessary to develop technologies with sufficient control so as to design more intricate tissue-specific scaffolds. In addition, scaffolds can be coated using surface modification techniques (such as introducing functional groups) to enhance cell migration, attachment, and proliferation. Three-dimensional printing allowed scaffolds to become more precisely fabricated (similar to that of the computer-aided design (CAD)) with higher flexibility in the type of materials used to make such scaffolds. Three-dimensional printing uses an additive manufacturing process where a structure is fabricated using a layer-by-layer process. Materials deposited for the formation of the scaffold may be cross-linked or polymerized through heat, ultraviolet light, or binder solutions. Using this technology, 3D printed scaffolds can be prepared for optimized tissue engineering. For appropriate formation of tissue architecture, the seeding cells (often stem cells)

require a 3D environment/matrix similar to that of the ECM. The ECM acts as a medium to provide proteins and proteoglycans among other nutrients for cellular growth. The ECM also provides structural support to allow for cellular functionality such as regulating cellular communication, growth, and assembly.[77]

With this in mind, scientists and engineers originally attempted to replicate the ECM through conventional techniques, which consequently established a framework for using more advanced techniques, such as 3D printing, to yield higher quality scaffolds. The 3D printing technique can create defined scaffold structures with controlled pore size and interconnectivity and the ability to support cell growth and tissue formation.[27, 78-79] The current methods for 3D printing involve CAD, which is then relayed to each 3D printing system to "print" the desired scaffold structure. Through various 3D printing technologies, discussed below, researchers are trying to fabricate biocompatible scaffolds that efficiently support tissue formation.

Computer aided design and digital imaging

The start of many 3D printing processes involves a CAD that must be drawn or taken from known organ structures. Generally 2D slices acquired from imaging instruments are compiled and stacked on top of one another to form a 3D structure.[35, 80] In tissue engineering, it is imperative to grow tissue similar to that of the native tissue and in order to accomplish this, imaging techniques can be used to produce scaffolds that closely mimic the structure of native tissues.[77] These images inform scaffold designs by providing morphology and size parameters to which scaffolds need to conform in order to fit into irregularly shaped defects/fractures where tissue formation is desired. The scaffold shape also helps to direct the growth of cells and provide shape for the final tissue.[81] It is also worth noting that scaffold

shape can affect the type of tissue regenerated as can be seen in dentin tissue regeneration with differentially shaped scaffolds using dental pulp-derived cells.[82] The complexities in morphology and architecture of tissues can be delineated with imaging technologies such as magnetic resonance imaging (MRI) and computer tomography (CT). These imaging technologies help to take cross-sectional slices of organs and compile them into a 3D image, thus allowing the design of scaffolds to be a close representation of native organs.[35]

MRI functions by using magnetic fields and pulsating radio waves to yield detailed pictures of organs and soft tissues. Using gradient coils to interpret energy signals produced by water molecules within the tissue, 2D images are generated.[83] These 2D images are then stacked to create a 3D image of the scanned area. Because MRI requires hydrogen molecules generally in water, they are best used for soft tissue imaging such as ligament and tendons and organs of the chest and abdomen (heart, spleen, pancreas, liver, kidneys). They are also used to image pelvic organs such as the bladder and reproductive organs.

CT, also known as computerized axial tomography, is a technology that uses X-rays to produce images from a scanned area. In a CT scanner, x-ray tubes are rotated around a patient's body producing signals that are taken up by digital x-ray detectors and sent to be processed by a computer to generate cross-sectional images of the body. These cross-sections are then stacked to create a 3D image of the scanned organ(s). CT scans are generally used for imaging bone due to its density while soft tissues can be problematic as they have varying abilities to inhibit x-ray penetration resulting in faint or undefined images. In order to image these soft tissues,

contrasting agents such as iodine or barium-based compounds may be used to facilitate contrast and increase visibility.[84]

MRI is preferable over CT when attempting to image soft tissue and other organs besides bones as the contrast of tightly placed organs can more readily seen when changes to radio waves and magnetic fields are applied. The radio waves and magnetic field enable the ability of the instrument to highlight the desired tissue in tightly knitted areas. However, CT scans create better quality images of bone structures than MRI due to the low concentration of water in bones resulting in less hydrogen atoms emitting energy to succinctly create a cross-sectional image. Creating a scaffold directly from the images is not always feasible due to the possibility of scanning diseased or damaged organs.[35] In this case, computer modeling may be necessary to recreate the missing parts of the organ or tissue. With MRI and CT imaging techniques, the reconstruction of both 2D and 3D images is a powerful tool to recreate the complexity of tissue structures. These tools allow researchers to be one step closer to fabricating a precise replica of the needed extracellular matrix to enhance functional tissue formation.

Direct 3D printing

Three-dimensional printing involves the fabrication of structures through successive layer deposition using a computerized process. The first “3D printer” was developed by Sachs et al. at the Massachusetts Institute of Technology (MIT) in the 1990s and was based on the technology of an ordinary inkjet printer. This printing technique can sometimes be referred to as “binder jetting” or “drop-on-powder”.[85] In an ordinary 2D inkjet printer, the ink nozzle moves in a side to side motion incrementally along one plane such that the printed material has the 2 dimensions of

length and width. A 3D printer uses the same technology, but as well as moving side to side along one plane, the printer has a platform capable of moving up and down (90 degrees to the side to side motion), hence adding the dimension of height and thereby printing in 3 dimensions. The 3D printer designed by researchers Emanuel Sachs, John Haggerty, Michael Cima, and Paul Williams at the MIT has similar characteristics to the 2D inkjet printer. However, instead of ink, the 3D printer uses a liquid binder solution that is selectively deposited on a powder bed instead of paper. The process begins with a powder bed, which could vary depending on materials used, that is spread onto the build platform and leveled using a roller system. The printer nozzle then dispenses binder solution in the designated powdered areas directed by the CAD. Once the binder solution and powder are combined, the excess powder is removed (blown off). The build platform is then lowered, and a new powder layer is deposited and leveled. This process is then repeated until the final structure is created (**Figure 1-1**). This technique also has the versatility to change the composition of binder and powder if it is deemed necessary where certain parts of the scaffold may require a material with higher mechanical strengths and/or smaller pore sizes. An example of this may be building a scaffold with larger pore sizes deep within the scaffold, while having smaller surface pores. With the increase in pore sizes, cells deep within the scaffold will be able to maintain their cellular processes as vital resources such as nutrients, oxygen, and waste are able to diffuse without difficulty compared to small pore sizes that may result in the nutrient deprivation of cells leading to cell death. Cell death on a large scale ultimately leads to the collapse of the scaffold and the inability to form functional tissue. The resulting desired effect of the fabricated scaffold will be to provide a medium that guarantees high

proliferation and differentiation of cells to generate functional tissues. The advantages of this method are the expansive list of powder-binder solutions available to yield the desired scaffold. The use of binders, however, can lead to toxicity if they are not completely removed once the scaffold is ready to be implanted, as in the case of organic solvents that are used as binders for some powdered polymer materials. Another disadvantage for this printing technique is the post processing required, where heat treatment may be necessary to ensure durability.[86]

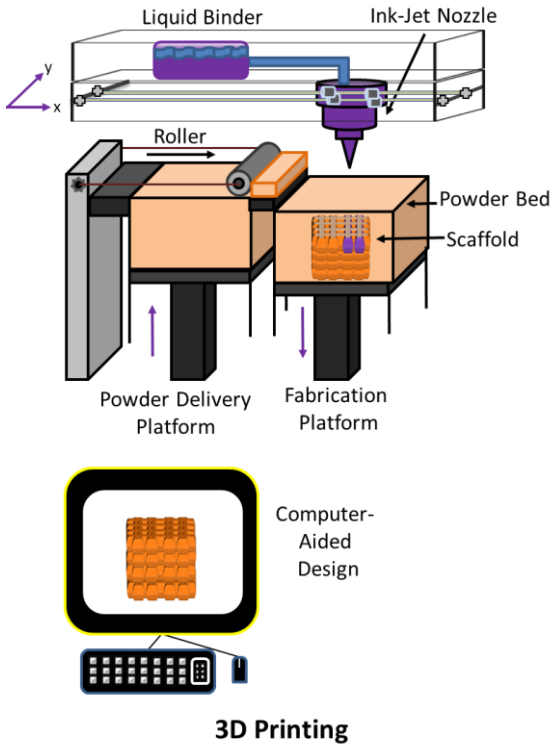

Figure 1-1 : Schematic of direct 3D printing of a CAD scaffold. Adapted from "Porous scaffold design for tissue engineering" by Scott Hollister, Nature Materials 2005, 4, 518.[20]

Bioprinting

In a similar manner to direct 3D printing, 3D-Bioplotter printing, or bio-printing, has garnered much attention due to its ability to print scaffolds with cell-laden gels. Bioplotter printing is a rapid manufacturing technique that uses a nozzle extrusion

system of thermally or chemically treated materials (**Figure 1-2**). In this system, the ink cartridge contains “bioink” rather than a binder solution used in direct 3D printing. As with all 3D printing methods, a CAD is first created and then sent to the 3D printer. The materials are deposited in a layer-by-layer fashion, where each layer may contain a combination of different materials. Similar to that of ink cartridges in an inkjet printer, the Bioplotter printer is capable of using and changing “bioink” to develop the final scaffold structure. A key feature of Bioplotter systems is that they print cell-laden gels, often with other polymeric materials such as PCL, to yield viable and functional scaffolds.[55, 87] Three-D-Bioplotter printing utilizes a pneumatic pressurized air system to dispense the bioink in a layer-by-layer fashion. When printing cell-laden gels, nozzle diameter and pressure must be calibrated because excess shear stress generated in the nozzle decreases cell viability.[88-89]

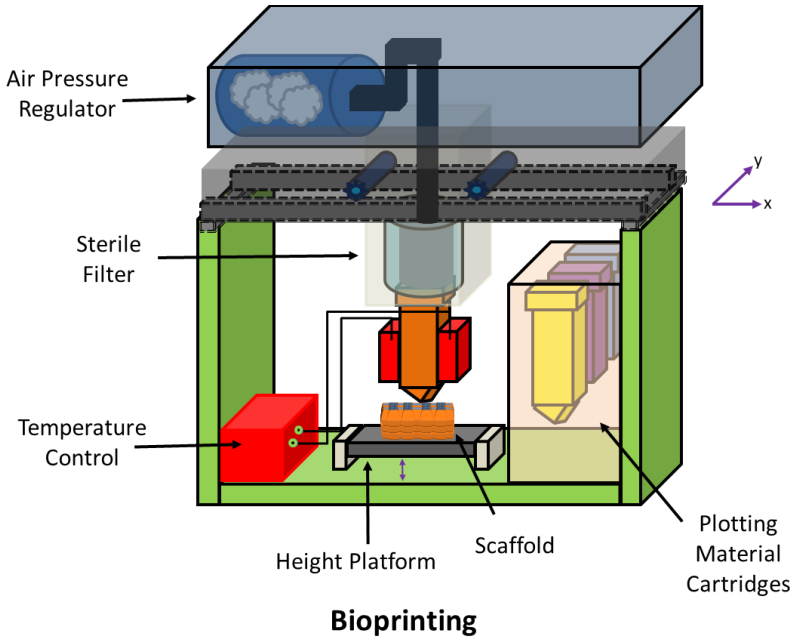

Figure 1-2 : Schematic of bioprinting printer set-up.

In order to develop a more efficient all-in-one system, one group used a NovoGen MMX Bioprinter from Organovo which comprised two pumps and two nozzles.[90] This system was capable of dispensing gelatin methacrylate (GelMA) hydrogels, whilst simultaneously dispensing cells to seed the scaffold. This system enables the direct addition of cells into the scaffold rather than waiting to seed the cells after scaffold fabrication. This direct seeding has the advantage of homogenously distributing cells throughout the scaffold, as well as being less time consuming. A UV light guide was also added to the printer to allow for photopolymerization of the GelMA. This system generated HepG2 cell-laden scaffolds capable of retaining high cell viability for at least eight days *in vitro*. This study illustrates the viability of using a 3D printer to print scaffolds for complex tissue engineering processes.

A bioplotter printer is a nozzle-deposition tool used to fabricate 3D scaffolds. A Tissue Engineering 3Dn-300 printer that was designed by Sciperio/nScrypt Incorporated to print composite scaffolds with varying PLA/PEG blends of 5, 10, and 20% (w/w) of PEG and PLA/PEG/bioactive calcium phosphate (CaP) glass. The blend incorporated the use of PEG as a plasticizer to decrease the glass transition temperature of the blend and enable processing at low temperatures.[91] The addition of PEG improved scaffold processing, however, the ability of these scaffolds to support cell growth both *in vitro* and *in vivo* is yet to be explored. Using a modified Bioplotter printer, a multihead tissue/organ building system was used to print PCL and cell laden hydrogels, while using PEG as a sacrificial layer. This system utilized a hybrid system of inkjet printing (hydrogels) and fused deposition modeling (thermoplastics) to enhance the mechanical stability of the scaffold, as some

hydrogels demonstrate poor mechanical properties.[92] Using this system, a complex-shaped scaffold for ear regeneration was fabricated.[67] The process involved the creation of a sacrificial layer as a base for the formulation of complex structures that was easily dissolved away. Similar to trying to build an inverse pyramid or bowl-shaped structures, there needs to be a support layer to allow the complex structure to take shape. Using these complex ear-shaped scaffolds positive *in vitro* results of chondrogenesis and adipogenesis from the co-printed chondrocytes and adipocytes were obtained. The use of this hybrid system will allow direct 3D printing to increase its flexibility in designing scaffolds with even the most complex shapes. The 3D-Bioplotter technology provides researchers with a versatile and convenient tool to manufacture ready-to-implant scaffolds with high mechanical strength, interconnectivity, porosity, biodegradability, and the ability to achieve higher rates of attachment, differentiation, and proliferation for enhanced tissue regeneration.

Stereolithography (SLA)

SLA is a process where 3D scaffolds are formed from a liquid polymer via a light-mediated chemical reaction. The exposure of photosensitive material to light triggers a chemical reaction that leads to polymerization. Polymerization is a process of reacting monomers or polymers together to form polymer chains or three-dimensional networks that are highly crosslinked. In SLA rapid prototyping, a vat of liquid photosensitive (photocurable) polymer or monomer is exposed to light (UV range of 300 – 400 nm) to be photocured.[93-96] After the first layer is cured, the process is repeated, overlaying the previous layer, until the scaffold has been fully designed (**Figure 1-3**).

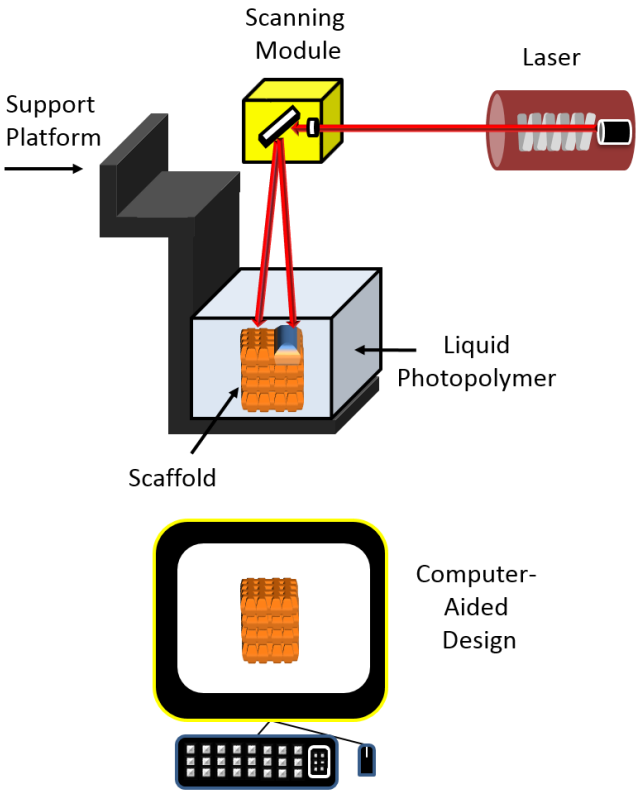

Figure 1-3 : Schematic of stereolithographical technique for manufacturing scaffolds. Adapted from "Porous scaffold design for tissue engineering" by Scott Hollister, Nature Materials 2005, 4, 518.[20]

The advantage of SLA is the use of the photopolymer, where the uncured polymer can be reused for another print. In addition, because of the use of lasers, scaffolds with higher resolution can be made.[96-97] The disadvantage of this technique is that the photopolymers are often not biodegradable once cured and crosslinked. In addition, photoinitiators are often toxic and generate free radicals that may be detrimental if not fully removed from the final structure. However, scientists are constantly trying to improve the system by creating biodegradable photopolymers.[97-98]

SLA 3D printing was also used in combination with electrospinning to fabricate highly aligned neural scaffolds. This technique was used to overcome the limitations of high resolution scaffolds without compromising mechanical properties. In this set up, PCL or PCL/gelatin scaffolds were initially prepared through electrospinning and then placed on a petri dish to be printed on with a Printrbot® printer using a hydrogel composed of 40 wt. % PEG (MW 300), 60 wt. % PEG-diacrylate (PEG-DA) (Mn 700) and photoinitiator (0.5 wt. % of PEG-DA concentration). When seeded with NE-4C neural stem cells, the ~1000 μm pore sizes equating to 66% porosity enhanced neural cell attachment compared to scaffolds with smaller porosity. Using this design, scaffolds with PCL/gelatin fibers not only had the highest mechanical stability, compared to all other iterations of printing, of 4.83 ± 1.14 MPa, they were also observed to have increased average neurite length and directed neurite extension of cortical neurons along the fiber. Thus, combining various printing techniques to tailor scaffolds for specific tissue regeneration needs may be a promising way forward, as explored by Lee et al.[99]

SLA technology provides an opportunity to print complex and defined scaffolds, where intricacies in the morphology of the scaffold may affect cellular differentiation and alignment as described for neural cells above. One of the biggest advances in SLA has been the creation of a two-photon 3D printer, where a Nanoscribe Photonic Professional GT two-photon lithography system was able to print scaffolds with 3 μm diameter pores and generate retinal cell grafts seeded with human iPSCs. Worthington et al. at the University of Iowa demonstrated the feasibility of using stem cells to restore vision to patients with retinal degenerative disease.[97] The 2PP technique is based on the interaction of femtosecond laser beams focused by a high

numerical-aperture objective to induce polymerization of a photosensitive resin within the volume of the focused laser beam (voxel) which can create resolutions down to 100 nm.[100] This resolution is made possible due to the polymerization of the photosensitive material occurring only in the region where light intensity exceeds the threshold for initiating the polymerization thus confining polymerization within the voxel.[101] With two photons, the voxels are smaller compared to conventional SLA printing.[102] With the advancements in SLA technologies, such as two photon 3D printing, 3D printing can be applied to a plethora of diseases and may possibly be a means of creating controlled drug delivery devices. Although the advances in 3D printing have led to the fabrication of scaffolds with fine resolutions (down to 10 μm precision) suitable for a range of tissues, the translation of 3D printed scaffolds to the clinic has been slow. Current obstacles to using 3D printed scaffolds in clinical applications reside in issues of biologics, engineering, cost, and regulation/safety. For biologics, it is necessary to take into consideration the survival requirements of cells such as oxygen diffusion, cell migration and levels of vascularization which have often been suboptimal. In terms of engineering, the processability and reproducibility of the scaffolds is necessary to ensure consistency and homogenous application. As 3D printing is a novel approach to tissue engineering, the procurement of a 3D printer with the ability to print scaffolds with fine resolution can be an expensive investment (up to $1.2million for a single printer). In addition, the supply of approved and appropriate materials, cell culture facilities and, in many cases, recombinant factors will add to the financial burden. Finally, regulation and safety guidelines must be established and a standard must be set in order to ensure that scaffolds meet a certain criteria before being used.[103] Never-the-less, the abundance of preclinical *in*

vivo studies using various 3D printing techniques demonstrates the feasibility of using scaffolds for tissue regeneration (**Table 1-1**). As scientists, engineers, pharmacists, dentists, and physicians continue to collaboratively develop these 3D printed scaffolds for tissue regeneration, the likelihood of overcoming barriers to clinical applications is high.

Table 1-1 : Table summarizing preclinical progress of 3D printing techniques used to print scaffolds for tissue engineering.

Printing Method	Advantages	Disadvantages	Preclinical progress
Direct 3D printing/Inkjet	▪ Versatile in terms of usable materials ▪ No support is necessary for overhang or complex structures	▪ Potential toxicity (incompletely removed binders) ▪ Low mechanical strength prints compared to laser sintering ▪ Time Consuming(Post-processing)[86]	▪ (Rat/Bone)[104-108] ▪ (Rabbit/Bone)[109-110] ▪ (Mouse/Bone)[110-111]
w/electrospinning			▪ (Mouse/Cartilage)[112]
Bioplotting	▪ Prints viable cells[55, 87] ▪ Soft tissue applications[113]	▪ Limitation on nozzle size*[88] (*Must not be cytotoxic during processing) ▪ Requires support structure for printing complex shapes	▪ (Rabbit/Trachea)[114] ▪ (Rabbit/Cartilage)[115] ▪ (Rat/Cartilage)[116] ▪ (Mouse/Cartilage)[117] ▪ (Mouse/Tooth regeneration)[118] ▪ (Mouse/Skin)[119]
Fused Deposition Modeling	▪ Low cytotoxicity vs direct 3D printing[120] ▪ Relatively inexpensive (printers and materials)[121]	▪ Limitation on materials (often requires thermoplastics)[122] ▪ Materials used are non-biodegradable ▪ Requires support structure for overhangs and complex shapes ▪ Post-processing may be necessary ▪ Low Resolution[121]	▪ (Swine/Bone)[123] ▪ (Rat/Bone)[120, 124]
Selective Laser Sintering	▪ Provides scaffolds with high mechanical strength ▪ Powder bed provides support for complex structure ▪ Fine resolution[125-126]	▪ Limitation on materials (must be shrinkage and heat resistant) [116] ▪ Very high temp required(up to 1400ºC) [127] ▪ Expensive and time consuming (processing and post processing)	▪ (Mouse/Bone) [128] ▪ (Rat/Heart)[129] ▪ (Rat/Bone)[130-131] ▪ (Mouse/Skin)[131-132] ▪ (Mouse/Heart)[132]

Table 1-1 — Continued

Stereolithography	▪ Very high resolution[121] ▪ Speed of fabrication[133] ▪ Smooth surface finish	▪ Materials must be photopolymers[134] ▪ Expensive (two photon printers)[121] ▪Support system is necessary for overhang and intricate objects.	▪ (Rat/Bone)[135] ▪ (Rabbit/Trachea)[136] ▪ (Pig/Tendon)[137]
Electrospinning	▪ Speed of fabrication ▪ Cell printing[138] ▪ Soft tissue engineering [139] ▪ Low shear stress (bioelectrospraying)[140]	▪ Random orientation of fibers[141] ▪ Non-uniform pore sizes[142] ▪ High voltage(1-30 kV) requirements[143-144]	▪ (Mouse/biocompatibility)[145-146] ▪ (Rat/Bone)[147-148] ▪ (Rabbit/Vascular tissue)[149]
Indirect 3D Printing	▪ Good for prototyping/preproduction ▪ Material versatility casting once mold is obtained[150]	▪ Requires proprietary waxes for biocompatibility(Wax Printing)[151] ▪ Low accuracies/resolution[152] ▪ Mold required for casting[153] ▪ Long production times (mold→cast→processing→product)	▪ (Rat/Bone)[154] ▪ (Mouse/Tooth regeneration)[155]

RESEARCH OBJECTIVE

The goal of this research was to develop and investigate controlled drug release systems with an emphasis on 3D printing technologies for its potential role in scaffolding to enhance the process of tissue engineering.

RATIONALE AND SPECIFIC AIMS

Controlled drug delivery systems and devices have the potential to address many of the challenges facing conventional approaches to treating a range of pathologies including cancer and tissue maladies that require healing or replacement. Developing technologies for 3D printing of scaffolds for tissue engineering is an area of research undergoing rapid advances. A major aim in the development of 3D printed scaffolds is the creation of scaffolds that closely resemble the native microenvironmental properties at the site of implantation, such as ECM properties, load bearing mechanical properties, pore size arrangements to allow nutrient diffusion and cell migration, and the appropriate growth factor milieu for the promotion of angiogenesis and/or osteogenesis. As new materials and “bioinks” are synthesized and novel printing methods are discovered, the 3D printing of scaffolds to be used in tissue engineering continues to become more sophisticated and effective. The 3D printing techniques and materials discussed in this chapter are likely to contribute to improved approaches to generating functional tissue for replacement and repair. Composite materials and hybrid 3D printing approaches are likely to lead to the next generation of advanced 3D printed scaffolds for tissue engineering applications. These hybrid systems, as discussed, have the potential to mitigate the disadvantages of any one printing technique and even the limitations of

the materials used. As current techniques are further fine-tuned and more bioink materials become available, the design of effective ECM-like scaffolds becomes increasingly possible. The focus of 3D printing techniques in medicine to date has generally been aimed at regenerating or replacing tissue *in vivo*, however, alternative approaches also being investigated include the printing of functional tissues *in vitro.* Such 3D printed tissues can be formed using a patient's own cells thereby potentially overcoming issues of rejection [156-157]. As technologies advance and 3D printing becomes a prominent tool for fabricating scaffolds for tissue engineering and implants for other diseases, the incorporation of controlled drug delivery systems will contribute to enhancing the therapeutic properties of the printed constructs. Promising results using 3D printing have been seen preclinically for soft tissues and clinically as implants in hard tissue, but more research is needed to ensure the effectiveness of current 3D printed constructs. Ultimately, 3D printing of scaffolds for tissue engineering may be the key to giving those suffering from organ failure and dysfunction caused by damaged or diseased tissue a chance at an improved quality of life.

In order to test the feasibility of using a controlled drug delivery system for melanoma treatment and using 3D printing technologies to fabricate devices imbued with controlled drug release kinetics and potential differentiation effects, the following specific aims have been proposed:

1. Assess the antitumor potential of an on-demand drug delivery system in a murine melanoma model using ultrasound-triggered doxorubicin release from PLGA microspheres.

2. Assess 3D printing functionality for sequential drug delivery systems using a core and shell model that involved PLGA (core) and alginate (shell; fabricated through a co-axial printing technique) as tube structures.
3. Define controlled drug delivery systems on a microscale through two-photon polymerization (2PP) 3D printing.
4. Investigate the effects of 2PP nano- and microscale topographies on cellular differentiation.

CHAPTER 2 : COMBINING ULTRASOUND AND INTRATUMORAL ADMINISTRATION OF DOXORUBICIN-LOADED MICROSPHERES TO ENHANCE TUMOR CELL KILLING

INTRODUCTION

Cancer is the second leading cause of death behind heart disease in the United States [158], and many cancer types are largely refractory to current conventional treatments. This is particularly so for patients with advanced melanoma and is at least partially due to a lack of antitumor efficacy of chemotherapeutic drugs imposed by multidrug resistance and the narrow therapeutic window.[159-161] Increasing the therapeutic index of chemotherapeutic drugs such as doxorubicin (DOX) is important if progress is to be made in improving tumor regression rates. DOX has the potential to cause fatal cardiomyopathy once the lifetime cumulative total soluble dose exceeds 450 mg/m^2.[162] As a result, DOX formulations have been developed and introduced into the clinic, such as pegylated liposomes, known as Doxil® [162], which have exhibited decreased drug toxicity compared to conventional DOX therapy although they have not made significant improvements in antitumor efficacy and long term survival.[163-165] Additionally, Doxil® still has dose-limiting side effects, such as hand-foot syndrome.[162]

It is becoming increasingly apparent, due at least in part to the heterogeneity of tumors, that a multipronged therapeutic approach is necessary for the treatment of advanced cancers where each therapy can have additive or, preferably, synergistic tumoricidal consequences. In this research, we attempted this by administering US to DOX-loaded microspheres, made from United States Food and Drug Administration-approved, biodegradable, and biocompatible PLGA [166-167], at the tumor site. Appropriate formulations need to be generated that provide safe and sustained

release of the drug payload within the therapeutic window. Techniques such as double emulsion solvent evaporation (water-in-oil-in-water) [168], aqueous-aqueous emulsion (followed by solid-in-oil-in-water) [169-170], solid-in-oil-in-hydrophilic oil-in-water [171], and solid-in-oil-in-hydrophilic oil-in-ethanol[172] have generated microspheres with abilities to provide sustained release of drugs from periods of weeks to months. The application of US can promote the inertial cavitation of air bubbles (or nucleation sites) [173] in close proximity to, or in direct contact with, microspheres or cells, resulting in direct (shock waves from inertial cavitation) or indirect (microsphere collisions) damage of these microspheres or cells. Inertial cavitation is a process where air bubbles expand to 2 - 3 times their resonant size and then implode during a single compression generating large gas pressures and temperatures.[174-175] The effects of US-induced inertial cavitation have also been seen to accelerate solid particle velocities which are capable of producing interparticle collisions resulting in morphological and compositional changes.[176-178] Although the concept of combining US and non-acoustically active micro-, or nanospheres for the purposes of drug or gene delivery has received some attention there have been no investigations into the application of such a system for the purposes of tumor cell killing.[179-180] By combining US and DOX-loaded microspheres there is the increased potential for manifold modes of cytotoxicity, which include physically-mediated direct lethal damage to cells or sufficiently disrupting membrane integrity (non-lethal) so as to increase intracellular uptake of DOX. Also, US may have a role in enhancing the release of DOX from microspheres by damaging microspheres through inertial cavitation of neighboring air bubbles, or indirectly through microsphere collisions. In addition, DOX possesses the ability to not only kill cells by inhibition of DNA synthesis,

it also induces an immunogenic form of cell death thereby potentiating tumor-specific immune responses.[181] Thus local treatment of a tumor with chemotherapeutic agents such as DOX can have systemic ramifications in terms of the generation of tumor specific immune responses[182] as has been more commonly observed with radiation therapy (and is often referred to as the abscopal effect).[183] We hypothesized that the combination of US with DOX-loaded microspheres delivered intratumorally could have a synergistic tumoricidal effect through multiple modes of tumor cell killing, thereby enhancing survival in tumor-challenged mice. In this study DOX was encapsulated within microspheres (diameter 4-8 μm) made from PLGA through a double emulsion solvent evaporation technique . PLGA microspheres in this size range often degrade gradually over a period of days to several weeks, releasing the encapsulated drug gradually, however, we hypothesized that with the application of US, a more rapid release rate can be triggered through the damage caused to the surface of drug loaded microspheres as a result of inertial cavitation of neighboring air bubbles. Although increased release rates from drug-loaded echogenic nanoparticles has previously been reported, such findings with solid and henceforth presumably non-echogenic particles have not been well documented [180]. In this study, we evaluated the effects of combining US with DOX-loaded solid microspheres and speculate how this combination may have contributed to the reduced growth of B16-F10 melanoma cells observed *in vitro* and *in vivo*.

Poly(lactic-co-glycolic acid) (PLGA)

PLGA (**Figure 2-1**) is an FDA approved, synthetic, biodegradable and biocompatible polymer that has had many clinical applications, including 14 PLGA-

based drug products in the United States.[184] The first FDA approved PLGA product was the Lupron Depot where PLGA microspheres deliver leuprolide acetate for the treatment of advanced prostate cancer (and now endometriosis[185]) over a period of 4 months.[186-187] PLGA degrades through ester hydrolysis to form lactic acid and glycolic acid which enter the tricarboxylic acid cycle to be metabolized into carbon monoxide and water.[166, 188] PLGA properties, such as crystallinity and hydrophilicity can be tuned by adjusting the lactide to glycolide ratio, where these ratios directly influence the degradation behavior of the polymer. The ratio of lactide to glycolide also directly affects the release kinetics of various drugs due to its level of crystallinity.[166] The highly tunable nature of PLGA polymers make them suitable for the development of devices designed for drug delivery and tissue engineering. These PLGA polymers also offer a high rate of reproducibility when used in particle formulations for the purposes of controlled drug delivery through sustained release. These controlled drug delivery systems can also be further enhanced through surface modification for targeted drug release [189-191]. One group modified the surface of PLGA nanoparticles with monoclonal antibodies raised against soluble membrane proteins derived from a human invasive ductal breast carcinoma cell line (MCF-7). When the nanoparticles were incubated in a co-culture of MCF-10A neoT cells (a cell line that originated from human breast epithelial cells) and Caco-2 cells (originating from human colon adenocarcinoma cells), the nanoparticles were localized solely on, and only entered, MCF-10A neoT cells, whereas non-coated particles were distributed randomly and were taken up by both cell types.[192] In a separate study, PLGA/PLGA-PEG-PLGA microparticles loaded with bone morphogenetic protein 2 (BMP-2) were fabricated to provide sustained delivery of BMP-2. The sustained delivery of BMP-2 was shown *in*

vitro to stimulate high levels of osteogenic differentiation (as measured by alkaline phosphatase and alizarin red staining) in murine calvaria pre-osteoblast (MC3T3-E1) cells by day 10 when incubated with BMP-2 loaded particles as compared to little or no differentiation in control growth media and minimal differentiation in cells cultured with osteogenic supplemental media.[193] As scientists unravel and understand the cause of many diseases, PLGA will continually provide a platform capable of tailoring drug delivery requirements for these diseases.

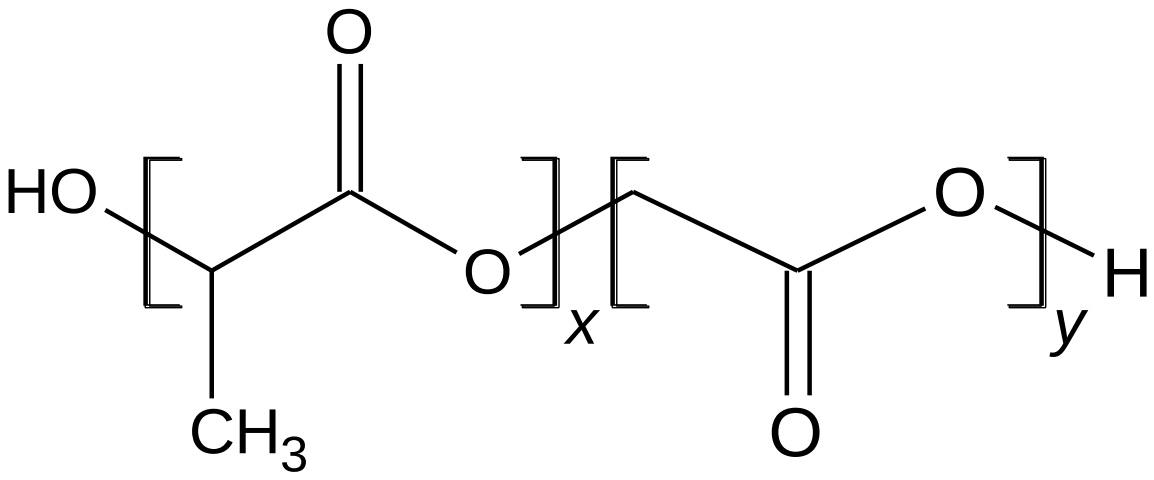

Figure 2-1 : Chemical structure of poly(lactic-co-glycolic acid) polymer.

Melanoma

Melanoma, also known as *malignant melanoma* and *cutaneous melanoma*, is a skin cancer originating from melanocytes, the melanin pigment-producing cells in the basal layer of the epidermis. Melanoma is the most lethal form of skin cancer because it has a high potential to metastasize (i.e. spread to other tissues). The primary cause of melanoma is exposure to ultraviolet (UV) light either from direct exposure to sunlight (UVA and UVB) or from tanning beds (UVA) which is absorbed by the skin and results in DNA damage. This DNA damage causes results in aberrant gene expression in multiple genes and can lead to malignant tumor formation.

Due to the fact that melanomas occur in the skin, the changes in shape and coloration of existing moles, as well as abnormal growth of melanomas can usually be readily seen by the patient. In fact, patients are frequently the first to notice early-stage melanomas. If diagnosed early enough, most melanomas can be successfully removed by surgery. Early detection and treatment are key because once the cancer metastasizes to other parts of the body, no reliably effective therapy is available and the chances of the patient succumbing to the disease are therefore high.

Melanoma progression can be characterized by five stages (stages 0 – IV) where stage 0 indicates the melanoma to be *in situ,* meaning that the abnormal melanocytes are located only in the epidermis, whilst stage IV, the most advanced, is when the melanoma has metastasized to other parts of the body. Surgery is the first treatment of all stages of melanoma. After stage 0, other therapies besides surgery may be necessary to cure or remove the skin cancer. There are four main types of melanoma. Three of these; superficial spreading melanoma, lentigo maligna melanoma and nodular melanoma comprise 90% of malignant melanoma whilst acral lentiginous melanoma and some other rare types make up the remaining 10%.[194]

Superficial spreading melanoma is the most common type of melanoma accounting for approximately 70% of all diagnosed melanomas. True to its name, this melanoma spreads along the surface layer of the skin for an extended period of time before penetrating deeply. This type of melanoma can form from pre-existing, benign moles. The first signs are darkened, flat, barely- raised lesions with irregular borders and color variations (black, brown, red, tan, or white). This melanoma can be found

anywhere on the body, but most commonly on the backs of men and the legs of women, and the upper back of both sexes.

Lentigo maligna melanoma arises from lentigos, which are flat, brown spots that are associated with aging or sun-damaged skin, rather than moles. For this reason, this type of melanoma is commonly found among the elderly in chronically sun-exposed areas such as the face, ears, arms, and upper torso. Since this type of melanoma arises from lentigos, it closely resembles lentigos, but may contain different shades of brown and other color variations of black, blue, red, gray, or white.

Nodular melanoma is most aggressive of the four main melanoma types because it grows more deeply and more quickly compared to the other three types. The melanoma appears as a blue-black dome-shaped nodule but as with most melanomas, color variations of blue, gray, white, brown, tan, red, or even flesh tones can be possible. This type of melanoma is invasive when it is first diagnosed, and malignancy is recognized when the damaged area becomes a bump or a highly raised area on the skin. This type of melanoma may not necessarily form from an existing mole and often occurs in areas of the body that only receive intermittent sun exposure (e.g. the chest).

Acral lentiginous melanoma is the most common melanoma among African Americans and Asians, and the least common among light-skinned individuals. This melanoma appears as tan, black, or brown discoloration with irregular borders on the palms of hands, soles of the feet, or under nails, particularly the big toenail. The specific causes for this melanoma are unknown and unrelated to sun exposure, so the cancer cannot be attributed to UV radiation.[195]

Treatment strategies for malignant melanoma depend on several parameters including histological classification and stage of the disease. Standard treatment for a primary melanoma lesion is wide excision of the primary tumor through surgery. Excision margins are based on the thickness of primary melanoma; wider excision margins are needed for the removal of a melanoma as its thickness increases due to the potential of metastases of melanomas to the lymph nodes, excision of the draining lymph node (or sentinel lymph nodes) is considered critical since this is most likely to be the first lymph node to which a melanoma will metastasize. Currently, sentinel lymph node biopsies are sensitive enough to evaluate metastasis to the first draining lymph node. If lymph node metastasis is detected in the sentinel lymph node, then other lymph nodes in the area of the primary melanoma may also be surgically removed. When surgery of tumors or metastatic lymph nodes not possible, radiation therapy of the primary tumor or the regional lymph nodes is a viable option. Both types of therapy are appropriate for solitary or localized lesions but are not sufficient for patients diagnosed with metastatic disease. Adjuvant therapy (i.e. additional treatment provided after surgery or radiation) is recommended to patients with potential for recurrence (stages II and III) and may include immunotherapy, or even the testing of a new treatment in a clinical trial. Since there is no effective treatment for the most advanced form of melanoma (stage IV), many treatment options may be offered to the patient which may include a combination of surgery, chemotherapy, and/or immunotherapy.[196]

MATERIALS AND METHODS

Microsphere fabrication

Microspheres were fabricated using a previously described double emulsion solvent method.[168] Briefly, a stock solution of doxorubicin (DOX: Sigma-Aldrich, St. Louis, MO) was made by dissolving 10 mg of DOX in 250 µl of 1% poly(vinyl alcohol) (PVA; Mowiol® 8–88; MW ~67,000; Sigma-Aldrich). This solution was incubated overnight at 4°C to ensure a complete and homogenous solution. Water phase 1 consisted of either 75 µl of the DOX solution or 75 µl of 1% PVA (for blank particles). An oil phase was created by dissolving 200 mg of PLGA (Resomer® RG 503; Boehringer Ingelheim KG, Germany) in 1.5 mL of dichloromethane (DCM). A primary emulsion was prepared by sonication of 75 µl of the water phase 1 into the oil phase using a sonic dismembrator ultrasonic processor (Fisher Scientific, Pittsburgh, PA) at 40% amplitude for 30 s. This emulsified solution was then added to 30 mL of 1% PVA in ammonium acetate buffer solution (pH:8.4) and homogenized using an Ultra Turrax T-25 basic homogenizer (IKA-WERKE, Inc., Wilmington, NC) at speed 4, 17500 min^{-1}, for 30 s. The emulsion was stirred for 1.5–2.0 h in a fume hood to allow DCM to evaporate. The particles were then centrifuged at 7*g for 5 minutes at room temperature to filter out particles larger than desired size. The supernatant was collected and centrifuged at 180*g for 5 min, washed twice with nanopure water, dispersed in 5 mL of water, and lyophilized using a FreeZone 4.5 freeze dry system (Labconco, Kansas City, MO).

Determining size, DOX-loading, and DOX-loading efficiency of PLGA microspheres

Eight batches of DOX-loaded PLGA microspheres were prepared as described above. To determine loading and loading efficiency, samples from each batch were tested. To determine loading, a sample of DOX-loaded microspheres (3-5 mg) post-lyophilization was dissolved in DMSO and the yield of DOX was calculated using a standard curve. Along with the standard curve samples, the test samples were measured for DOX at λ_{ex}485, λ_{em}570 using a SPECTRAmax M5 Microplate Spectrofluorometer (Molecular Devices, San Diego, CA). The yield of DOX was then divided by the weight of DOX-loaded microspheres (in the sample) to determine the loading per mg of microspheres. To determine loading efficiency, the known amount of total DOX-loaded PLGA particles from each batch post-lyophilization was multiplied by the calculated loading (as determined above) and then divided by the original 3 mg of DOX added to fabricate the particles. This value was then multiplied by 100 to achieve a percent value. The size (diameter) of the fabricated microspheres was calculated using scanning electron microscopic (SEM) images (Hitachi High-Technologies, Tokyo, Japan) and analysis using ImageJ software.

Device configuration for US generation

Device configuration and US generation were set-up as previously described[179] where a 4040B 20 MHz DDS Function Generator (BK Precision, Yorba Linda, CA) was used to generate the desired waveforms. The function generator was then connected to a radio frequency ENI 310L RF Power Amplifier (ValueTronics Intl Inc., Algin, IL) which helped to produce excitation signals to drive the transfer of the waveforms to a custom designed 1 MHz transducer (L = 2.5”, D = 1” , ID = 0.5”)

(Ultrasonic S-Lab, Concord,CA). Refer to **Figure 2-2** for instrument configuration. The function generator parameters were programmed to have continuous sinusoidal waves at a frequency of 1 MHz and an amplitude of 0.2 V in order to output the desired ultrasonic waves necessary for microsphere damage. US application was performed using these settings for a period of 10 seconds at an intensity of 900 mW/cm^2 as determined by radiation force balance.

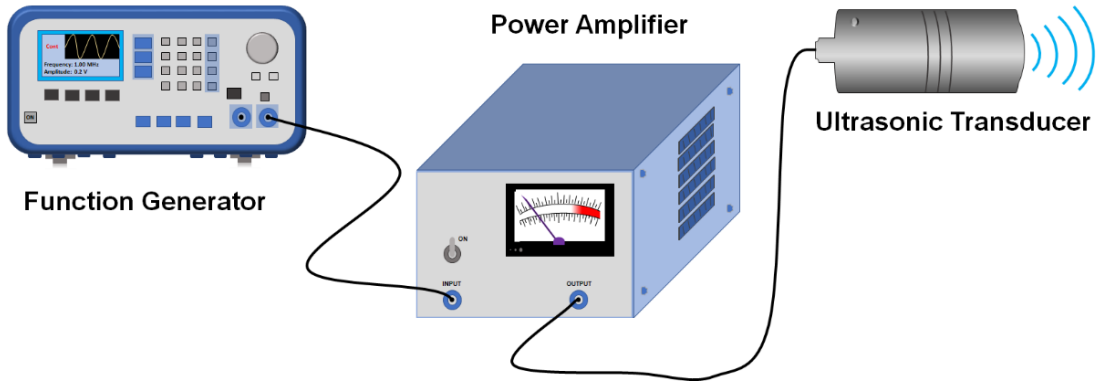

Figure 2-2 : US generation instrument set up.

Ultra-morphology of blank particles after the application of US

Blank particles were weighed and suspended in nanopure water at a concentration of 3 mg/mL and added to a 1.5 mL microcentrifuge tube. The suspensions were then divided in two, where one sample was the control, while the other was the test group. To demonstrate the importance of the presence of air bubbles in mediating US-triggered particle damage, particle suspensions were also made using degassed nanopure water. Nanopure water was degassed under vacuum at high stirring for 24 h. Samples were then sealed with Parafilm® film and fully submerged in a petri dish containing water at room temperature. Underneath this petri dish was a HAM A acoustic absorber (Precision Acoustics, United Kingdom)

which absorbed deflected ultrasonic waves and reduced reflected waves. This acoustic absorber was used to mimic the absorption of waves that occurs when US is applied to organs, which is the main contributor to attenuation. The US probe was also submerged into the water, to reduce any attenuation of sounds waves, and then US was directly applied to the microcentrifuge tube for 10 seconds whilst the tube was rotated clockwise at a rate of 0.2 rotations/s. A schematic of the set up can be seen in **Figure 2-3**. The ultra-morphology of US treated blank microspheres was examined using Scanning Electron Microscopy (SEM). Briefly, microsphere samples from the US treated and untreated tubes were placed on silicon wafers and mounted on a SEM stub using double sided carbon tape. These samples were then left to dry overnight in ambient air for 24 h prior to being coated with gold-palladium using an argon beam K550 sputter coater (Emitech Ltd., Kent, England). Once coated, samples were imaged using a Hitachi S-4800 SEM (Hitachi High-Technologies). Particle size distributions were measured from SEM micrographs using ImageJ software.

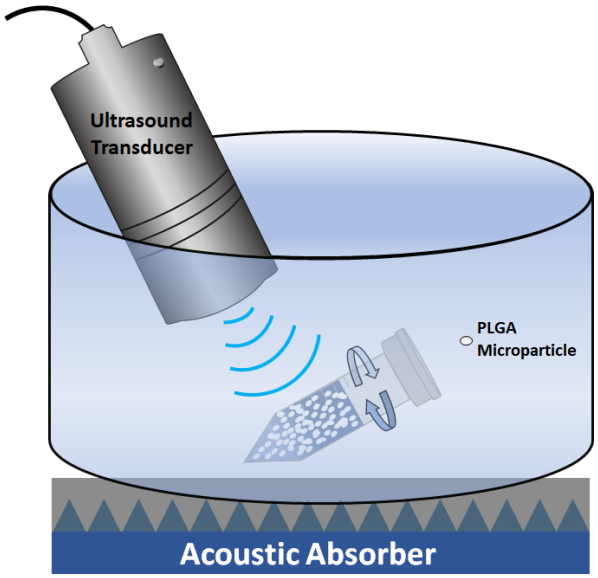

Figure 2-3 : Schematic of the application of US to blank microspheres.

DOX-loaded microspheres (3 mg) were added to amber microcentrifuge tubes containing 1 mL of PBS. After US application (as described in methods section **"Ultra-morphology of blank particles after the application of US"**), the tubes were then placed in a shaker incubator set at 300 rpm and 37°C. Samples were collected after 1, 3, 6, 12, 24, 48, 72, 96, 168, 336, 672, 840, and 1008 h. Sampling involved centrifuging the microcentrifuge tubes at 180*g for 5 minutes from which 300 µl of supernatant was collected. Then 300 µl of fresh PBS was added back to the tubes and the microsphere pellets were resuspended. The collected samples were measured at λ_{ex}485, λ_{em}570 using a SPECTRAmax M5 Microplate Spectrofluorometer (Molecular Devices). These readings were then compared to a standard curve and normalized for photodegradation (data not shown) and weight to determine the amount of DOX released.

Evaluating the effect of blank and DOX-loaded microspheres plus US on cell viability

Cell lines and cell culture

The murine melanoma cell line, B16-F10, was acquired from ATCC and maintained in Dulbecco's modified Eagle's medium (DMEM) (Gibco®, Life Technologies Corporations, NY) supplemented with 10% fetal bovine serum (Atlanta Biologicals, Lawrenceville, GA), 10 mM HEPES (Gibco®), 50 µg/mL gentamycin sulfate (Cellgro, Manassas, VA), 1 mM sodium pyruvate (Gibco®), and 1 mM Glutamax (Gibco®). These cells were incubated at 37 °C and 5% CO_2 in a humidified atmosphere.

Assessing the effect of blank and DOX-loaded microspheres plus US on cell viability in vitro

B16-F10 cells were initially seeded at a density of 1 x 10^5 cells in 4 mL of complete DMEM media in 6-well plates and incubated for 24 h. Then the cells were treated with one of the following treatment systems: untreated/control (no microspheres, no US); US (no microspheres); blank microspheres alone; blank microspheres with US; DOX-loaded microspheres alone; DOX-loaded microspheres with US; and soluble DOX alone. The dose of DOX used (0.5 µg/ml) for all treatment groups was the LD_{50} (for B16-F10 cells as determined from a two day incubation period). The LD_{50} was determined from a study involving B16-F10 cells seeded into wells of a 96-well tray and was simply used as a guide as to what dose to use that would yield sufficient specific cell killing. The amount of blank particles and DOX-loaded microspheres added were comparable. After treatment, cells were incubated for 48 hours and then washed with 1 mL of PBS before being detached from the plate surface with 0.5 mL of 0.25% trypsin-EDTA (1X) (Gibco) for 2 minutes, followed

by 2 mL of complete media to quench the trypsin. Wells were then flushed 5-10 times with a 1 mL pipette to remove additional cells from the plate surface. The cell suspensions were then centrifuged at 230*g for 5 minutes, the supernatant was discarded, and the cell pellets were resuspended in 200 µl of media. Cells were then counted on a hemocytometer using a 1:1 mixture of cells to 0.4 % trypan blue to compare the effectiveness of treatments on cell viability. Cell viability was measured based on the number of live cells within each sample and then comparing these results to the control group. In order to determine if the treatment with DOX-loaded microspheres plus US was synergistic, the percent cytotoxicity generated by this treatment was compared to the combined cytotoxicities of DOX-loaded microspheres alone and US-treated blank microspheres. Prior to comparison the nonspecific cytotoxicity generated by blank microspheres alone was subtracted from all three cytotoxicity values.

US/DOX-loaded microsphere treatment of tumor challenged mice

For tumor challenge, 7 – 10 week old C57BL/6 female mice (5 per group) purchased from Jackson Laboratories (Bar Harbor, ME) were anesthetized by intraperitoneal injection of a ketamine/xylazine mix (87.5 mg/kg ketamine; 2.5 mg/kg xylazine). All animal care, housing and experimental procedures were performed and carried out in accordance with the requirements of the University of Iowa Animal Care and Use Committee. Mice were then challenged with 1 x 10^5 B16-F10 cells by subcutaneous (s.c.) injection (in 100 µL of FBS-free media) into the shaved dorsal right flank. Seven days after tumor challenge, US treatments were applied and repeated on days 7, 8, 9 and 13. After mice were anesthetized,

intratumoral injections of 100 µL of suspended particles or PBS solution were administered. For blank particles, mice were injected with concentrations (w/v) equivalent to the weight of particles delivering the highest dose of DOX. Injections were split into two doses, where 50 µL of the particle suspension would first be injected using an insulin needle/syringe, followed by the application of US for 10 seconds, while keeping the needle inside the injection site to avoid excessive injections. Before the application of US, a smear (enough to cover the US probe and the targeted area) of US transmission gel (Chattanooga Group, Hixson, TN) was applied to the shaved skin surface above the tumor. US, at the settings described in methods section **"Device configuration for US generation"**, was directly applied to the tumor containing the US transmission gel, making sure that the tip of the probe was submerged within the transmission gel. These steps were then repeated for the remaining 50 µL in the insulin syringe. The starting dose of DOX (2 µg) was based on a previous study using DOX-loaded microspheres where intratumoral therapy (without US) was administered.[41, 197] Tumor outgrowth, determined by tumor size as a function of time, was measured multiple times per week and tumor volume was calculated by the equation for determining the volume of an ellipsoid: [(Diameter 1 × Diameter 2 × Height) × (π/6)]. Mice were euthanized when tumors reached or exceeded 20 mm in any direction.

Data Analysis

Data were analyzed and graphed using GraphPad Prism 7. Statistical analyses were performed on cell viability studies using one-way ANOVA followed by a Tukey's multiple comparison test. The Mantel-Cox test was used to analyze survival curves.

Global significance was then followed by a Tukey-Kramer multiple comparison test that compared the means of each group to one another. The cumulative release data (**Figure 2-5A**) were analyzed using nonlinear regression with a two-phase exponential decay function. The initial values and parameter constraints were as automatically provided by the program. Least square fitting was used. The best curve that fitted the data set was selected based on the extra sum-of-squares F-test. Data were presented as mean ± SD, unless stated otherwise. The percent DOX release study at t = 3 h (**Figure 2-5B**) was analyzed using the student t-test (unpaired, two-tailed). All statistical analyses were done based on a 95% confidence interval.

RESULTS

Characterization of DOX-loaded and blank microspheres

SEM images of the fabricated microspheres were analyzed for particle size using ImageJ and blank microspheres were 6.42 ± 1.75 μm (n = 200), while DOX-loaded microspheres were determined to be 6.23± 1.78 μm (n = 200). All microsphere preparations demonstrated smooth surfaced intact spheres. The average loading of a total of 8 batches of DOX-loaded microspheres was 6.76 ± 2.13 μg DOX/mg of PLGA microspheres, while the loading efficiency was approximately 25 ± 8%. The average yield per batch of DOX-loaded microspheres was 113 ± 9.68 mg.

Evaluation of US effects on ultra-morphology of blank microspheres

US was applied to blank microspheres (in water) which were then evaluated, using SEM, for any damaging effects caused by US-induced inertial cavitation. Compared to the untreated microspheres (**Figure 2-4A, 2-4B**), the ultra-morphology of

the microspheres that were treated with US displayed noticeable signs of superficial damage (**Figure 2-4C, 2-4D**). A small percentage (approx. 15%) of microspheres treated with US showed signs of surface damage that may have been caused directly or indirectly (particle collisions) by inertial cavitation. This percentage is likely an underestimation since we can only visualize one face of the microspheres using SEM. Multiple exposures (up to 4x) to blank microspheres did not further increase detectable damage (data not shown). That this damage was not readily detected on microspheres not treated with US nor on US-treated microspheres resuspended in degassed water (**Figure 2-4E, 2-4F**) strongly implicates the involvement of air bubbles already present within the medium (water).

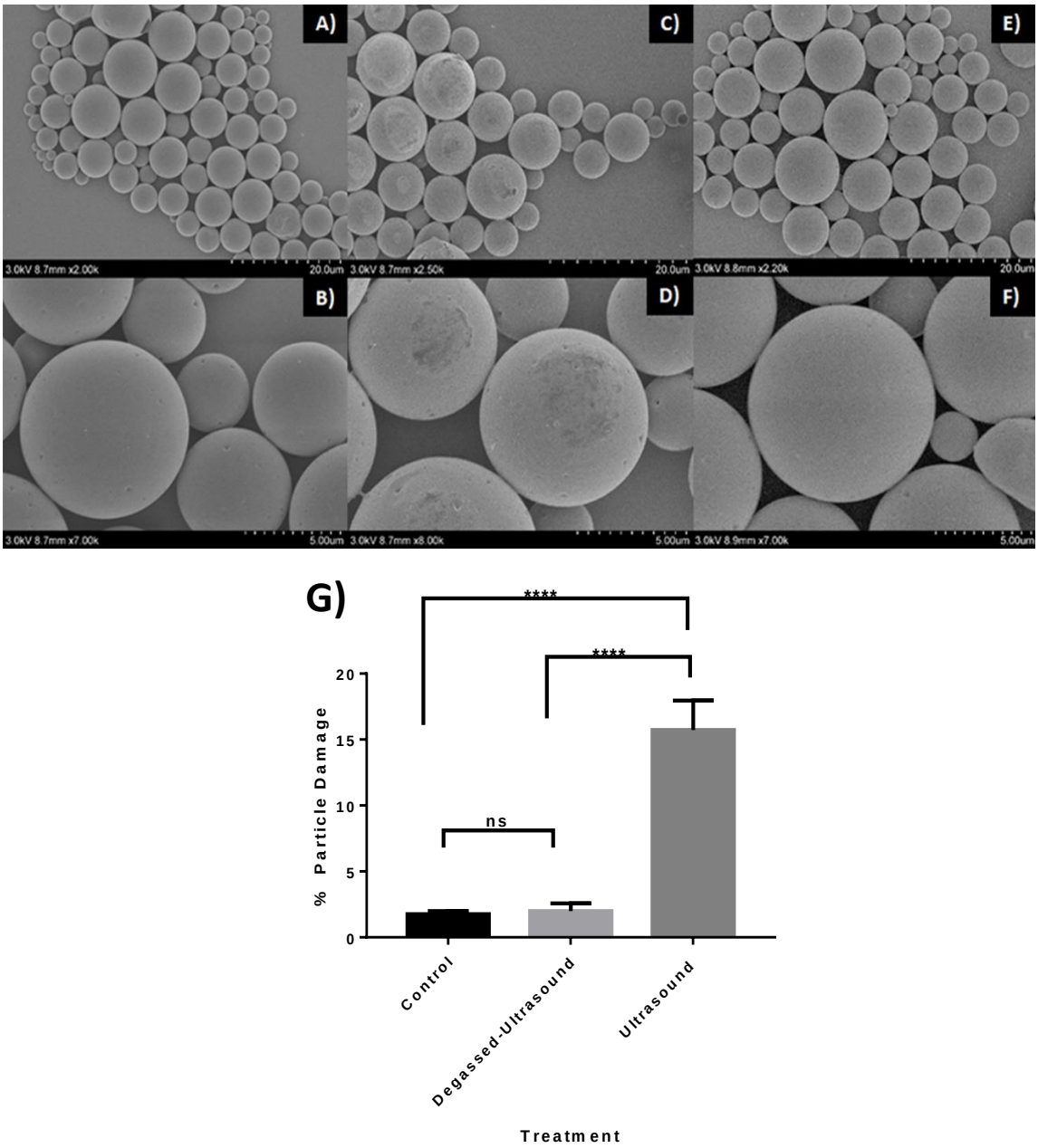

Figure 2-4 : US-mediated damage to the surface of PLGA microspheres. (A-F) SEM images of blank PLGA microspheres either untreated (A,B), or treated with US without degassing (C,D) or with degassing (E,F). (G) Graph illustrating the percent of particles displaying surface damage (E). **** $p < 0.0001$. Error bars represent standard deviation of the mean.

Effect of US on the drug release profile of DOX-loaded microspheres

The effect of US on the release kinetics of DOX from DOX-loaded microspheres was investigated. Comparing release profiles of US-treated versus untreated DOX-loaded microspheres revealed an increased rate of release of DOX by the former. Upon exposure to US, there was an approximately 12% increase in the cumulative release profile compared to the control group (**Figure 2-5**). Analysis using nonlinear regression with a two-phase exponential decay function revealed that cumulative release rates of treated versus untreated microspheres were statistically different ($p < 0.001$) (**Figure 2-5A**). The majority of the enhanced release was observable within 3 h of US treatment and shown to be significant upon analysis of two pooled experiments (**Figure 2-5B**).

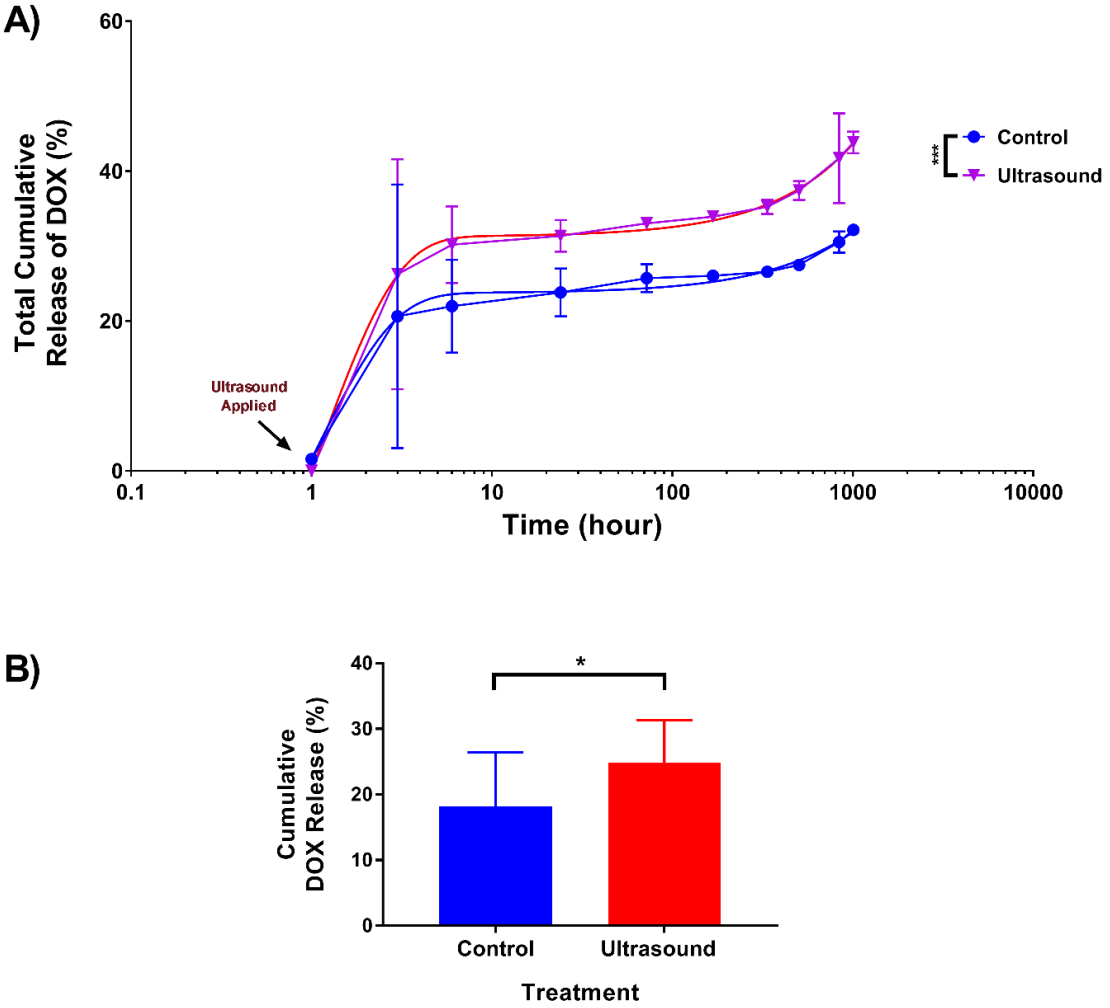

Figure 2-5 : Cumulative release of DOX from DOX-loaded particles with or without US exposure. US was either applied or not applied to DOX-loaded microspheres (loading of 1.94 µg DOX/mg PLGA microspheres), as described in the methods section **"Ultra-morphology of blank particles after the application of US"**. A) Release was subsequently monitored over the indicated time period and showed an enhance burst release of 6% (3 h) and a total increase in 12% over the span of the release study (1008 h). B) Pooled data from 2 experiments (n = 13) comparing percent release DOX from US treated and non-treated microspheres at t = 3 h. *** $p < 0.001$. Error bars represent standard deviation of the mean. Also shown are curves of best fit based on the extra sum-of-squares F-test. * $p < 0.05$.

Effect of the combination of US and DOX-loaded microspheres on killing melanoma cells in vitro.

The effect of US +/- DOX-loaded microspheres on B16-F10 tumor cell viability *in vitro* was investigated. US alone and DOX-loaded microspheres alone provided 23% and 29% tumor cell killing, respectively. Blank microspheres alone caused the least tumor cell death (15%), while DOX in solution alone provided the greatest tumor cell killing (94%). Blank microspheres + US induced 54% killing, while DOX-loaded microspheres + US caused 76% tumor cell killing (**Figure 2-6).** The lower degree of cell death caused by DOX-loaded particles + US compared to DOX in solution can be attributed to the fact that the DOX is encapsulated in the PLGA microspheres and is not completely and immediately available for cells to take up compared to the DOX in solution. With the addition of US to blank microspheres there was a synergistic increase in cell death compared to either treatment alone implicating that inertial cavitation of air bubbles in the presence of microspheres contributed to the cytotoxicity. We speculate that the blank microspheres may have directly damaged cells by physical impact as a result of the forces applied to the microspheres by cavitating air bubbles. When DOX-loaded microspheres were combined with US, synergy was observed (see methods section **"Assessing the effect of blank and DOX-loaded microspheres plus US on cell viability in vitro"** for description of how synergy was calculated) suggesting that US was responsible for enhanced killing of cells by DOX-loaded microspheres due not only to enhanced physical cell damage but also due to enhanced release rate of DOX and/or enhanced permeability of non-lethally damaged cells to soluble/released DOX.

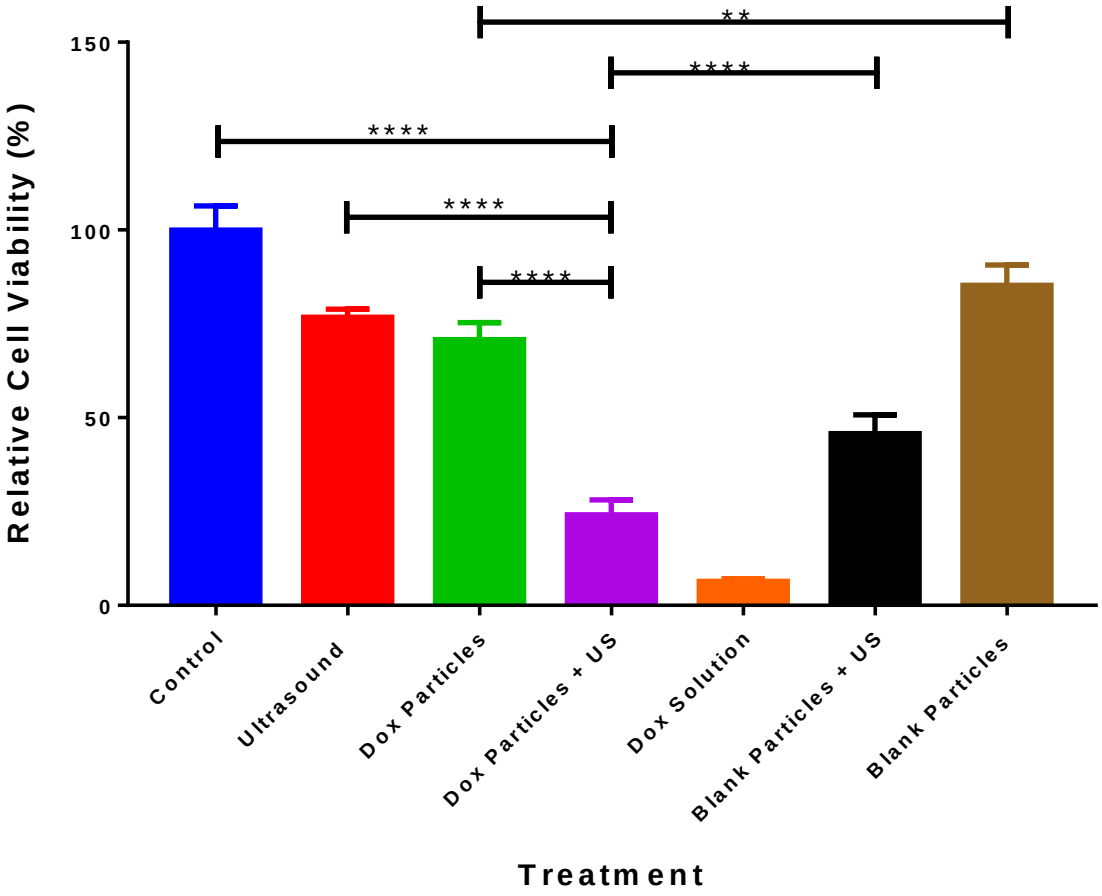

Figure 2-6 : Cell viability of B16-F10 cells treated with particles (w/wo DOX) and/or US. Cells were subjected to treatment and incubated for 48h prior to analysis by counting (see methods section **"Assessing the effect of blank and DOX-loaded microspheres plus US on cell viability in vitro"**). Statistical analysis was performed using one-way ANOVA with a Tukey's multiple comparison test and showed statistical significance between all groups (only a selection is indicated) except for US vs. blank microspheres and US vs. DOX-loaded microspheres. (n = 4, ** $p < 0.01$, **** $p < 0.0001$). Error bars represent standard deviation of the mean.

Effect of the combination of US and DOX-loaded microspheres on survival in a mouse melanoma model

Mice challenged with B16-F10 melanoma cells were treated with intratumoral injections of PBS, blank microspheres, or DOX-loaded microspheres with or without US on day 7 post tumor challenge (see **Figure 2-7A** for regimen). The naïve group treated with PBS had tumors that progressed at a greater rate than other treatment groups (data not shown) and these mice consequently had the lowest mean survival (10.4 days, **Table 2-1**). Statistical analysis revealed that DOX-loaded microspheres (containing 8 μg DOX) plus US was the only treatment to have significant therapeutic benefit over most other groups (**Figure 2-7B**), having a mean survival of 22.1 days compared to 10.4 days for PBS treated mice (**Table 2-1**). This treatment group demonstrated statistically significant extended survival over negative control groups as well as over mice treated with DOX-loaded microspheres (containing 8 μg DOX) alone ($p < 0.05$) or with DOX-loaded microspheres (containing 2 μg DOX) plus US ($p < 0.01$). Mice treated with US as a part of the therapy trended toward longer survival times compared to treatment counterparts without US. In addition, the mice treated with US plus DOX-loaded microspheres (8 μg DOX) exhibited a 13% "cure rate" (**Figure 2-7B**) where "cured" simply means the mice were tumor-free at the conclusion of the survival study (Day 60). It was also noted that survival rates were dose dependent, where higher concentrations of DOX yielded a trend toward increased survival. Based on a combination of encapsulation efficiency and injectable volume limitations (100 μL was the maximum volume feasible intratumorally), the maximum dose we could administer was 8 μg of DOX. Analysis of hazard ratios (**Table 2-1**) revealed the percent chance survival increased

synergistically from 6 percent for mice treated with blank microspheres plus US and from 34.1% for mice treated with DOX-loaded (8 µg) microspheres alone, to 74% for mice treated with DOX-loaded (8 µg) microspheres plus US. This synergy may be at least partially explained by the additional role of DOX as an inducer of immunogenic apoptosis where the host's immune system is stimulated to recognize the B16-F10 melanoma cells as foreign by the induction of tumor specific T cells. Thus, we chose to add an immune checkpoint blocker (anti-PD-1) to the most effective treatment group, DOX-loaded (8 µg) microspheres plus US, to see if this could further improve survival outcome by enhancing any tumor-specific effector T cell response. No significant increase in survival was observed (**Figure 2-7C**), suggesting either that the impact of DOX-loaded microspheres/US on the effector arm of the immune response may have been limited or that the immune checkpoint axis of PD-1:PDL1 was not of significant influence in suppressing any induced antitumor immune response. In addition, at day 90 subsequent to initial tumor challenge, all "cured", or tumor-free, mice were rechallenged by subcutaneous injections of 1 x 10^5 B16-F10 cells (contralateral to original challenge), in a similar manner to that described in methods section **"US/DOX-loaded microsphere treatment of tumor challenged mice"**. All mice developed detectable tumors within 2 weeks of rechallenge demonstrating the lack of a protective adaptive immune response (data not shown).

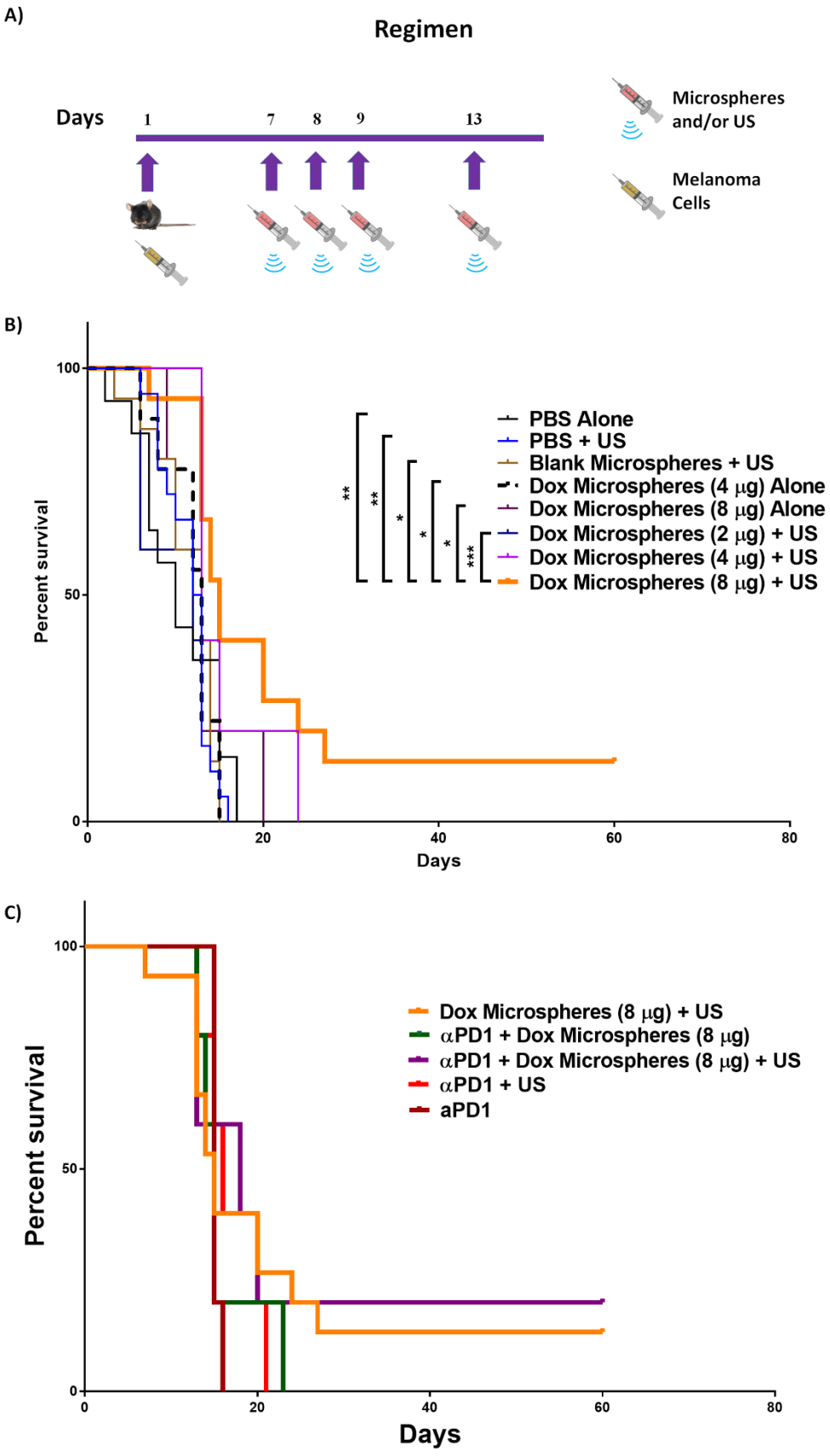

Figure 2-7 : Survival study of in vivo tumor therapy. A) Tumor challenge and treatment regimen. B) Survival curve (pooled data) of tumor (B16-F10) challenged mice that received the following treatments on indicated days: PBS only (n = 14), PBS + US (n = 18), blank particles + US (n = 15), DOX-loaded particles (4 μg) alone (n = 9), DOX-loaded particles (2 μg) + US (n = 5), DOX-loaded particles (4 μg) + US (n = 10), and DOX-loaded particles (8 μg) alone (n = 5), DOX-loaded particles (8 μg) + US (n = 15). A Mantel-Cox test was performed to analyze the survival distribution yielding a p-value of 0.0110. This global significance was then followed by a Tukey-Kramer post-test with multiple comparisons * $p < 0.05$, ** $p < 0.01$, *** $p < 0.001$. C) Survival curve comparing mice treated with DOX-loaded particles (8 μg) + US and/or anti-PD1, where all anti-PD1 groups were n = 5.

Table 2-1 : Mean survival times for tumor-challenged mice receiving indicated treatment.

Treatment	Mean Survival (Day)	Hazard Ratio (95% CI)
PBS Alone	10.4	1.00
PBS + US	11.3	1.09 (0.540, 2.21)
Blank microspheres + US	11.5	0.939 (0.448, 1.96)
DOX-loaded microspheres (4 μg) alone	11.6	0.927 (0.399, 2.15)
DOX-loaded microspheres (8 μg) alone	13	0.659 (0.233, 1.86)
DOX-loaded microspheres (2 μg) + US	10	1.46 (0.518, 4.13)
DOX-loaded microspheres (4 μg) + US	15.3	0.447 (0.196, 1.02)
DOX-loaded microspheres (8 μg) + US	22.1	0.259 (0.113, 0.593)

DISCUSSION

In this study, we demonstrated the tumoricidal benefits of combining DOX-loaded microspheres with US. We speculate that the combination of: 1) physically based cell killing/damage mediated directly or indirectly (microsphere collisions) by US, 2) chemically based killing mediated by DOX, and 3) enhanced release rate of DOX from US-treated PLGA microspheres likely contributed to the observed enhanced tumor cell killing *in vitro* and greater survival *in vivo* when compared to DOX-loaded microspheres alone or US/blank microspheres alone. Microspheres treated with US *in vitro* were observed to have undergone discernible and quantifiable superficial damage (see SEM images, **Figure 2-4**). Such damage can be visualized as disrupted uniformity at the surface of the particles. Since the surface damage is not observed on US treated microspheres in degassed medium (**Figures 2-4E-G)** we speculate that the damage is attributed to the process of inertial cavitation of proximal air bubbles that are capable of damaging the particles directly and/or indirectly by inducing interparticle collisions.[176]

The application of US to DOX-loaded microspheres *in vitro* was shown to increase the rate of release of DOX from the microspheres (**Figure 2-5**) which we propose may have been a direct result of the damage described above (**Figure 2-4**). Whether the increase in release rate of DOX was due to the direct impact of air bubbles undergoing inertial cavitation, the impact of particle:particle collisions (caused indirectly by the inertial cavitation of air bubbles) or a combination of the two is unknown. Nevertheless, the application of US provides the opportunity for controllable drug release. In addition to the US-inducible increased rate of drug release from the nonechogenic PLGA microspheres, these microspheres have the

added advantage of simultaneously providing sustained drug release since only a fraction of the DOX payload is stimulated to be released upon US treatment.[41, 168] This is in contrast to the immediate payload release that results when echogenic particles are used.[198-200]

Cell viability studies were performed to assess the effects of combinations of US +/- DOX-loaded particles on B16-F10 melanoma tumor cells *in vitro* (**Figure 2-6**). Although DOX solution exhibited the highest tumor cell death (94%), this is not a viable direction for treating melanoma in the clinic due to: 1) the vesicant properties of soluble DOX, particularly if administered intratumorally, as well as 2) the undesired acute and chronic toxicities that result from soluble DOX.[201-202] Thus, soluble DOX was used *in vitro* as a positive control. Excluding the soluble DOX-treated group, tumor killing was greatest (76%) when cells were treated with DOX-loaded microspheres plus US. We speculate this to be due to a synergistic effect resulting from the presence of microspheres/US causing physical cell damage [203] plus the cytotoxicity generated by released DOX [204] where the rate of release increased upon US treatment (**Figure 2-5**). The statistically significant difference in cytotoxicities between DOX-loaded microspheres and blank particle treatments confirm that DOX *released* from these particles impacted on cell viability since uptake of DOX-loaded microspheres would be unlikely due to their excessive size. US alone did cause a small amount of cell killing, which we propose was most likely through sonoporation/inertial cavitation, where the intensity of the US causes irreversible damage to the cell membrane.[180] The degree to which the increased release of DOX from the US-treated microspheres contributed to the increased cytotoxicity is difficult to assess since the combination of US and microspheres may have increased cell

permeability to DOX, therefore potentially further contributing to the observed cytotoxicity of DOX regardless of the enhanced release.[205]

An *in vivo* murine melanoma model was employed to observe the effect of combining US and intratumorally administered DOX-loaded microspheres on survival (**Figure 2-7**). Supporting the findings from the *in vitro* experiments, the combinatorial treatment of tumors with DOX-loaded microspheres (8 µg) plus US was the most effective treatment group, as demonstrated by longer survival times and 13% tumor-free mice ("cured") at the termination of the survival study (Day 60). US, when combined with DOX (4 µg or 8 µg)-loaded microspheres, enhanced survival times compared to the same treatment groups without US. In particular, when the treatments with DOX (8 µg)-loaded microspheres in the presence and absence of US were compared, a significant difference was observed ($p < 0.05$). However, US alone or in combination with blank microspheres only had a marginal and non-significant impact on survival. This contrasted with the *in vitro* data where US alone and the combination of US and blank microspheres were significantly cytotoxic. Such findings suggest that the cell death directly caused by physical damage to melanoma cells *in vivo* was likely to have been minimal. It has been shown that the impact of US on cell viability is indirectly correlated to cell density [206], and therefore tumor cell killing *in vitro* would have been expected to be higher than it would be for a densely packed tumor mass. Thus, we propose that the synergy observed *in vivo* when US and DOX (4 µg or 8 µg)-loaded microspheres were used in combination may have stemmed from US-mediated enhanced cell permeability [205], through the generation of non-lethal cell membrane damage thereby resulting in increased uptake of DOX. Support for this comes from the recent finding that US alone can increase cancer cell uptake of

chemotherapeutic agents.[207] That US could induce an increased release of DOX was demonstrated *in vitro* (**Figure 2-5**), however, whether it occurred *in vivo* to the same or any extent is uncertain since this was not easily measurable. Nevertheless, it is a possible explanation for how the combinatorial treatment may have at least partially contributed to the observed synergistic effect *in vivo*.

Another possible interpretation of the observed synergy was that a mode of killing aside from US/microsphere mediated physical damage and direct DOX-mediated cytotoxicity occurred. One possibility that we considered was that some amount of immune based killing was generated through the ability of DOX to induce immunogenic apoptosis of tumor cells.[181] However, when the mice surviving ("cured") from treatment with DOX-loaded (8 μg) microspheres plus US were subsequently rechallenged with B16-F10 cells they succumbed to the tumor therefore suggesting that the adaptive immune response may not have played a role in the enhanced survival caused by the combinatorial treatment. This likely lack of immune involvement in tumor cell killing is further supported by the finding that immune checkpoint blockade (anti-PD1) could not significantly extend survival of mice treated with DOX-loaded microspheres plus US (**Figure 2-7C**). It would have been desirable to have generated a detectable antitumor immune response as this would have benefits for the treatment of metastatic melanoma due to the generation of a potential abscopal-like response. In order to address this, it may be necessary to include additional chemotherapeutic agents capable of promoting antitumor T cell responses when used in combination with DOX, such as cyclophosphamide.[182]

To the best of our knowledge this is the first study using drug loaded microspheres in combination with US that go on to test cytotoxic impact in an *in vitro*

and *in vivo* cancer cell system. The results from the melanoma mouse model, whilst promising, indicate that there is room for generating improved efficacy through formulation modifications and these potential adjustments may stem from findings from independent sources. Other researchers have implemented US as a method of promoting pulsatile drug release, using cross-linked hydrogels containing mitoxantrone for the treatment of breast cancer in preclinical in vivo studies.[208] The researchers found that providing US to gels *in vivo* marginally, but not significantly, improved the anti-tumor activity of the mitoxantrone compared to gels not treated with US, and suggested that spatial and temporal optimizations can be performed to maximize drug efficacy. Another approach, using US with DOX-liposome-loaded microbubbles, has been shown to kill melanoma cells *in vitro*, however, this system does not provide a means of sustained drug release since the majority of the payload is released upon US treatment.[209] The application of US on microspheres loaded with anti-cancer agents such as DOX has the potential to be used as a cancer treatment system, possibly in combination with a cancer vaccine and/or intraoperatively upon resection of superficial lesions. The former may boost the possibility of an effective systemic immune response, whilst the latter would reduce the chances of local tumor recurrence. The above system can be considered as a potential treatment for melanoma patients with skin lesions readily accessible to treatment.

CONCLUSION

We initially assessed the efficacy of a controlled drug delivery system for the treatment of cancer using on-demand, and sustained, release of an anticancer drug, doxorubicin (DOX), for the treatment of melanoma in a murine model. Using a

melanoma model, we investigated the antitumor potential of combining ultrasound (US) with poly(lactic-co-glycolic acid) (PLGA) microspheres loaded with DOX. An *in vitro* release assay demonstrated an ability of US to affect the release kinetics of DOX from DOX-loaded PLGA microspheres by inducing a 12% increase in rate of release where this treatment resulted in synergistic tumor cell (B16-F10 melanoma cells) killing. Melanoma-bearing mice treated intratumorally with DOX (8 μg)-loaded microspheres and subjected to US treatment at the tumor site were shown to significantly extended survival compared to untreated mice or mice subjected to either treatment alone. Our system provides a means of US-triggered enhanced drug release, as well as retaining a sustained release profile since the PLGA microspheres were only partially affected by US treatment when measured *in vitro*. Adjustments in polymer chemistry, molecular weight, and crystallinity will affect the hydrolysis rate (DOX release) as well as mechanical properties (response to applied force) of the formulation, resulting in varying susceptibilities to US. It would also be valuable in future approaches to explore the implementation of multiple US treatments of tumors containing DOX-loaded microspheres so as to generate a pulsatile release profile as Huebsch et al. obtained with their treatment system.[208] Further optimization is required to provide a systemically deliverable nanoparticle version capable of targeting metastasized lesions. Nonetheless, the synergistic increase in survival of melanoma-challenged mice treated with the combination of US and DOX-loaded microspheres implicates a such a treatment methodology as a promising additional tool for combatting an otherwise currently incurable cancer. The efficacy of these controlled drug delivery systems to treat cancer led to the investigation of more

novel controlled drug delivery systems such as 3D printing compared to the conventional microparticle controlled drug delivery.

CHAPTER 3 : CONTROLLED AND SEQUENTIAL DELIVERY OF FLUOROPHORES FROM 3D PRINTED ALGINATE-PLGA TUBES

INTRODUCTION

The ability to control the means by which drugs are delivered, whether through pulsatile [210-212], sequential [37, 213], or on-demand release [42], has the potential to provide more effective dosage regimens and enhanced therapeutic effects for various diseases and injuries. Not only do these systems have the potential to increase the efficacy of current drugs, they could also help to address many patient compliance and adherence issues caused by forgetfulness [6], complicated dosage schedules [7], and inability to physically handle the drugs.[8] In the research presented here, we utilize two distinct fluorophores as model drug molecules to demonstrate a "proof of concept" 3D printed PLGA filled alginate tube capable of controlled sequential drug release. Sequential release involves a differential temporal release of two or more agents. Sequential release has been demonstrated using titania (TiO_2) nanotubes and polymer micelles to sequentially deliver both hydrophobic (indomethacin and itraconazole) and hydrophilic (gentamicin) drugs.[37] Sequential drug release has also provided a potential cancer treatment system where the sequential release of ibandronate and tamoxifen has been reported to act synergistically in preventing the proliferation of an estrogen receptor-positive breast cancer cell line, MCF7.[38] Sequential drug release may also be beneficial for tissue engineering. For example, a silica calcium phosphate nanocomposite scaffold has been developed that is capable of controlled drug delivery, initially providing protection from infection through the release of an antibiotic, followed by the release of a bone morphogenetic protein.[214]

The impact of three-dimensional (3D) printing in a range of industries is already evident and this technology is expected to have increasing applications in many biomedical applications with advancements in printer performance and resolution [33, 215], and the emergence of new bioprinting technologies.[216] 3D printing of tablets has demonstrated the potential for controlled release of drugs.[217-221] Here, we aimed to build on these previous tablet-based technological innovations and demonstrate for the *first* time the controlled and sequential release of distinct fluorophores from 3D printed PLGA and alginate hybrid tubes. Three-dimensional bioprinting of alginate tubes using a coaxial extrusion-based system was recently carried out to mimic natural vascular networks with the ultimate aim of generating blood vessels during scale-up tissue fabrication.[32, 222-223] Here, we have 3D printed a drug delivery device capable of sequential drug delivery by utilizing a double layer system. The delivery system comprises a 3D-printed (through a coaxial extrusion system) alginate tube housing a poly (lactic-co-glycolic acid) (PLGA) core. The PLGA core was added to fortify the structural integrity of the alginate tube as well as to provide versatility with respect to controlled drug delivery applications(See Chapter 2: **"PLGA"** section for more information).[224] In addition, PLGA is a Food and Drug Administration (FDA) approved biocompatible and biodegradable polymer that has been used in many drug delivery systems.[225] Thus, in the study presented here, tubes comprising 4% w/v alginate (shell) and 1% (w/v) PLGA (core) (alginate-PLGA tubes) were fabricated, and tested for controlled sequential delivery of different fluorophores. Biocompatibility of the alginate-PLGA tubes used in our studies was assessed through cytotoxicity assays using a human embryonic kidney cell line, HEK293, and bone marrow stromal cells (BMSCs). Mechanical analysis was

performed to test compressive strengths of various alginate versus alginate-PLGA tubes ± fluorophores in order to assess the contribution of the PLGA core to the mechanical strength of the tubes as well as testing if the integrity of the tubes was load-dependent. The development of these alginate-PLGA tubes through 3D coaxial-extrusion-based printing provides a unique drug delivery system capable of sequential release. Such devices have the potential to be used in a multitude of applications, including but not limited to, scaffold fabrication for bone regeneration and cancer vaccine/therapy implants.

Sodium alginate

Sodium alginate (**Figure 3-1**) is the sodium salt form of alginic acid which is a natural polymer derived from brown seaweed. Sodium alginate is often used for biomedical applications due to its biocompatibility, minimal toxicity, low cost, and ease of gelation through the addition of divalent ions, such as divalent calcium.[226] Alginate consists of linear copolymer blocks of (1,4)-linked β-D-mannuronate (M) and α-L-guluronate (G) residues. The blocks are composed of consecutive G residues (GGGGGG), consecutive M residues (MMMMMM), or alternating M and G residues (GMGMGM). However, only the G-blocks of alginate are speculated to participate in intermolecular cross-linking with divalent cations to form hydrogels, where increasing the length of the G-block results in higher mechanical properties.[226-227] Alginate hydrogels are typically prepared by crosslinking with $CaCl_2$ to form structures that have used for: wound dressing to promote healing[228], controlled drug delivery[229], and as composites for tissue regeneration.[230] Alginate is inherently non-degradable in mammals due to the lack of the alginase enzyme, however, ionically cross-linked

alginate gels can be dissolved by the release of divalent ions used in the cross-liking process into the surrounding media due to exchange reactions with monovalent cations such as sodium ions. An attractive approach to making alginate more degradable at physiological conditions includes the partial oxidation of alginate chains. An issue with this degradation process is that there is no hydrolytic or enzymatic chain breakage that occurs within alginate chains under physiological conditions. The issues are resolved through the oxidation of the alginate hydrogels, where the degree of oxidation of the uronic acid residues is directly proportional to the rate of degradation. Care should be taken at higher levels of oxidation because, at these levels, the oxidation can interfere with the gelation process.[231] Other factors that can affect the rate of degradation of alginate hydrogels are pH and temperature.[226, 232]

In order to reduce the burst release of drugs from traditional hydrogel matrices, pH sensitive sodium alginate/hydroxyapatite (SA/HA) nanocomposite beads were prepared and loaded with diclofenac sodium. The release of sodium diclofenac was prolonged by 8 h compared to sodium alginate hydrogel beads because the SA/HA microparticles acted as inorganic crosslinkers in the nanocomposites causing the SA polymer chains to contract and restrict movability resulting in a slower rate of swelling and dissolution.[233] In another study, chitosan-alginate scaffolds were fabricated for bone tissue engineering, where, when incubated in vitro with MG63 osteoblast cells, the cells were able to attach and proliferate to promote the deposition of minerals without osteogenic medium. The osteogenic properties of these scaffolds were further confirmed in skeletally mature female adult Sprague–Dawley rats to promote rapid vascularization and calcium

deposition as early as the fourth week after implantation.[234] Alginate is a vital natural material that can be used for a variety applications involving controlled drug release or providing stability to scaffolds in tissue engineering.

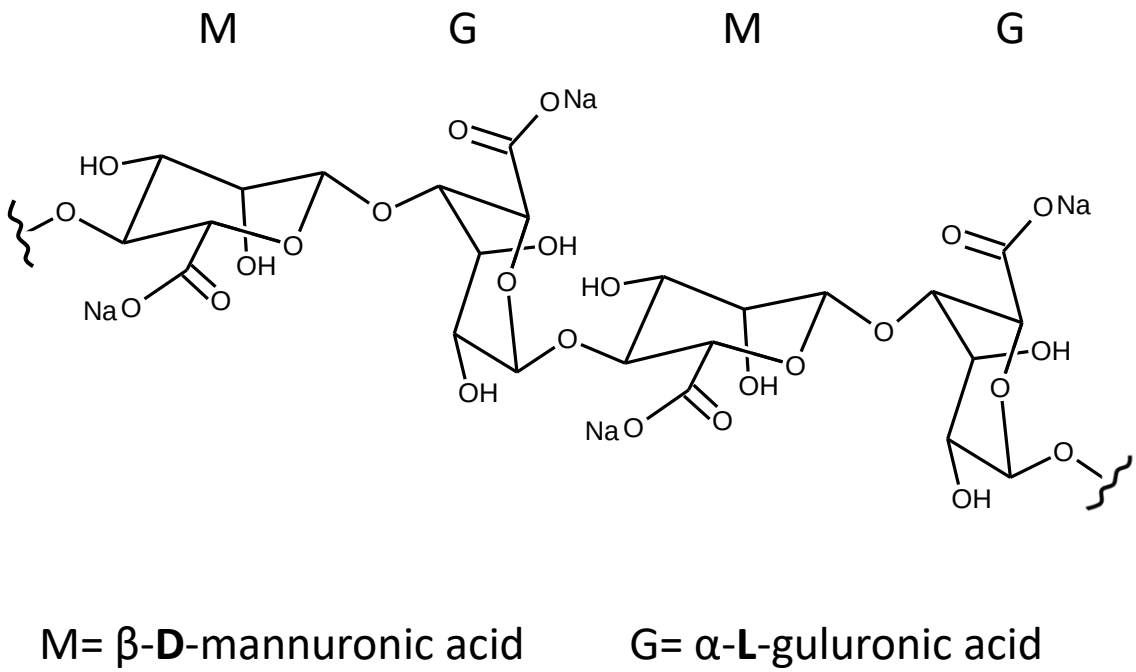

M= β-**D**-mannuronic acid G= α-**L**-guluronic acid

Figure 3-1 : Chemical structure of sodium alginate.

MATERIALS AND METHODS

Alginate-PLGA tube fabrication

Sodium alginate (Sigma, St. Louis, MO) was used as the tube sheath material and calcium chloride ($CaCl_2$) powder (Sigma) was used as a crosslinking agent. Sodium alginate (4% w/v) and $CaCl_2$ (4% w/v) were each dissolved in sterile deionized water. The fabrication system consisted of a single-arm robotic printer (EFD® Nordson, East Providence, RI) controlled by a proprietary computer system and a homemade coaxial nozzle unit connected to a pneumatic air dispenser (EFD® Nordson) and a mechanical pump (New Era Pump System Inc., Farmingdale, NY) for

alginate and $CaCl_2$ extrusion, respectively (**Figure 3-2A**). The coaxial nozzle comprised a 14-gauge outer needle and a 22-gauge inner needle (**Figure 3-2B**). Alginate precursor solution was dispensed through the sheath section of the coaxial-nozzle unit while $CaCl_2$ solution was dispensed through the core section. The alginate dispensing pressure was set at 82.7 kPa and the $CaCl_2$ dispensing rate was set at 16 mL/min. The 3D printed alginate tubes were then soaked overnight in 4% $CaCl_2$ solution to allow complete crosslinking. Poly (lactic-co-glycolic acid) 50:50 (RG503, Evonik, Darmstadt, Germany) was dissolved in chloroform (Sigma) at a concentration of 1% (w/v) and was then injected into the alginate tubes using a custom syringe unit (Hamilton Company, Reno, NV, USA). These PLGA-loaded alginate tubes, or alginate-PLGA tubes, were then clamped together by surgical micro-vessel clips (30 g) (World Precision Instruments, Sarasota, FL). The alginate-PLGA tubes were soaked for 48 h in deionized (DI) water to achieve maximum crosslinking and to prevent leakage. This soaking process also performed the function of potentially washing away any residual chloroform or chemical impurities.

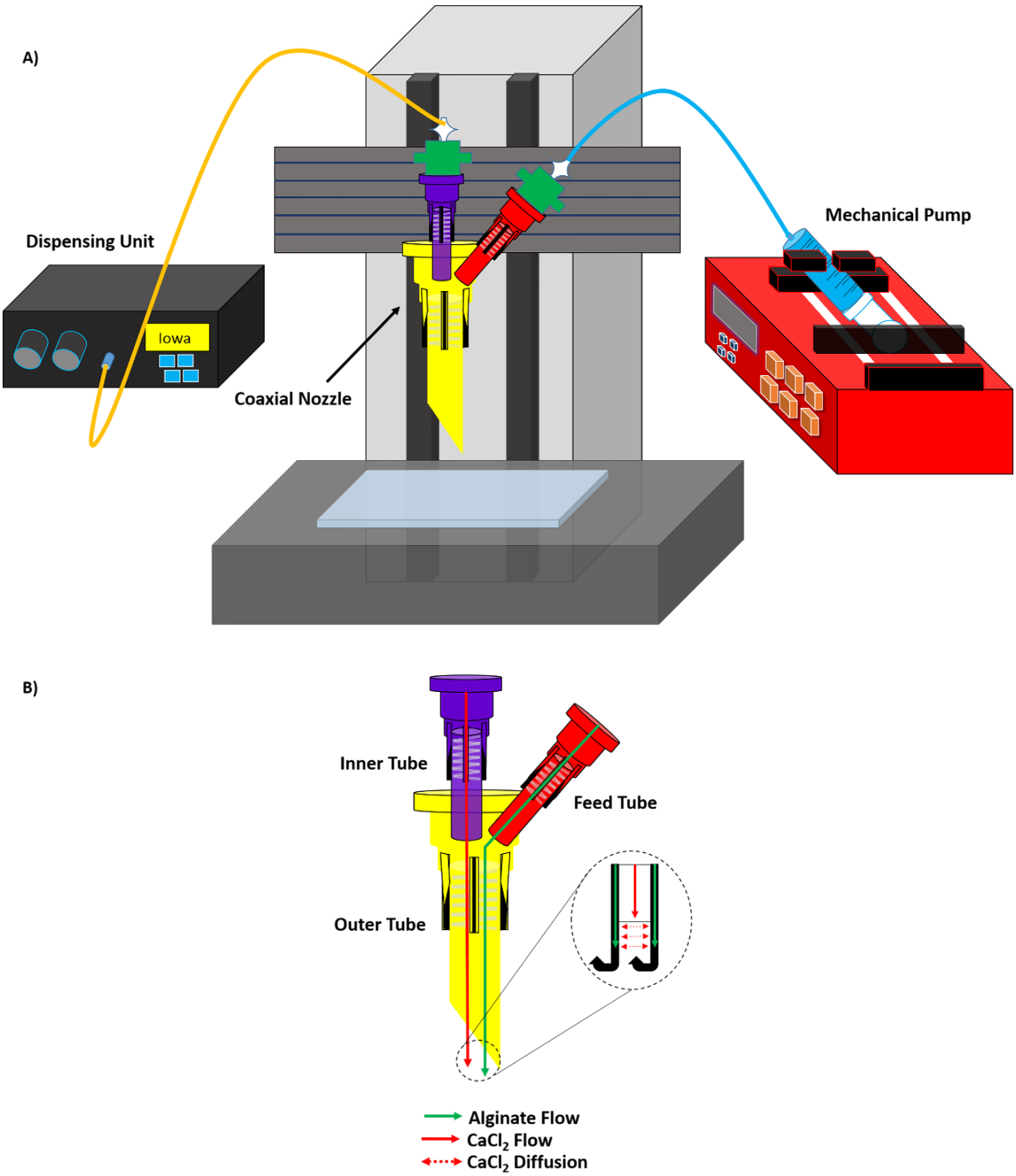

Figure 3-2 : Schematic of the extrusion printing systems. A) Schematic of the coaxial extrusion printing system utilizing a mechanical pump to extrude sodium alginate (blue fluid) and a dispensing unit to introduce $CaCl_2$ (yellow fluid). B) Illustration of the coaxial nozzle used to print alginate conduits tubes, where the hydrogel flow contains the sodium alginate and $CaCl_2$ solutions in the sheath and core sections, respectively.

Morphology imaging of alginate-PLGA tube

Alginate shell and PLGA core layers were visualized and imaged using an optical microscope. From these images, the layer diameters were measured using the open source ImageJ software. The ultra-morphology of alginate-PLGA tubes was examined using Scanning Electron Microscopy (SEM). Samples were placed on aluminum stubs and left to dry overnight in ambient air for 24 h prior to being coated with gold-palladium using an argon beam K550 sputter coater (Emitech Ltd., Kent, England). Once coated, samples were imaged using a Hitachi S-4800 SEM (*Hitachi* High-Technologies, Tokyo, Japan).

Fluorophore release study

Release studies were performed with tubes comprising 4% (w/v) alginate (shell) and 1% (w/v) PLGA (core) where fluorescein (Molecular Probes, Eugene, OR) was mixed with alginate and rhodamine B (Sigma, St. Louis, MO) was mixed with PLGA. These fluorophores were chosen due to their distinct (non-overlapping) excitation and emission wavelengths. Alginate-PLGA tubes containing both dyes were made with one concentration of fluorescein (0.025 mg/ml) and either of two concentrations of rhodamine B (0.80 mg/ml (R1) or 0.40 mg/ml (R2)). These concentrations were chosen due to the solubility and the detection limits of the fluorophores. The two concentrations of rhodamine B were also selected to observe any concentration dependent effects on alginate-PLGA tube stability and fluorophore release. Alginate-PLGA tubes of 5 cm length were created by cutting with a surgical blade, ensuring that each section did not contain air bubbles. The cutting process also provided a means to close off the ends of the tubes because the pressure

applied by the incision created a seal at each end. These alginate-PLGA tubes were added singly to scintillation vials containing 3 mL of phosphate-buffered saline (PBS) and then placed in a shaker incubator set at 300 rpm and 37°C. Care was taken to submerge the alginate-PLGA tubes in the 3 mL of PBS. In order to mitigate photodegradation of fluorophores, the vials were covered with aluminum foil. Samples were collected after 1, 3, 6, 12, 24, 48, 72, 120, and 168 h. Sampling involved removing 200 µl from the vial (being cautious to avoid sampling remnants of the alginate-PLGA tubes) and then 200 µl of fresh PBS was added back to the vials. The samples were measured for fluorescein (λ_{ex}494, λ_{em}521) and rhodamine B (λ_{ex}540, λ_{em}625) fluorescence using a SPECTRAmax M5 Microplate Spectrofluorometer (Molecular Devices, San Diego, CA). These readings were then compared to a standard curve to determine the amount of each fluorescence dye released. In addition, degradation (or loss of fluorescence) of the fluorophores was taken into account by monitoring (at t = 0, 1, 3, 6, 12, 24, 49, 120, 144, and 168 h) the concentrations of both fluorophore solutions in PBS in parallel samples at starting concentrations of 0.025 mg/ml fluorescein and 0.8 mg/ml rhodamine. The degradation of the fluorophores yielded a degradation rate equation of y = 7.7 ln(x) + 100 for fluorescein and y = -2.1 ln(x) + 98 for rhodamine B (**Figure 3-3**). Using these equations, the release study data were adjusted to account for any fluorophore degradation.

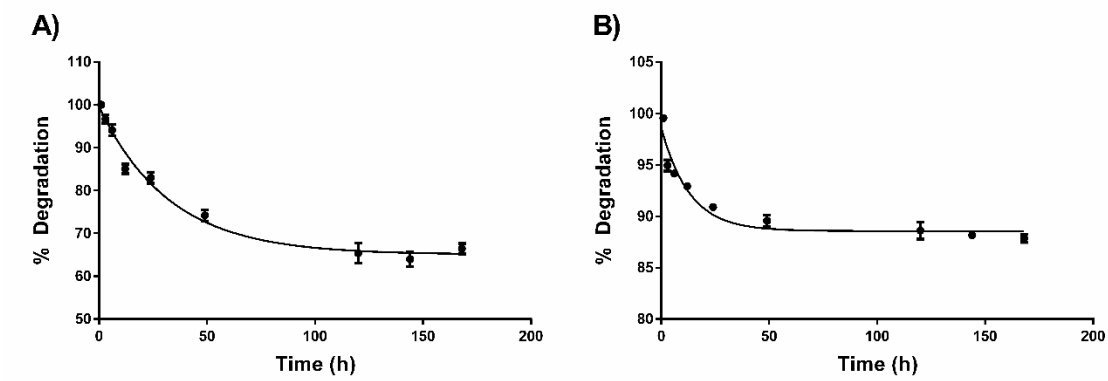

Figure 3-3 : Degradation curves for: A) fluorescein (λex494, λem521) and B) rhodamine B (λex540, λem625).

Individual release of fluorophore from polymers

Release studies were performed with polymer and fluorophore combinations comprising either 4% (w/v) alginate (shell) or 1% (w/v) PLGA (core) with either fluorescein or rhodamine B. Alginate hydrogel was combined with rhodamine solution to yield a 0.80 mg/ml solution, while PLGA was solubilized and mixed with fluorescein or rhodamine B to yield a polymer-fluorophore mixture of 0.025 mg/ml and 0.80 mg/ml, respectively. Samples in one mL volumes of each desired polymer-fluorophore combinations were made, to which 3 mL of PBS was added and then placed in a shaker incubator set at 300 rpm and 37°C and were covered with aluminum foil. Samples were then collected after 1, 3, 6, 12, 24, 48, 72, 120, and 168 h. Sampling involved removing 300 µl out of each vial and replacing with 300 µl of PBS. The samples were measured for fluorescein (λ_{ex}494, λ_{em}521) and rhodamine B (λ_{ex}540, λ_{em}625) fluorescence using a SPECTRAmax M5 Microplate Spectrofluorometer (Molecular Devices). The readings were compared to a standard curve and photodegradation equations applied to normalize the results.

Evaluating cell viability and cytotoxicity

Cell lines and cell culture

Human embryonic kidney 293 (HEK293) cells and bone marrow stromal stem cells (BMSCs) were purchased from the American Type Culture Collection (ATCC, Rockville, MD) and were maintained in Dulbecco's modified Eagle's medium (DMEM) (Gibco®, Life Technologies Corporations, NY) supplemented with 10% fetal bovine serum (Atlanta Biologicals, Lawrenceville, GA), 10 mM HEPES (Gibco®), 50 µg/mL gentamycin sulfate (Cellgro, Manassas, VA), 1 mM sodium pyruvate (Gibco®), and 1 mM Glutamax (Gibco®). Both cell types were incubated at 37 °C and 5% CO_2 in a humidified atmosphere.

Evaluation of Alginate-PLGA Tubes on Cell Viability

Cell viability studies were performed using an MTS assay (CellTiter 96®, Promega, Madison, WI). The MTS assay was performed following manufacturer's instructions. In brief, cells were plated in a 96-well plate at a density of 1 x 10^4 cells/well in 100 µl of DMEM (+ supplements) for 24 h prior to treatments. The media was then aspirated, and fresh media was added along with alginate-PLGA tubes of different lengths. The cultures were then incubated for 24 h, after which the alginate-PLGA tubes were removed, the media was aspirated and then replaced with fresh media. It was also crucial to ensure during media removal, no remnants of the alginate-PLGA tubes remained in the well because this could affect absorbance readings. Then, 20 µl of MTS reagent was added and cells were incubated for a further 2 h. The absorbance was determined at 490 nm using a SpectraMax plus 384 Microplate spectrometer (Molecular Devices, Sunnyvale, CA). Relative cell viability was analyzed using untreated cells as the control group. The resultant

absorbance of the soluble formazan at 490 nm is directly proportional to the cellular metabolic activity of living cells in each well.

Mechanical analysis

Mechanical properties were measured using a dynamic mechanical analyzer (DMA Q800 V7.0 Build 113, TA Instruments, New Castle, DE) equipped with a submersion compression clamp in static mode. Prior to the measurements, the drive shaft position, clamp mass, clamp offset, and clamp compliance were calibrated according to the protocols suggested by the manufacturer. The samples were cut with a razor blade to be ~10 mm in length and the exact length and diameter of each sample was measured using calipers. Each sample was carefully transferred to the basin of the DMA clamp using forceps and the top portion of the clamp was gently lowered onto the sample. A preload force of 0.0001 N was initially applied and the force was then increased to a final value of 0.2 N at a rate of 0.02 N/min. Data were collected every 2 seconds as each sample was compressed. The stress was plotted against strain data with the slope of the line representing the compressive modulus of the sample.

Data analysis

Data were analyzed using GraphPad Prism 6. All graphs were generated using GraphPad Prism 6. Statistical analysis was performed using one-way ANOVA, followed by the Dunnett's multiple comparison test to compare the experimental group with a

single control group. All error bars represent standard deviation. All statistical analyses were done based on a 95% confidence interval.

RESULTS

Visualization and dimensions of alginate-PLGA tubes

Alginate tubes were printed through coaxial extrusion and then manually injected with PLGA. The fabricated device can be seen in **Figure 3-4**. The two layers were visualized using light microscopy (**Figure 3-4B**). With the addition of rhodamine B mixed into PLGA, it could be seen that the dye was homogenously mixed and dispersed throughout the core of the alginate-PLGA tube (**Figure 3-4C**). The diameters of the alginate-PLGA tubes ranged from 1.5 - 1.7 mm; however, tubes could be extruded to any length. The thickness of the alginate sheath layers and the PLGA cores were 140 ± 14 μm and 1,200 ± 120 μm, respectively. Scanning electron microscopy images were also captured to visualize the surface morphology of the alginate-PLGA tubes (**Figure 3-4D**). The small variation in diameter (1.5 – 1.7 mm) of the alginate-PLGA tubes may have been caused by the inherent variability associated with the manual injection of the PLGA solution that can result in a non-uniform dispersal of PLGA within the alginate tubes. This process of injection of the core solution will be automated in the future in an attempt to reduce diameter variability.

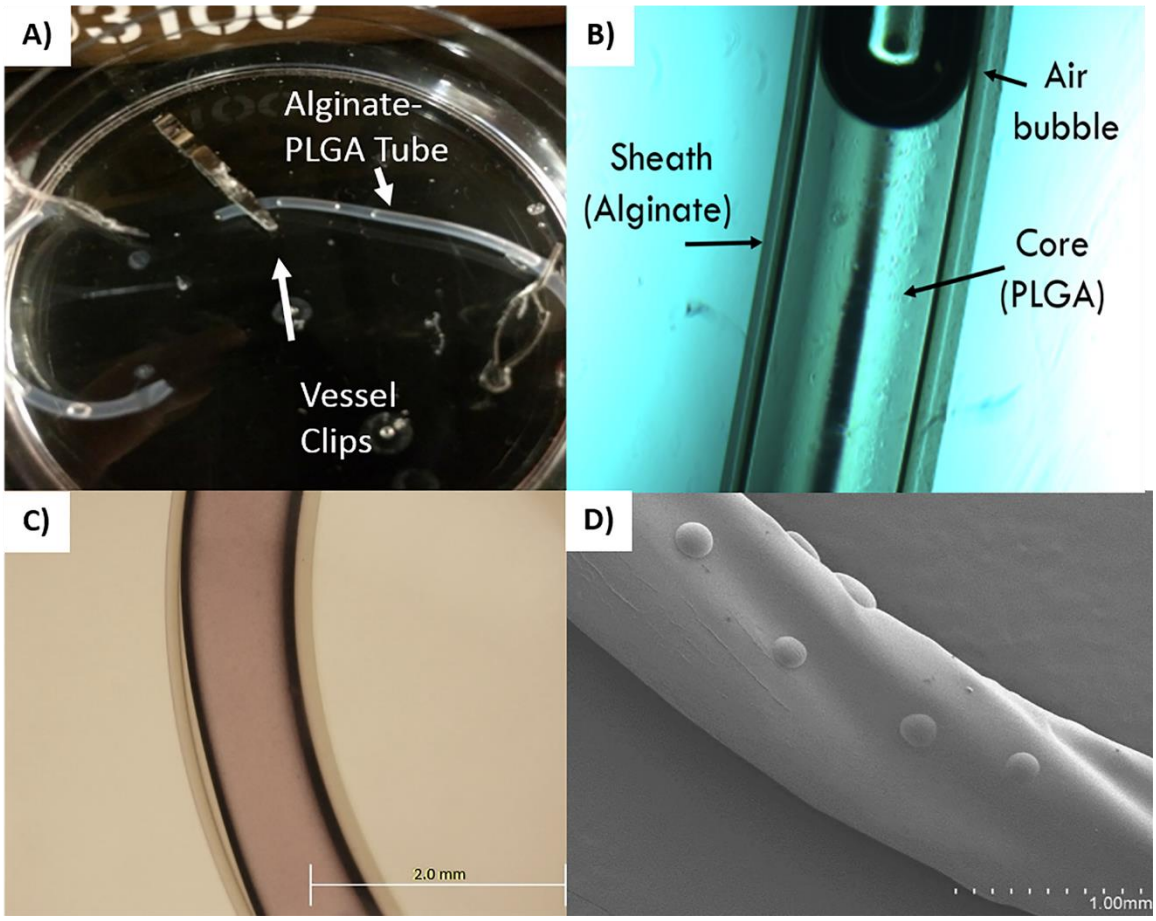

Figure 3-4 : Images of 3D printed alginate-PLGA tubes. A) A photograph of an alginate-PLGA tube. B) A light microscope image of an alginate-PLGA tube with the alginate sheath and PLGA core indicated with arrows. C) A light microscope image (clear shell showing alginate, light-purple core showing PLGA containing rhodamine) of an alginate-PLGA tube B). D) A SEM image of alginate-PLGA tube.

Release kinetics of fluorophores from alginate-PLGA tubes

Release studies were performed with alginate-PLGA tubes where fluorescein (0.025 mg/ml) was loaded into the alginate sheath whilst rhodamine B (0.8 mg/ml (R1) or 0.4 mg/ml (R2)) was loaded into the PLGA core. Sequential release was observed where fluorescein began to be released immediately (burst release) from the alginate sheath and the majority of this fluorophore was released within 24 hours

(**Figure 3-5**). In contrast, no detectable rhodamine B was released for the first 24 hours followed by a steady release over the next 3 – 4 days.

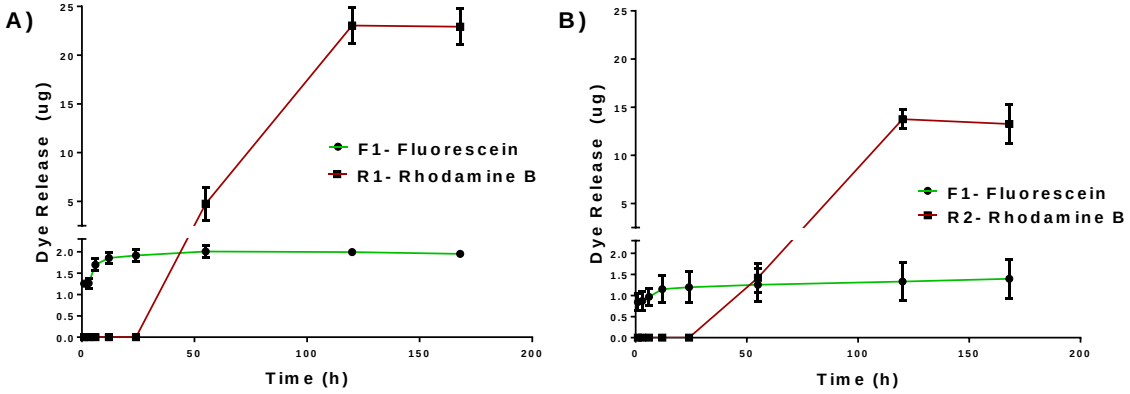

Figure 3-5 : Cumulative release from alginate-PLGA tubes. Tubes had varying fluorescent dye and material composition with A) alginate-PLGA tubes containing 0.8 mg/ml of rhodamine B in the PLGA core and 0.025 mg/ml of fluorescein in the alginate sheath (n = 3) and B) alginate-PLGA tubes containing 0.4 mg/ml of rhodamine B in the PLGA core and 0.025 mg/ml of fluorescein in the alginate sheath (n = 3).

In order to eliminate the possibility that chemical interactions between polymer and fluorophore impacted on release kinetics, the release rates of different polymer and fluorophore combinations were assessed. All combinations yielded similar release kinetics demonstrating a burst release for each fluorophore/polymer matrix combination (**Figure 3-6**). Of particular importance here, was the observation that rhodamine B was released from the PLGA polymer much faster (**Figure 3-6B**) than was observed for the alginate-PLGA tube (**Figure 3-5**) highlighting the influence of the alginate sheath in slowing release of this fluorophore.

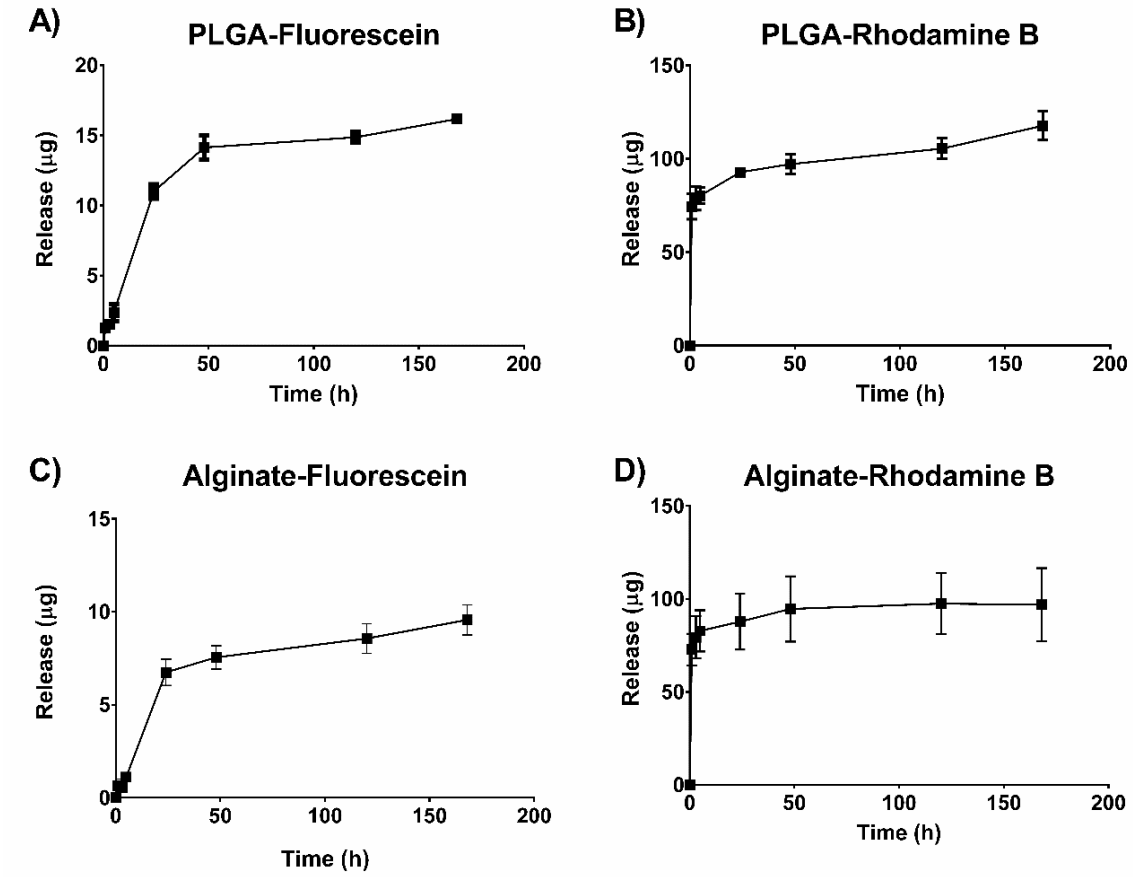

Figure 3-6 : Cumulative release of individual composition of fluorophore and polymer. Cumulative release of fluorophores from: A) PLGA loaded with fluorescein (0.025 mg/ml), B) PLGA loaded with rhodamine B (0.8 mg/ml), C) alginate loaded with fluorescein (0.025 mg/ml), and D) alginate loaded with rhodamine B (0.8 mg/ml) (*n* = 4 for A, B and C).

Cytotoxicity of alginate-PLGA tube

In order to evaluate the effect of alginate-PLGA tubes on cell viability, HEK293 cells or BMSCs were cultured for 24 h in the presence of alginate-PLGA tubes of different lengths (ranging from 1 to 5 mm). After 24 h the alginate-PLGA tubes were removed and MTS reagent was added, as described in the methods section, to assess the viability of each of the differently treated cultures. As shown in **Figure 3-7** the alginate-PLGA tubes were found to have no detectable detrimental effect on viability of HEK293 cells or BMSCs.

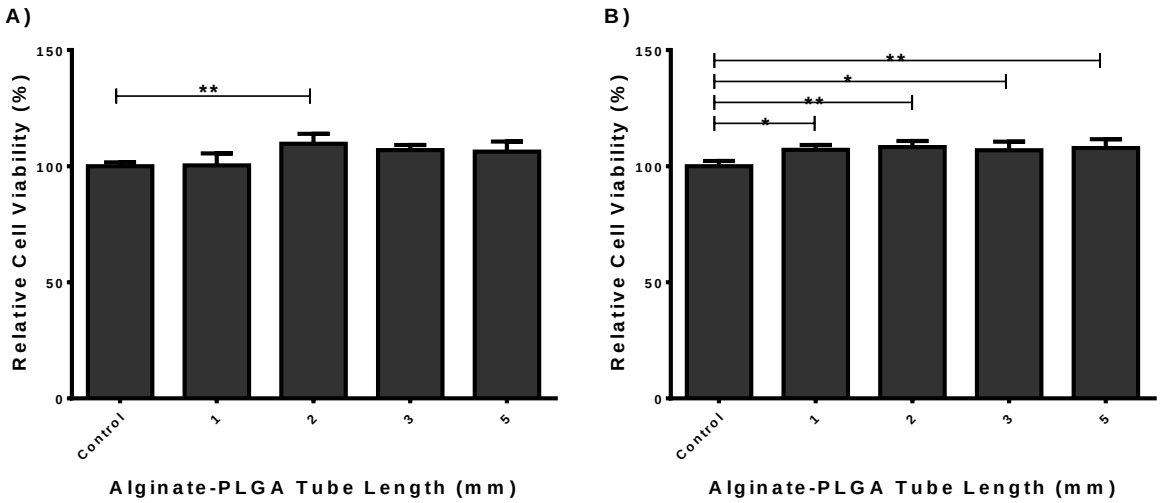

Figure 3-7 : Cell viability assays: A) HEK293 or B) BMSCs were incubated with alginate- PLGA tubes of indicated varying lengths. Statistical analysis was performed using one-way ANOVA with Dunnett's multiple comparison test at n = 4 (* signifies $p < 0.05$, ** $p < 0.01$).

Compression moduli of alginate-PLGA tubes

The compression moduli were determined using dynamic mechanical analysis as described in the methods section. Comparisons of the compression moduli data obtained for empty alginate tubes versus alginate-PLGA tubes (with or without fluorophore) were made and the results are shown in **Figure 3-8**. It was found that alginate-PLGA (without fluorophore) had a four-fold higher compression modulus compared to empty alginate tubes. The loading of fluorophore into PLGA resulted in a concentration dependent reduction in the compression modulus.

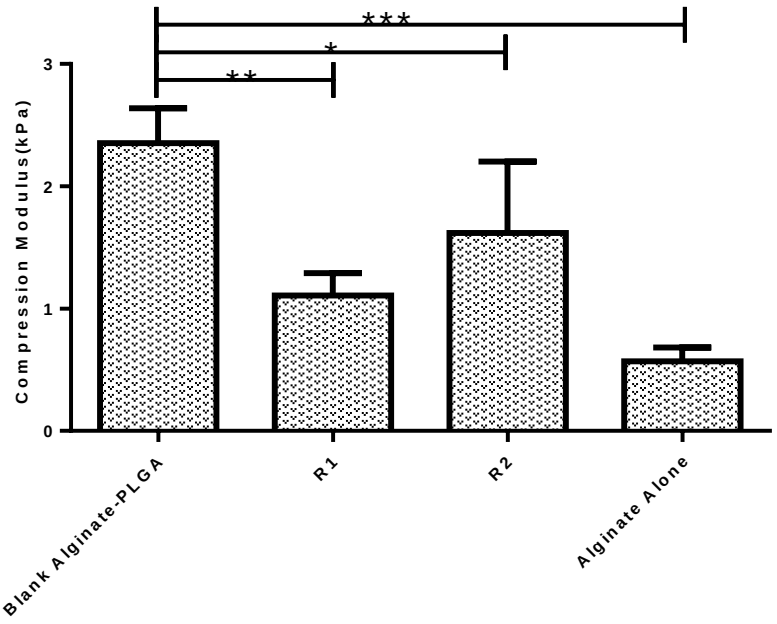

Figure 3-8 : Compression moduli of coaxial extrusion printed tubes. The moduli of blank alginate-PLGA tubes, alginate-PLGA tubes loaded with 0.025 mg/ml fluorescein (in alginate) and 0.80 mg/ml (R1) or 0.40 mg/ml (R2) rhodamine B (in PLGA), and alginate tubes alone were measured through a dynamic mechanical analyzer. Statistical analysis was carried out using one-way ANOVA with Dunnett's multiple comparison test at n=4 (* signifies $p<0.05$, ** $p<0.01$, and *** $p<0.001$).

DISCUSSION

The alginate-PLGA tubes manufactured in these studies comprised a 3D printed alginate (4% w/v) sheath and an injected PLGA core. The rationale for using 4% alginate solution was based on previous studies showing that 3 - 4% (w/v) alginate solutions were optimal for generating structurally intact tubular structures.[222, 235] The properties of the two-layered system used here were investigated, in vitro, for sequential drug delivery, biocompatibility and mechanical strength. The fluorophore release study performed with alginate-PLGA tubes loaded with fluorescein (in the alginate sheath) and rhodamine B (in the PLGA core)

demonstrated the ability of the device to release two distinct molecules in a discrete and sequential fashion. The initial release of fluorescein followed by the delayed release of rhodamine B is consistent with the nature of the layered system, where the fluorescein diffusion through the alginate sheath occurred before the release of rhodamine B from the PLGA core. We showed that rhodamine B in combination with PLGA is released very quickly into solution when it is not incorporated into the core of the alginate tube (**Figure 3-6B**) thus demonstrating the ability of the alginate-PLGA tube to achieve sequential fluorophore release.

To demonstrate the potential biocompatibility of alginate-PLGA tubes, cytotoxicity assays were performed with HEK293 and BMSC cells, and no detrimental effects on cell viability for either cell type were observed. HEK293 cells were tested because they are routinely used in drug and gene delivery studies. Bone marrow stromal cells were tested due to the fact that they are widely used in tissue engineering, specifically for bone regeneration.[236-237] Mechanical testing revealed that insertion of a PLGA core enhanced the mechanical strength of the alginate tubes by up to 4-fold. The presence of rhodamine B in the PLGA core reduced the contribution of the PLGA core to the mechanical strength of the alginate-PLGA tube and we speculate that loading of any agent may have the same effect. This effect is possibly due to the dye (or some prospective drug) reducing the overall density of the PLGA polymer core.[238-239] Thus, if that is the case, the core formulation will require minor adjustments to improve its strength if such drug-loaded alginate-PLGA tubes are to be used in applications where compression moduli of > 2 MPa are required. Conversely, it should be noted that the potential interaction between drug and polymer could cause an increase in overall density and mechanical strength.

Situations where a compression modulus of > 2 MPa would be important include the development and design of scaffolds for tissue engineering, where the scaffolds/implants are required to tolerate compression forces caused by cellular processes in order to maintain their structural integrity.[240]

CONCLUSION

The main purpose of this study was to design and test a proof of concept 3D printed controlled drug or molecule delivery system capable of sequential release. This was accomplished through the fabrication of a delivery device, comprising a 3D-printed outer alginate layer (or sheath) and an inner PLGA core, that was capable of differential release of fluorescent dyes. The sequential release observed was due to the delayed release of dye from the PLGA core with the surrounding alginate layer facilitating its retention, whilst the dye in the alginate layer was released more rapidly. It was also established that alginate-PLGA tubes were non-toxic in vitro for two cell types tested, suggesting their potential biocompatibility in a range of in vivo applications. The mechanical strength of alginate-PLGA tubes were greatly increased with the addition of PLGA. Further optimization is ongoing to further improve design features and mechanical strength of the alginate-PLGA tubes. This includes switching from manual to automated injection of PLGA solution, as well as manipulating layer thickness to optimize release profiles and mechanical strength. These alginate-PLGA tubes have rapid and practical processability, and have the potential to provide more efficacious drug treatments. 3D printing provides a means for controlled drug delivery on the macroscale through bioprinting, but as injuries become more complex and may require smaller microscale scaffolds, other 3D printing technologies such as

two-photon polymerization should be investigated for microscale printing with controlled drug delivery abilities.

CHAPTER 4 : CONTROLLED DRUG DELIVERY FROM 3D TWO-PHOTON POLYMERIZED POLY(ETHYLENE GLYCOL) DIMETHACRYLATE DEVICES

INTRODUCTION

In order to be effective, many drugs must remain at physiologically-relevant concentrations for an extended period of time, which can be problematic with respect to patient adherence to a dosing regimen. In fact, patients with a prescription that requires multiple doses at varying times have a failure rate of approximately 50% due a myriad of issues such as health illiteracy, a complex drug regimen, or limited access to healthcare.[241] These challenges could be addressed, at least in part, through precisely controlled drug delivery systems. In other words, manipulating the release of various drugs could increase a drug's potency or deconvolute dosing regimens, while reducing cost.

Historically, controlled delivery approaches have involved formulations for targeted drug delivery,[242-245] sustained drug delivery,[245-247] or differential drug delivery[248-250] in order to enhance the temporal bioavailability of the drug or provide drugs in a specific sequence. For example, sequential drug release could be pertinent in the treatment of breast cancer; treating with ibandronate before tamoxifen is more effective than the summing effects of either drug alone, in terms of prohibiting malignant cell growth.[38] Other conditions, such as diabetes, could be treated using pulsatile drug release, where specific dosages are released at set intervals over a certain period of time based on food intake schedule. Pulsatile drug delivery systems have seen some successes in terms of treating: cardiovascular disease through different coating thicknesses using the chronomodulated drug delivery system of urapidil;[251] inflammation through ultrasound-triggered diclofenac-

loaded alginate microcapsules;[252] and colorectal cancer using enteric-coated tablets to deliver celecoxib as a prophylactic measure.[253] Furthermore, on-demand release of a drug using an internal or external trigger has been shown to be a promising strategy for treating colon cancer.[42] Various forms of controlled release have also recently found utility in several types of tissue engineering applications. For example, multilayered microspheres were fabricated using a polyelectrolyte system on the surface of poly(lactic-co-glycolic) acid constructs to deliver basic fibroblast growth factor (bFGF). This system provided the sustained delivery of biologically relevant levels of bFGF to induce higher cell proliferation compared to bFGF in solution.[254] Moreover, the ability to control when, where, and how various therapeutic molecules are released has potential applications to a variety of human diseases.

Recent advances in 3D printing, including the ability to construct complex structures with fine precision to match a designed device, open the door to rapid and facile production of controlled release devices. However, drug delivery and release kinetics have yet to be fully characterized in the context of 3D printing. Some current tissue engineering systems can immediately release various growth factors such as vascular endothelial growth factor (VEGF),[255] bone morphogenetic protein 2,[237, 256] platelet-derived growth factor,[257] and bFGF[258]. However, these successes could be greatly improved with controlled drug delivery to provide the coordinated release of growth factors in a manner that mimics biological processes like wound healing or tissue differentiation.[25] Additionally, patient-specific 3D-printed implantable devices could be used to provide slow release of anticancer drugs at the surgery site of resected tumors, thereby reducing the chances of local tumor recurrence for cancer patients while also minimizing undesirable systemic side effects.[259-261]

Several 3D-printed devices have been approved by the Food & Drug Administration (FDA), which have primarily been intended for use as prosthetics or orthopedic implants. In fact, over 100 3D-printed devices are currently on the market in the United States, the majority of which are focused on patient-matched devices that are tailored to fit a patient's missing anatomy. However, one recently FDA-approved drug tablet, Spritam, is manufactured through 3D printing and is prescribed to treat seizures.[262] Manufacturing this device via 3D printing results in dramatic improvements in drug dissolution rate in even a small amount of water, boosting the speed of treatment in these urgent scenarios. Yet, this is the only device of its kind thus far, and within the research community there is a dearth of available products that incorporate the advantages of 3D printing for precise device design with the benefits of using a controlled release strategy for drugs or biologics. Newly developed technologies such as two-photon polymerization (2PP) enable researchers to prototype micro- and nanostructures with high resolution. Compared to typical fused deposition modeling printing (50-200 μm resolution) and stereolithography (~20 μm resolution), 2PP can be used to create structures with features of the order of approximately 100 nm resolution.[263] With such high resolution and precision, 2PP enables the fabrication of complex nanoscale devices capable of directly influencing cellular growth, differentiation and behavior.[97, 264]

In this study, we investigated the effect of manipulating a number of parameters during the 3D printing process to determine if such changes could be used to control release of a model drug, rhodamine B. Using 2PP, Poly(ethylene glycol) dimethacrylate PEGDMA devices were printed with varying parameters and their drug release kinetics were assessed. PEGDMA was chosen due to its

biocompatible properties and its ability to be used as a photopolymer for 2PP printing.[265] We also tested for any cytotoxic effects of the devices on a range of potentially relevant cell lines, including those that may be pertinent to tissue engineering. We hypothesized that the 3D printing parameters of slicing, hatching, and pore size would affect drug release profiles of printed structures. The results obtained from this study provide a valuable foundation that connects 3D printing settings to controllable drug release, opening the door for this approach to be applied to implantable devices aimed at improving the treatment of a range of diseases. To the best of our knowledge, this is the first study to characterize the effects of printing parameters on (model) drug release kinetics.

Poly(ethylene glycol) dimethacrylate

Polyethylene glycol (PEG) is a synthetic polymer used in several FDA-approved applications. It is non-toxic, biocompatible, bioinert, and is often used for many biological applications as a biomaterial. PEG can be synthesized with a range of different end groups attached through anionic ring opening polymerization of ethylene oxide.[266-267] PEG also provided a strategy for overcoming many disadvantages with some biopharmaceuticals due its ability to increase drug stability and retention time (bioavailability), thereby reducing dosing frequency.[268] Through the process of PEGylation, which is the covalent conjugation of molecules with PEG, the newly formed compound is able to retain the aforementioned properties of PEG. It is also possible for PEG to form hydrogels by crosslinking the chains.[269] In our case, the crosslinking was achieved by the addition of methacrylate groups on each end of the chain, which can then undergo photo-induced crosslinking to form PEGDMA

(**Figure 4-1**) hydrogels. Using arginine-glycine-aspartate(RGD)-modified PEG hydrogels, the photoencapsulation of osteoblasts was made possible for bone tissue regeneration. The modification with RGD promoted rat calvarial osteoblasts to attach, spread, and organize on the polymer surface of the PEG hydrogel to greater extent compared to the when unmodified hydrogels were used. The enhanced adhesion allowed the encapsulated osteoblasts to form mineralized matrices in vitro. The ability to create an injectable polymer system provided an alternative *in situ* method of delivering cell-polymer constructs to bone defect sites.[270]

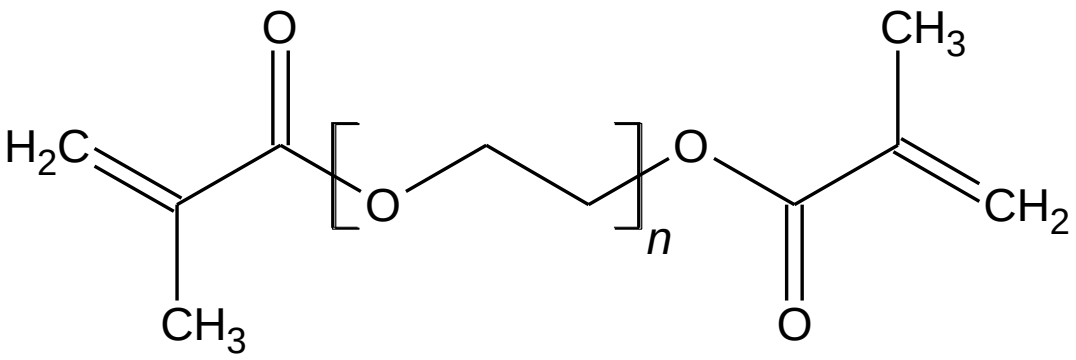

Figure 4-1 : Chemical structure of Poly(ethylene glycol) dimethacrylate.

MATERIALS AND METHODS

Device design

Stereolithographic files of printable devices were designed and generated using AutoCAD software (Autodesk, San Francisco, California). The general design consisted of either a cuboid or a "woodpile" structure, which contained multiple layers of regularly-spaced cylinders, each layer lying in the x-y plane but rotated 90° compared to the previous layer. The overall dimensions of each device was 105 x 105 x 60 μm (LxWxH), unless otherwise noted. For woodpile structures, cylinder diameter and spacing were each varied according to the parameters listed in **Table**

4-1. When 3D models are translated into a series of commands for line-by-line two-photon polymerization, the user must determine the line density. The 3D solid is first split into a series of horizontal layers in a process known as slicing. The distance between each of these layers is known as the slicing distance. Each of these layers is then split into a series of parallel lines in a process known as hatching. As with slicing, the distance between each line is known as the hatching distance. In our experiments, the slicing and hatching distances were each varied for cuboid and woodpile structures, with all other parameters held constant (Table 4-1).

Device fabrication

According to our previous work and preliminary results, the optimal formulation to create repeatable 2PP poly(ethylene glycol) structures containing sufficient fluorophore for detection was: 88.3 % wt PEGDMA (Mn of 575, viscosity of ~57 cP, Sigma-Aldrich, St. Louis, MO), 2.7 % wt Irgacure 369 (photoinitiator, BASF, Germany), and 10 % wt rhodamine B (Sigma-Aldrich) mixture (10 mg/mL in water) or water only (no fluorophore) as the control. To facilitate adhesion of the printed structure to the substrate, we functionalized glass coverslips with polymerizable groups prior to their use as two-photon polymerization substrates.[97] Briefly, we exposed glass substrates to oxygen plasma (Plasma Cleaner equipped with PlasmaFlo gas flow control, Harrick Plasma, Ithaca, NY) at an oxygen flow rate of 22.5 mL/min at 30 W radio frequency power for three minutes. The substrates were then submerged in a 1% solution of 3-(trimethoxysilyl)propyl methacrylate (Sigma-Aldrich) in hexanes (Fisher Scientific, Waltham, MA) overnight. We then rinsed the

glass substrates in hexanes, dried them and stored them in an airtight container at room temperature until ready for use.

Table 4-1 : Design parameters for two-photon polymerized PEGDMA woodpile and cuboid devices.

	Structure Type	Cylinder Diameter	Clyinder Spacing	Slicing Distance	Hatching Distance
Varying Cylinder Size	Woodpile	5 µm	5 µm	0.10 µm	0.10 µm
	Woodpile*	10 µm	10 µm	0.10 µm	0.10 µm
	Woodpile	15 µm	15 µm	0.10 µm	0.10 µm
Varying Cylinder Spacing	Woodpile	5 µm	5 µm	0.10 µm	0.10 µm
	Woodpile	5 µm	9.29 µm	0.10 µm	0.10 µm
	Woodpile	5 µm	15 µm	0.10 µm	0.10 µm
Varying Slicing Distance	Woodpile*	10 µm	10 µm	0.05 µm	0.10 µm
	Woodpile*	10 µm	10 µm	0.1 µm	0.10 µm
	Woodpile*	10 µm	10 µm	0.15 µm	0.10 µm
Varying Hatching Distance	Woodpile*	10 µm	10 µm	0.10 µm	0.05 µm
	Woodpile*	10 µm	10 µm	0.10 µm	0.10 µm
	Woodpile*	10 µm	10 µm	0.10 µm	0.15 µm
Varying Slicing Distance	Cuboid	N/A	N/A	0.05 µm	0.10 µm
	Cuboid	N/A	N/A	0.10 µm	0.10 µm
	Cuboid	N/A	N/A	0.15 µm	0.10 µm
Varying Hatching Distance	Cuboid	N/A	N/A	0.10 µm	0.05 µm
	Cuboid	N/A	N/A	0.10 µm	0.10 µm
	Cuboid	N/A	N/A	0.10 µm	0.15 mm

*These devices were each 110 x 110 x 60 µm

For each set of devices, the substrate was placed in the sample holder and a droplet of the formulation was placed in the center of the substrate which was a 30

mm ½" glass coverslip (CS-30R, Warner Instrument, Hamden, CT). The structures were created using a Nanoscribe Photonic Professional GT two-photon lithography system (780 nm laser, Nanoscribe GmbH) using a 25X objective (NA=0.8). Laser power (100%), scanning speed (50,000 um/s) and all other lithography parameters were held constant for all experiments. After fabrication, the structures were removed from the sample holder, submerged in deionized water for five minutes and dried at room temperature overnight in the dark.

Device morphology

The morphology of the printed devices was examined using scanning electron microscopy (SEM). Samples were mounted on an aluminum stub using double-sided carbon tape. These samples were then dried overnight in ambient air for 24 h prior to being coated with gold-palladium using an argon beam K550 sputter coater (Emitech Ltd., Kent, England). Once coated, samples were imaged using a Hitachi S-4800 SEM (Hitachi High-Technologies, Tokyo, Japan) at an accelerating voltage of 1 kV with the sample stage tilted at 30°.

Release of rhodamine B

Samples were initially imaged with an EVOS FL fluorescence microscope (Thermo Fisher, Waltham, MA) and used as the starting reference point for fluorophore release (starting concentration of 100%: **Figure 4-2**). Samples were imaged at the lowest brightness settings: 10% intensity at an exposure rate of 15 ms. Devices were then submerged in 3 mL of nanopure water and incubated in a shaking incubator set at 300 rpm and 37°C. Samples were collected at the following time

points: 1, 3, 6, 12, 24, 48, 72, 96, 168 h. At each designated time point, the water was aspirated and the devices were left to dry for 5 minutes prior to imaging. Images of the devices were collected using a fluorescence microscope at the settings previously mentioned, then analyzed using ImageJ as described previously (see example in **Figure 4-2B-C**).[271-272]

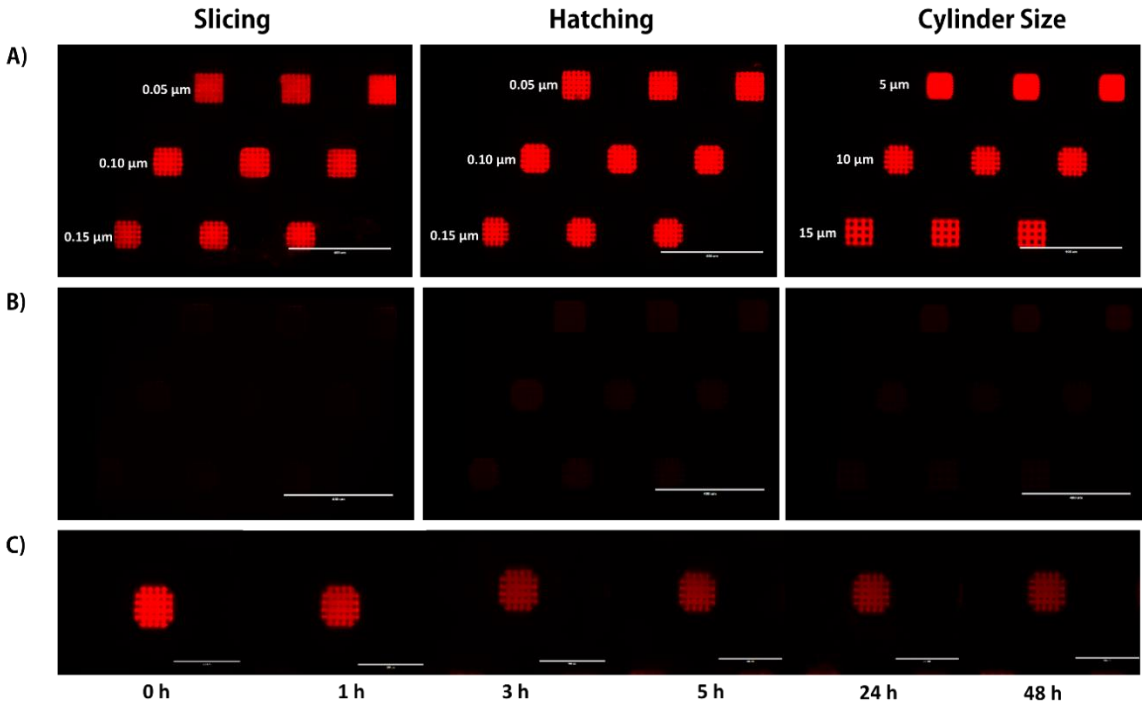

Figure 4-2 : Method of detecting release from 2PP PEDMA scaffolds. A) Image of scaffolds taken from the EVOS microscope depicting slicing, hatching, and cylinder size with their respective change in distance and cylinder sizes from 2PP at 10% intensity and 15 ms using an EVOS RFP light cube. B) Control samples of PEGDMA without rhodamine B at 10% intensity and 15 ms, (no fluorescence detected). C) An example of the loss of fluorescence of a single scaffold over time (0-48 h). Full sets of scaffolds have a scale bar of 400 µm (A, B), while single scaffolds have a scale bar of 200 µm (C).

In order to generate this standard curve, PEGDMA discs (4 mm x 50 µm) were fabricated using UV polymerization. Briefly, laminate molds were constructed using two standard glass slides with two layers of heavy duty aluminum foil (approximately

0.5 in. x 1 in.; total thickness ~50 μm) on each end as spacers. These layers were clamped on each end using binder clips and each mold was filled with 60 mL of PEGDMA with rhodamine. The pre-polymerized formulations were the same as described above and to each other except for the amount of rhodamine B added, which ranged from 0 mg/mL to 2 mg/mL. Each sample was photopolymerized by exposing the mold to high intensity UV light (Omnicure Series 2000 equipped with 8 mm liquid light guide, Excelitas Technologies, Waltham, MA) at a distance of 2 inches from the end of the light guide and an intensity of 6 W/cm^2 (measured at the source) for 50 seconds. After polymerization, each mold was carefully deconstructed, and the resulting films were rinsed by rapid submersion in excess deionized water three times to remove trace amounts of unreacted prepolymer. The films were then blotted with a laboratory napkin and a 4 mm biopsy punch was used to create uniform discs ($n > 5$) from the periphery of the film, where photobleaching had not occurred. After imaging as described above, our results confirmed that the amount of added rhodamine B was within the linear range of the standard curve and therefore the structures were not saturated with the fluorophore (**Figure 4-3**).

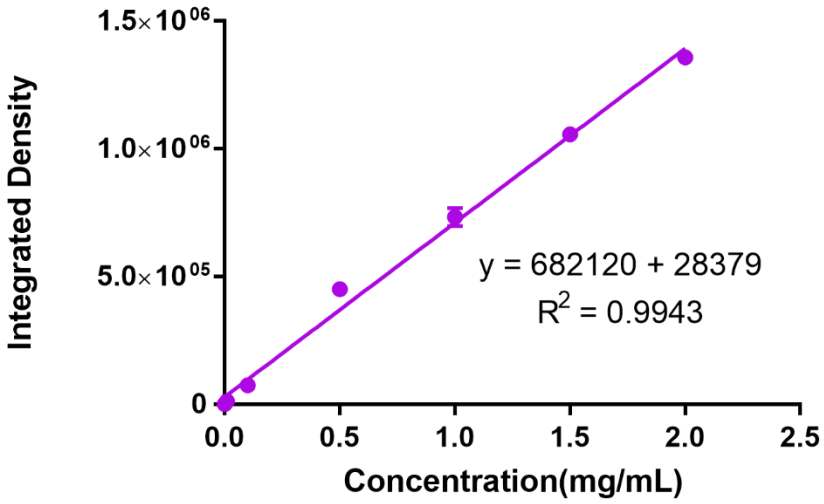

Figure 4-3 : Standard curve of rhodamine B concentrations loaded on PEGDMA printed 5mm discs. A standard curve was constructed from printed PEGDMA discs containing different concentrations of rhodamine B (n=3).

PEGDMA biocompatibilty

Human embryonic kidney 293 cells (HEK293, ATCC, Rockville, MD) and bone marrow stromal stem cells (BMSCs, ATCC) were maintained in Dulbecco's modified Eagle's medium (DMEM) (Gibco®, Life Technologies Corporations, Brooklyn NY) supplemented with 10% fetal bovine serum (Atlanta Biologicals, Lawrenceville, GA), 10 mM HEPES (Gibco®), 50 µg/mL gentamycin sulfate (Cellgro, Manassas, VA), 1 mM sodium pyruvate (Gibco®), and 1 mM Glutamax (Gibco®). Both cell types were incubated at 37°C and 5% CO_2 in a humidified atmosphere. Murine induced pluripotent stem cells (MiPSCs) were generated previously.[273-274] Pluripotency media comprised Dulbecco's modified Eagle's medium: Nutrient Mixture F-12 (DMEM/F12; Life Technologies, Gibco, Carlsbad, CA) with 15% fetal bovine serum (Life Technologies), 1% 100X nonessential amino acids (NEAA; Life Technologies), 0.4 mM L-glutamine (Life Technologies), 0.1 mg/mL Primocin (InvivoGen, San Diego, CA), and 8.88 ng/mL 2-mercaptoethanol (Sigma-Aldrich). Just before use, 2 U/mL of mouse

recombinant leukemia inhibitory factor (mLif, ESGRO; EMD Millipore, Billerica, MA) was added and media were warmed to 37 °C.

To test for cytotoxicity of the PEGDMA-based devices, 5 mL of complete media was added to 60 mm petri dishes that contained the PEGDMA devices and were incubated overnight at 37 ˚C. The supernatant was then harvested and used as growth media to feed each cell line. The "conditioned" media was incubated with the cells for 24 hours before cytotoxicity was analyzed. Cytotoxicity was assessed using an MTS assay (CellTiter 96®, Promega, Madison, WI) following manufacturer's instructions. In brief, cells were plated in a 96-well plate at a density of 1 x 10^4 cells/well in 100 µl of DMEM (+ supplements) for 24 h prior to treatments. The media was then aspirated and then the indicated supernatants (described above) were added at varying dilutions. The cultures were then incubated for 24 h, after which the media was removed, cells were washed with 1X PBS, and then replenished with fresh media. Then, 20 µL of MTS reagent was added and cells were incubated for a further 3 hours. Finally, the absorbance was measured at 490 nm using a SpectraMax plus 384 Microplate spectrophotometer (Molecular Devices, Sunnyvale, CA). Relative cell viability was analyzed using untreated cells as the control group.

Statistical analysis

The loss of fluorescence was use as a means of quantifying drug release (**Figure 4-2**) and release curves were analyzed using non-linear regression with a one-phase exponential decay function. Extra sum-of-squares F-tests were used to test the null hypothesis that all release profiles within a given group could be modeled using the same parameters. P-value was two-sided and the value of less than 0.05 was

considered to be statistically significant. Data were presented as mean ± the standard error of the mean, unless stated otherwise. All statistical analyses were done based on a 95% confidence interval.

RESULTS AND DISCUSSION

In order to identify the potential connection between 3D printing settings and controlled drug release, we investigated the effects of varying printing parameters on controlled fluorophore release. Using a Professional GT two-photon polymerization system, 3D printed devices were printed with varying slicing, hatching, spacing, and shape and were homogenously loaded with rhodamine B in order to assess controlled drug delivery functionality. Furthermore, the printed devices were analyzed for cytotoxic effects on a variety of cells in an effort to demonstrate the potentially wide applicability of this technology to multiple disease models.

Cylinder diameter

In this experiment, rhodamine B was homogenously encapsulated in the material (PEGDMA) and thus can be assumed to be distributed equally across the entire volume. Meanwhile, diffusion is known to be dependent on the surface area available for transport. Hence, a higher surface area per volume should equate to more rapid transport. For an individual cylinder, this relationship becomes:

$$\frac{SA}{V} = \frac{2\pi rh + 2\pi r^2}{\pi r^2 h} = \frac{2(h+r)}{rh} \quad (1)$$

Where r is the cylinder diameter and h is cylinder length. Thus, for a constant cylinder length, decreasing the diameter increases the surface area to volume ratio.

Accordingly, we hypothesized that the rate of rhodamine B released from PEGDMA "woodpile" structures would increase as the diameter of cylinders decreased.

The PEGDMA structures created to test this first hypothesis matched the overall intended woodpile design (**Figure 4-4A-F**). It should be noted, however, that PEGDMA structures are known to be hydrophilic and in this case, water accounts for roughly 10% of the mass. The majority, if not all, of this hydration can be presumed to have been lost upon dessication, which was required for SEM imaging. This drying effect likely contributed to slight deviations (e.g. shrinkage) in the appearance of the structures from their morphology prior to dessication (**Figure 4-4D-F**). Furthermore, the exact resolution of 2PP of this particular formulation has not yet been characterized thoroughly, and it is possible that inexact printing in the form of over-polymerization also contributed to minor structural deviations from the model. In the case of the woodpile structure with 5 μm cylinders, this phenomenon resulted in occlusion of the intended spaces between cylinders.

It is reasonable to anticipate that such pore obstruction in the 5 μm woodpile structure would inhibit release from the structure. Indeed, the initial rate of release of rhodamine B from the 5 μm woodpile structures was lower than that from the 10 or 15 μm structures (**Figure 4-4G**). Furthermore, the ultimate amount of rhodamine B released from the 5 μm structures (41%) was lower than the amount released from the 10 or 15 μm structures (51% and 53%, respectively; **Figure 4-4G**). In fact, the nonlinear regression parameters for the 5 μm release profile was significantly different from those of the 10 and 15 μm parameters ($p < 0.001$), which were not significantly different from each other. Overall, these data do not support the hypothesis that decreasing cylinder diameter increases release rate from woodpile

structures. On the contrary, structures composed of the smallest cylinders released the model drug more slowly than structures with larger cylinders. This difference in release can likely be attributed to the occlusion of water due to the small pore size of the structures containing 5 μm cylinders. Potentially indicating that there are pore size limitations for water infiltration. Furthermore, differences in pore size (spaces between cylinders) in this experiment could have confounded the effect of cylinder size. With a larger pore size, more water would be more readily able to enter the device and thus increase the rate of fluorophore diffusion and release. Since cylinder diameter and spacing were directly linked in this experiment, the expected effect of increasing the cylinder diameter (decreasing the release rate) because of the decrease in surface area to volume ratio could have been offset by the concomitant expected effect of increasing the spacing between cylinders (increasing release rate).

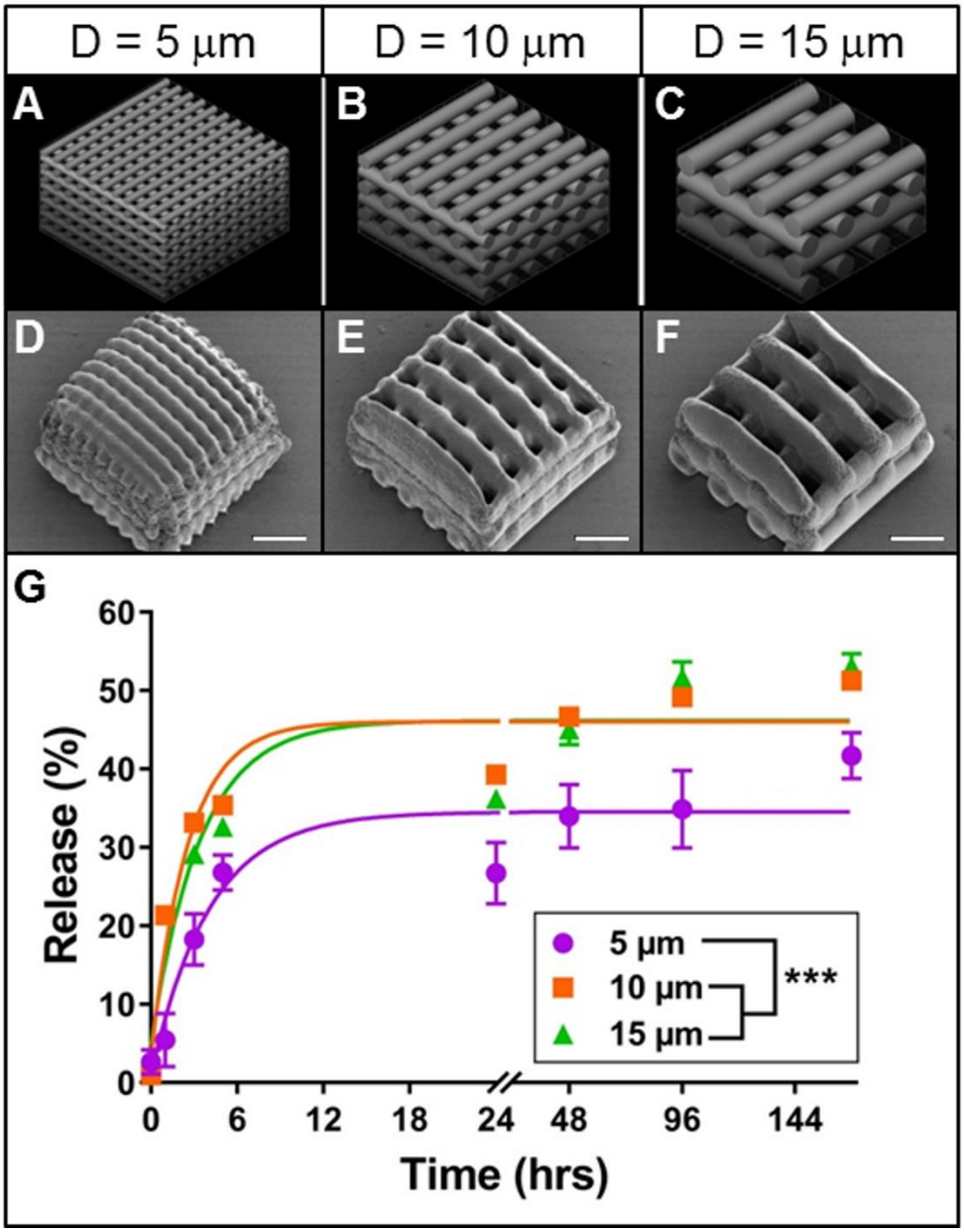

Figure 4-4 : Effect of cylinder size on rhodamine release from 2PP woodpile structures. A-C: 3D models of woodpile structures with designed cylinder diameters and cylinder spacing of 5, 10 or 15 µm, respectively. D-F: Representative scanning electron micrographs of the corresponding poly(ethylene glycol) woodpile structures. Scale bars represent 25 µm. G: Release profiles (data points) and best-fit non-linear regression curves (lines) of rhodamine B diffusion from the devices shown in A-F. Error bars represent standard error of the mean; significance denoted is based on comparison of non-linear regression parameters, ***$p < 0.001$ (n=6).

Cylinder spacing

In order to gain more clarity into the effects of woodpile morphology on rhodamine B release rate, the effects of cylinder diameter and cylinder spacing were separated. In theory, increasing the space between cylinders in a woodpile structure will increase the accessible surface area for release per unit weight of the structure, boosting the driving force for diffusion of rhodamine B out of the cylinders. In essence, smaller pores may occlude water infiltration while larger pores allow for higher rates of diffusion. Thus, we hypothesized that for PEGDMA woodpile structures with constant cylinder diameters, increasing the spacing between cylinders would increase the release rate of encapsulated rhodamine B.

As in the initial experiment described above, the PEGDMA woodpile structures resembled their respective 3D models reasonably well (**Figure 4-5A-D**), considering the effects of overpolymerization and dessication. While a structure with 15 μm spaces between cylinders was initially included in this experiment, these structures could not be reliably fabricated and were often absent from the sample surface, most likely because the large spacing prevented adequate intra-structural adherence of the cylinders to one another. Thus, this group was excluded from further analysis. Regardless, the initial rate of release of rhodamine B from the structures with larger spacing between cylinders (9.29 μm) was higher than that from the structures with smaller spacing (5 μm; **Figure 4-4E**). Meanwhile, the amount of rhodamine B that had been released at the end of the experiment was relatively similar between the structures with larger spacing (44%) compared to smaller spacing (42%; **Figure 4-4E**). Furthermore, the nonlinear regression parameters for these two release profiles were also significantly different from one another ($p < 0.001$). These data support the

hypothesis that increasing spacing between cylinders in a PEGDMA woodpile device increases the release rate of encapsulated rhodamine B. Also, as was observed here, the planned porosity should be considered carefully, as pores that are too large can cause structural integrity issues of the printed device.[275]

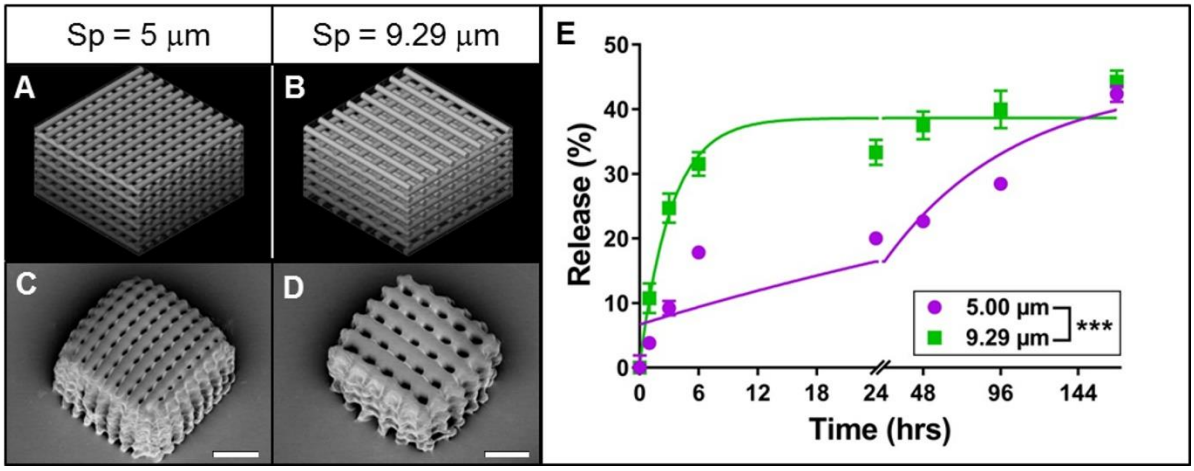

Figure 4-5 : Effect of cylinder spacing on rhodamine B release from 2PP woodpile structures. A-B: 3D models of woodpile structures with designed space between cylinders of 5 or 9.29 µm, respectively, with constant cylinder diameter of 5 µm. C-D: Representative scanning electron micrographs of the corresponding PEGDMA woodpile structures. Scale bars represent 25 µm. E: Release profiles (data points) and best-fit non-linear regression curves (lines) of rhodamine B diffusion from the devices shown in A-D. Error bars represent standard error of the mean; significance denoted is based on comparison of non-linear regression parameters, ***$p < 0.001$ (n=6).

Slicing and hatching distance

Our previous work has demonstrated that, for any given material chemistry, the structural outcomes of 2PP devices are highly dependent on selected 2PP parameters, such as slicing and hatching distance.[97] Knowing the impact of these subtle adjustments on final morphology, it was speculated that slicing and hatching distance may also play a role in the diffusion kinetics of encapsulated molecules from 2PP devices. Slicing and hatching distance are each inversely correlated to line

density within a structure. Thus, increasing either parameter should result in structures of decreasing density. In theory, this change would in turn enhance the mobility of encapsulated molecules and speed their diffusion out of the structure. Thus, we hypothesized that increasing slicing or hatching distance of PEGDMA structures would increase the rate and ultimate amount of rhodamine B released from the device. This expectation is congruent not only with our second hypothesis (supported by **Figure 4-5**), but also with findings that suggest increased release rate of small molecules from highly porous mesoporous matrices,[276] lidocaine from highly porous poly(lactic-co-glycolic) microparticles,[277] and vancomycin from calcium phosphate cement matrices.[278]

In order to separate the effects of slicing and hatching from those of cylinder size and spacing, as previously described, we first tested the slicing and hatching hypothesis using a simple cuboid structure. In all cases, the PEGDMA cuboids were qualitatively similar to the originally designed model (**Figure 4-6A-B**) and to one another, with the effects of drying and over-polymerization being less pronounced than they were for the woodpile structures. Increasing slicing increased the initial rate of rhodamine B release from the cuboids (**Figure 4-6C**). Furthermore, the total amounts of rhodamine B released at the end of the experiment were 42, 44 and 50% for slicing distances of 0.05, 0.1 and 0.15 μm, respectively. In particular, significant differences were observed between the non-linear regression parameters of the release profiles of cuboids with slicing distances of 0.05 and 0.15 μm ($p < 0.01$). Increasing the hatching distance had a similar effect on rhodamine B release from PEGDMA cuboids (**Figure 4-6D**). In this case, each set of release profile non-linear regression parameters were significantly different from one another ($p < 0.001$).

These data support the hypothesis that increasing slicing or hatching distance would boost release from 2PP PEGDMA structures. Additionally, the release of rhodamine B from these cuboids was markedly slower than release from analogous woodpile structures. This difference can likely be attributed to the lower surface area and limited porosity of the cuboids compared to the woodpiles, which likely led to less water infiltration and thus decreased the rate of rhodamine B diffusion from the devices.

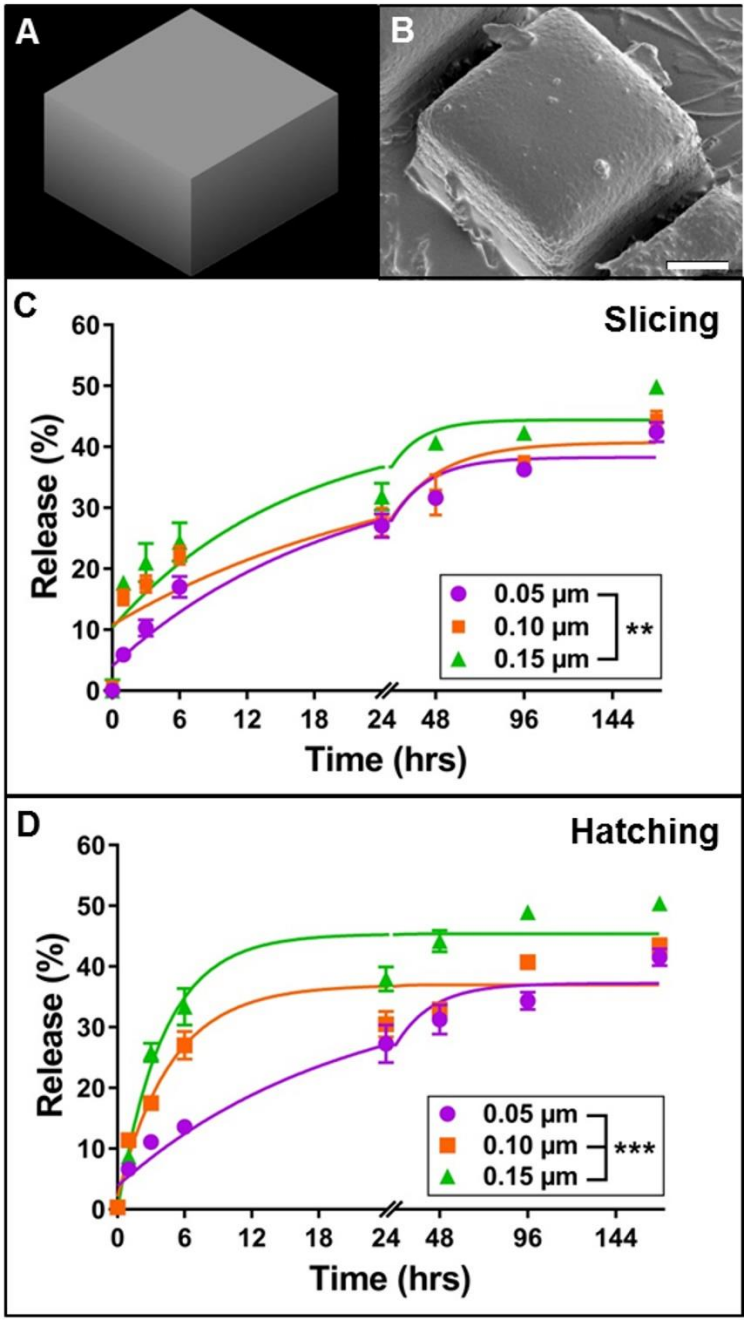

Figure 4-6 : Effect of slicing and hatching distance on rhodamine B release from 2PP cuboid structures. A: 3D model of cuboid structure. B: Representative scanning electron micrograph of the corresponding poly(ethylene glycol) cuboid structure. Scale bar represents 25 µm. C-D: Release profiles (data points) and best-fit non-linear regression curves (lines) of rhodamine B diffusion from cuboid devices with varying slicing or hatching distance, respectively. Error bars represent standard error of the mean; significance denoted is based on comparison of non-linear regression parameters, $^{**}p < 0.01$ and $^{***}p < 0.001$ (n=3).

The effects of varying slicing and hatching distances were then investigated with woodpile structures described previously. While in all cases the resulting PEGDMA woodpiles (**Figure 4-7A-F**) resembled the model (which is shown in **Figure 4-4B**), small slicing or hatching distances resulted in deterioration of the structure at the edges of the device (**Figure 4-7A, D**). Despite this structural difference, the profiles of rhodamine B release from these PEGDMA devices were remarkably similar to one another. The total amount of rhodamine B released from structures with slicing or hatching distances of 0.05 μm (49 or 52%, respectively) was slightly lower than that from 0.1 and 0.15 μm slicing or hatching (56 and 59, or 58 and 58%, respectively; **Figure 4-7G-H**). However, no significant differences between the non-linear regression parameters for these release profiles were detected, suggesting that at this scale, the kinetics of rhodamine B release from PEGDMA woodpile structures were independent of slicing or hatching distance.

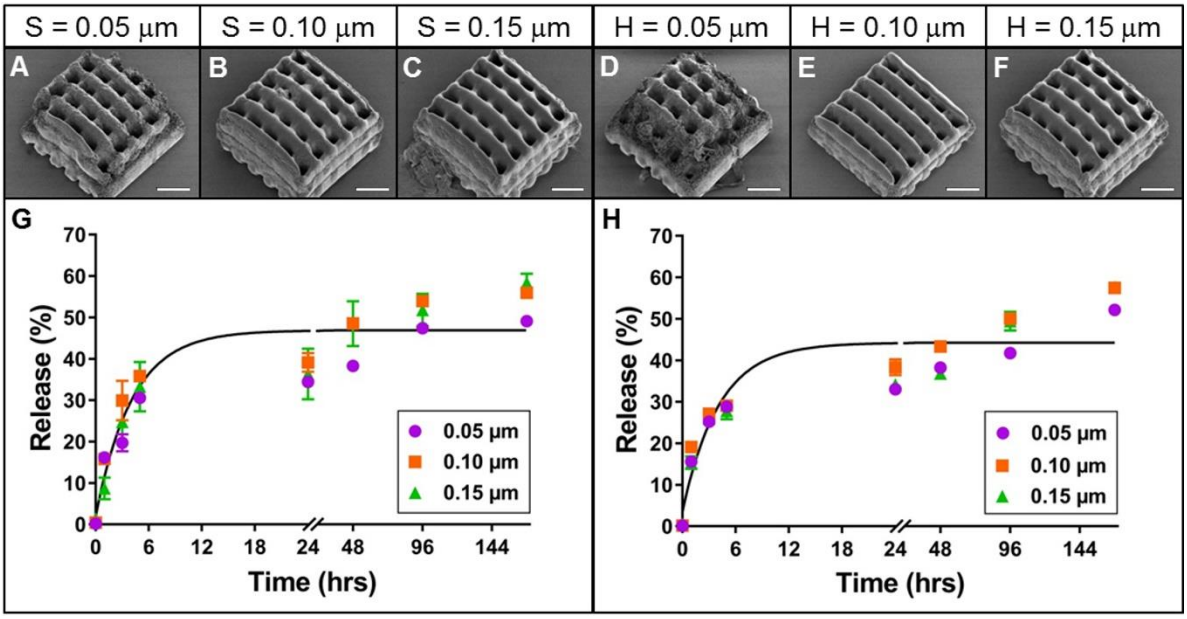

Figure 4-7 : Effect of slicing and hatching distance on rhodamine B release from 2PP woodpile structures. A-F: Representative scanning electron micrographs of PEGDMA woodpile structures with 10 µm cylinders created using a slicing distance of 0.05, 0.1 or 0.15 µm at constant hatching distance or a hatching distance of 0.05, 0.1 or 0.15 µm at a constant slicing distance, respectively. Scale bars represent 25 µm. G-H: Release profiles (data points) and best-fit non-linear regression curves (lines) of rhodamine B diffusion from the devices shown in A-F with varying slicing (G) or hatching (H) distances. Error bars represent standard error of the mean; no significant differences between non-linear regression parameters were detected (n=3).

At the end-points of the release studies (one week) presented in **Figures 4-5 - 4-7**, the devices did not completely release their payloads, yet the diffusion profiles seemed to have reached equilibrium. There are a number of possible explanations as to why this may have occurred. First, small amounts of rhodamine B may still have continued to be released past the final time point, but the incremental change in fluorescence was not great enough to be detected. Second, since rhodamine B is photoactive, a proportion of it may have acted as a second photoinitiator during two-photon polymerization, thus becoming part of the crosslinked polymer via covalent

bonding.[279] However, given the relatively high concentration of rhodamine B included in the formulation and the presence of the primary photoinitiator, which is more sensitive and efficient, we presume that rhodamine B activation during fabrication occurred to only a minor degree. Furthermore, even though this event may prevent the full release of the rhodamine B from the devices, it is a variable that is expected to be consistent between all groups. Finally, the saturation effect could also be due in part to the photodegradation properties of rhodamine B. Since the photodegradation of rhodamine B is relatively low (about 10% loss over 168 h),[248] we believe that this contribution was also minimal.

PEGDMA biocompatibility

In order to be clinically translatable, the devices described here must not only be effective in delivering the intended therapeutic, but also show evidence of being biocompatible. With photopolymerization in particular, the presence of free radicals is at least one concern in terms of cytotoxicity.[280] We validated the safety of these prototype 2PP devices using a range of cell types, including cells that may be used for tissue engineering purposes, such as iPSCs and BMSCs. The released PEGDMA material had no significant cytotoxic effect when incubated with these various cell types (**Figure 4-8**). These results build upon what others have also noted; crosslinked PEGMA has been shown to have no cytotoxic effects on other cell lines such as NIH-3T3 fibroblasts.[265] The lack of cytotoxic effects of the printed PEGDMA material towards stem cells is particularly important when considering these PEGDMA-based devices for tissue engineering purposes, as it demonstrates their versatility for a wide range of applications and tissue types.

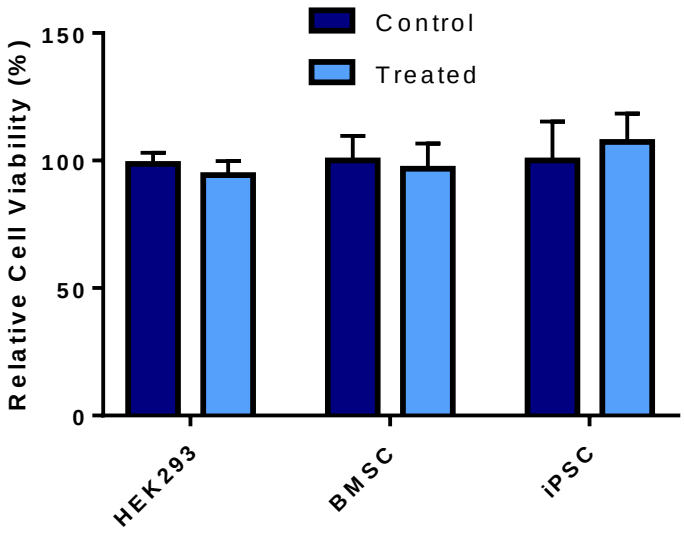

Figure 4-8 : Biocompatibility of photopolymerized poly(ethylene glycol). The viability of human embryonic kidney cells (HEK293), bone marrow stromal stem cells (BMSC) or mouse induced pluripotent stem cells (iPSC) was analyzed through an MTS assay after 24h of incubation in "conditioned" media. The cells were incubated with "conditioned" media that was made by incubating photopolymerized poly(ethylene glycol) dimethacrylate samples in cell culture media for 24 h . Error bars represent standard deviation (n=4).

CONCLUSION

3D printing technologies provide a means for the production of novel therapeutic systems by creating matrices for cellular attachment, proliferation, and differentiation with the ability to release drugs that promote improved therapeutic responses. In this study, we demonstrated that the manipulation of 3D printing parameters is within the purview of controlled drug delivery. Specifically, device design, porosity, and material density all play a role in the kinetics of small molecule release from two-photon polymerized structures. Since these can be tuned independently of material chemistry, this method of control has potential cost and time saving benefits over traditional controlled release methods. Furthermore, this

approach paves the way for facile manipulation of release rates in various locations within the device to provide improved controlled drug delivery in cases where sequential or spatially-specific release is desired. This method would be cost effective compared to a multi-material system because it would reduce the print time and the amount of material needed to fabricate the desired device. Furthermore, these multifaceted systems should be further explored in future studies to determine their feasibility as tissue engineering scaffolds, especially in cases where sustained release of signaling molecules is desired for a specific and high-resolution 3D printed microenvironment. Additional future studies aimed at utilizing other drug candidates such as proteins and lipophilic drugs would further demonstrate the versatility of this approach. Overall, our results speak to the promise of 3D printing in controlled drug delivery and suggest the possibility of precisely and easily tailoring implants and other devices to fit the specifics of many biomedical applications or the personalized therapeutic needs of individual patients.

CHAPTER 5 : TWO-PHOTON POLYMERIZATION OF TOPOLOGICAL CUES FOR HUMAN iPSC DIFFERENTIATION

INTRODUCTION

The process of regenerating functional tissues *in vitro* depends on the synergistic interactions between the biomimetic constructs (e.g. scaffolds), cells, and biologically active molecules.[281] Thus, one of the core aspects of tissue engineering is the design of biomimetic scaffolds with the ability to modulate the cellular attachment, proliferation, and differentiation. These scaffolds can be created in an effort to mimic the extracellular matrix (ECM), which provides chemical and physical cues that can influence the function and fate of cells, including stem cells.[282-283]

In their physiological microenvironment, stem cells differentiation, aside from being stochastically driven, is guided by a diverse cocktail of signals provided by the stem cell specialized microenvironment or "niche" and often involving the ECM.[282, 284-285] These signals can come chemical and biological cues from growth factors, from molecules released from the ECM or can be the result of physical ECM properties such as rigidity, porosity, and topography where cells differentiate in response to surface patterns, among other cues, ranging from 10 nm to 10 μm.[286-289] Thus, the most complex and physiologically accurate scaffolds would theoretically not only contain growth factors or provide a generic ECM-like medium for promoting attachment, but also elicit a specific cell fate when encountered by stem cells or other cell types of interest. Surface topographical cues for cellular differentiation can include such properties as roughness, anisotropic patterns (grooves, aligned fibers), and isotropic patterns (pillars, pits, tubes/columns, fibers).[283] Many attempts at studying topographical effects on differentiation have involved groove stuctures,[286,

[290] symmetry and disorder,[291] spacing,[292] and roughness.[293] However, there is a paucity of research investigating the effects of microscale/nanoscale shape and shape size on cellular differentiation. This is possibly due to the limited availability of tools for templating as well as being a time consuming endeavor.[294] Due to its prevalence in tissue engineering and its ability to be used to create repeatable microscale structures, 3D printing technology is a feasible means of addressing this knowledge gap.

Two-photon polymerization (2PP) can be used to pattern and print variously shaped and sized microstructures with nanometer precision (50 nm),[295] enabling one to study the effects of these topographies on cellular differentiation. Two-PP technology offers high-resolution outputs compared to similar light-induced 3D printing (e.g. traditional stereolithography) by requiring two photons to arrive at the initiator molecule within 1 femtosecond of each other. This requirement restricts the polymerization reaction to the focal point of the light source, where the two photons meet and provide adequate energy to stimulate photopolymerization.[97] Two-PP is a promising and emerging technique in tissue engineering. For example, it was recently used to fabricate prototype photoreceptor scaffolds, which were incubated with human induced pluripotent stem cell (iPSC)-derived retinal progenitor cells as a potential means to create patient-specific cell therapies for retinal degeneration. Seeded cells were able to settle and extend neuronal processes parallel to the vertical pore of the scaffolds to produce autologous retinal cell grafts. These grafts have the potential to be used for the restoration of vision for those suffering retinal degenerative diseases.[97] In another study, 2PP technology was applied to bone tissue engineering, where researchers were able to print exact replicas of trabecular

bone from μCT scans. These scaffolds, when incubated with a human osteosarcoma-derived cell line, Saos-2, were shown to provide a biomimetic 3D structure to foster cellular behavior that led to enhanced osteogenic differentiation of Saos-2 cells *in vitro*.[296] These results demonstrate the significant potential of 2PP to provide patient-matched scaffolds. Advances in stem cell research have enabled the effective integration of stem cells into tissue engineering based systems, leading to progress in developing functional tissue and generating patient-matched *in vitro* models for potential screening and investigational research on pathophysiology or transplantation. In particular, pluripotent stem cells have garnered interest due to their ability to self-renew indefinitely or differentiate into any cell type in the body.[286, 297-298] The use of iPSCs has garnered a great deal of interest due to their ability to be derived from adult somatic cells (fibroblasts)[299] thus circumventing the ethical issue of isolating them from pre-implantation stage embryos.[300-301] Also, iPSCs provide an opportunity to create patient-specific cell therapies, thus bypass the problematic issue of immune rejection due to a lack of histocompatibility.[298, 302] Using iPSCs derived from adult mouse fibroblasts, Diekman *et al*. were able to generate chondrogenic cells through the addition of bone morphogenic protein 4 and dexamethasone. The differentiated cells were applied to an *in vitro* cartilage defect model and were shown to be effective at promoting the interaction of nascent tissue with surrounding adult cartilage.[303] In a separate study, neural crest stem cells (NCSCs) derived from human iPSCs were shown to preferentially differentiate into Schwann cells *in vitro*. The preferential differentiation in Schwann cells also occurred *in vivo* where the cells became integrated into the myelin sheath and resultantly enhanced myelination and regeneration of peripheral nerves subsequent to being

seeded on nanofibrous tubular scaffolds (nerve conduits) that were used to bridge transected sciatic nerves in an athymic rat model.[304] Thus iPSCs provide a valuable resource for tissue engineering by helping to generate viable tissues and organs, and when derived from the patient's own cells, free from immune rejection.

Both iPSCs and 2PP technologies significantly contribute to an ever growing and versatile tissue engineering-based toolset aimed at generating functional tissue. In this study, we leveraged this combination to understand the effects of topographical cues, namely shape and size, on stem cell differentiation. Two-PP IP-L-780 arrays were fabricated with varying shapes (circles, triangles, squares, or stars) and varying shape sizes (1, 2, or 5 μm diameter or equivalent) to determine how down-stream gene expression was affected by these parameters. The goal of this study was to provide insight into the effects of 3D printed 2D microscale platforms of shape and size topographies on stem cell differentiation. The use of 2PP enabled rapid fabrication of defined topographies at the single micron scale. Since these cues were generated using 2PP, they can be incorporated into future scaffold designs by directly mapping to the structure surface, enabling cellular differentiation to a desired cell type. Furthermore, topographies that encourage differentiation to a specific lineage could be used in combination with traditional differentiation protocols (which typically rely on chemical cues), more efficiently and affordably.

MATERIALS AND METHODS

Topography design

Four geometric shapes were selected for study: circles, triangles, squares, and five-pointed stars. To determine the effect of shape alone, size was held constant using the shape width needed to yield equivalent shape areas (**Table 5-1**), as calculated using the following geometric relationships:

$$A_{circle} = \left(\pi/4\right)W^2$$

$$A_{triangle} = \left(1/4\right)(\sin 30°)W^2$$

$$A_{square} = W^2$$

$$A_{star} = \left(5/4\right)\left[\frac{1}{(1+\sin 18°)^2}\right]\left[\frac{1}{\tan 18°}+\frac{1}{\tan 36°}\right]W^2$$

Where W is the absolute width of the given shape. To study the effect of size, we selected one shape (star) and varied its width by a factor of 2 or 5 (for widths of 3.18 or 7.96 μm, respectively). For each distinct shape and size, a series of commands was written in the Nanoscribe command software (DeScribe) such that the shapes, when printed, would occur in a square array with overall dimensions approximating an octagon with a width of 6 mm. Regardless of shape or size, the center of each feature of the array was spaced 10 μm from the center of its nearest neighbor. For imaging purposes, the overall size of the array was decreased to a width of 200 μm.

Table 5-1 : Specifications for the varying shapes at constant size.

Shape	Width, W (μm)	Area (μm^2)
Circle	1	0.79
Triangle	1.25	0.79
Square	0.89	0.79
Star	1.59	0.79

Two-photon polymerization

A Photonic Professional GT System (Nanoscribe GmbH, Germany) was used to create the high resolution topographical features described above. Glass coverslips (30 mm d.; #1.5; CS-30R, Warner Instrument, Hamden, CT) were used as fabrication substrates. For each array, a coverslip was secured to the sample holder and a drop of oil (Immersol 518 F, Carl Zeiss; Inc Oberkochen, Germany) was applied to the bottom in the center. A droplet of photoresist (IP-L-780, Nanoscribe) was placed on the top, in the center of the coverslip, and the sample holder was inserted into the instrument. Each array was printed at 100% laser power and a scanning speed of 50 mm/s using regular 3D direct-laser-writing and a 25X objective (NA = 0.8). Once printing was complete, the substrate was removed from the sample holder, then submerged in 25 mL propylene glycol monomethyl ether acetate (Sigma-Aldrich, St. Louis, MO) for 15 minutes, followed two five-minute submersions in 25 mL isopropyl alcohol (Sigma-Aldrich). Each sample was then air-dried overnight and stored in the dark at room temperature until use.

Topography characterization

The morphology of the printed devices was examined using scanning electron microscopy (SEM). Samples were adhered to a segment of a standard glass slide and mounted on an aluminum stub using double-sided carbon tape. These samples were then dried overnight in ambient air for 24 h prior to being coated with gold-palladium using an argon beam K550 sputter coater (Emitech Ltd., Kent, England) at 35 mA for 1.5 minutes. Once coated, samples were imaged using a Hitachi S-4800 SEM (Hitachi High-Technologies, Tokyo, Japan) at an accelerating voltage of 1 kV. Atomic force micrographs (AFM) were collected using a Bruker BioResolve with Peak Force Tapping (Bruker, location) equipped with a ScanAsyst in Air probe (Bruker) using a peak force amplitude of 350 nm and peak force frequency of 2 kHz.

Topography preparation

Each sample was transferred to a 6 well plate and sterilized in 70% ethanol for 15 minutes, followed by three washes with 1X PBS. Samples were then incubated with 1.5 mL of poly-d-lysine hydrobromide solution (0.1 mg/mL in sterile water) at 4°C overnight to allow for recombinant human laminin 521 (Gibco) binding. After overnight incubation, the poly-d-lysine solution was aspirated, and the samples were washed with sterile water. Meanwhile, 6 mm glass cloning cylinders (Sigma-Aldrich) were sterilized by submersion in 70% ethanol overnight followed by three washes with 1X PBS. These were then air-dried in a sterile environment for approximately 15 minutes prior to their use. Vacuum grease was sterilized by exposure to UV light (3 W/cm^2 for 90 seconds, Omnicure Series 2000 equipped with 8 mm liquid light guide, Excelitas Technologies, Waltham, MA), then applied to one end of the cloning

cylinder, without greasing the interior of the cylinder, and then placed directly over the printed structures. The cylinders were then gently pressed down to ensure adhesion to the glass coverslip or the 6-well plate (in the case of the control with no coverslip). Then 50 µL of recombinant human laminin 521 solution (50 µg/mL in HBSS +/+) were added to each cylinder and the samples were incubated overnight.

Cell culture and seeding

Prior to being seeded onto the laminin-coated 2PP substrates, human iPSCs (episomally derived, Gibco, Brooklyn, NY) were cultured on laminin-coated 6-well tissue culture plates with Essential 8 (E8) Flex Medium containing 10 ng/mL human recombinant fibroblast growth factor (FGF, Gibco) and 1 mg/mL Primocin (InvivoGen, San Diego, CA).

At the time of seeding, cells were washed twice with 1X PBS and incubated with 1 mL EDTA (0.48 mM) in PBS (Versene, Gibco) at room temperature for 6 minutes or until cell colonies began to break up and cells became rounded (cells were viewed under the microscope in real-time during this process to prevent over-incubation, which can lead to cell death). The Versene was aspirated and then 2 mL of differentiation media [10% heat-inactivated FBS (Gibco) and 1 mg/mL of Primocin in DMEM medium (Gibco)] were added immediately and used to gently wash cells from the plate surface. Generally, one well of confluent human iPSCs in a 6-well plate can be passaged to yield 6 other wells (1:6). With this ratio in mind, we adjusted the amount of cells to seed based on the area scaling of one well of a 6-well plate and our cloning cylinder. For one well in a 6-well plate, the amount of cell suspension to passage at 1:6 would be 0.33 mL cell suspension. The area of a single well in a 6-

well plate is about 9.6 cm^2, while the area of the cloning cylinder is 0.3 cm^2. From these areas we calculated the dilution amount needed to ensure seeding densities were consistent. For example, for 18 cylinders, the total area would be 5.4 cm^2, which is about half of one well in a 6-well plate. Thus, approximately 0.17 mL cell suspension would be needed for all 18 cylinders. Seeding at a volume of 50 µL per cylinder, the total volume needed would be 900 µL, consisting of 170 µL of cell suspension and 730 µL of differentiation media. After removing the excess laminin solution, cells were seeded into each cloning cylinder at a total of volume of 50 µL. Cells were incubated at 37 °C and 5% CO_2 and media was replaced daily for 7 days.

Sample Calculation:

1. Passage ratio 1 to 6

$$2\frac{mL\ cell\ suspension}{well}\ x\ 1\ well = \frac{2}{6}\frac{mL\ cell\ suspension}{wells} = 0.33\frac{mL}{well}$$

2. $6\ Well : Area = 10\ cm^2$

$\text{Cloning}\frac{\text{Cylinder}}{96}\text{well plate: Area} = 0.3\ \text{cm}^2$

$$For\ 18\ cylinders:\ \ 18\ cylinders\ x\ 0.3\frac{cm^2}{cylinder} = 5.4\ cm^2\frac{1}{2}of\ a\ 6\ well$$

3. $\frac{1}{2}\ well\ x\ 0.33\frac{mL}{well} = 0.17\ mL\ cell\ suspension$

$50\ \frac{\mu L}{cylinder}\ x\ 18\ cylinders = 900\ \mu L$ total volume needed

$$170\ \mu L\ of\ cell\ suspension + \mathbf{730\ \mu L\ of\ media} = \mathbf{900\ \mu L\ total}$$

Material cytotoxicity

To verify the biocompatibility of IP-L-780, thin (50 µm) discs of this material were created using UV polymerization and were used to create conditioned differentiation media. Briefly, one droplet of IP-L-780 was added to the surface of a 30 mm glass coverslip covered with a thin coating of Rain-X ®, which was applied as directed by the manufacturer. A second coated coverslip was gently placed on top with the coated side facing toward the droplet, causing the liquid to disperse evenly between the two surfaces. This construct was exposed to high-intensity UV light at an intensity of 1.5 W/cm2 for 15 seconds (Omnicure, at a distance of 2 inches from the end of the light guide intensity measured at the source). The coverslips were then delaminated, the thin film was removed, and discs were created using a 4 mm biopsy punch. The resulting samples were immersed in 70% ethanol, rinsed three times in 1X PBS, and incubated in differentiation media at 37 °C and 5% CO_2 overnight to create conditioned media. Cells were seeded in a tissue culture treated 96-well plate as described above at a volume of 100 µL per well. Discs were incubated in media for 1-7 days without cells to create conditioned media. Cells were then fed with the conditioned media 24 h. After 24 h of incubation, cells were tested for cell viability. Cell viability was measured using an MTS assay (CellTiter 96®, Promega, Madison, WI) following removal of conditioned media and replacement with fresh media. To this fresh media, 20 µL of MTS reagent were added and after three hours, the absorbance of each well was measured at 490 nm using a SpectraMax plus 384 Microplate spectrophotometer (Molecular Devices, Sunnyvale, CA). The relative cell viability was analyzed and compared to untreated cells as the control group.

Gene expression

RNA was extracted from iPSCs after 7 days of incubation in various topographies using a NucleoSpin RNA XS RNA isolation kit (Macherey-Nagel, Mountain View, CA). All steps were consistent with the manufacturer's protocol except for collection of cell lysate. Instead, the media from each sample was first aspirated and then 51 µL of the Buffer RA1 + TCEP was added to each cylinder to enable lysis. Instead of vortexing vigorously, the solution for each sample was pipetted up and down 5-10 times to reduce the potential of cylinders detaching from glass cover slip. This suspension was then collected and added to a 0.5 mL microcentrifuge tube. This step was repeated twice in order to obtain a total of 102 µL solution used in the "lyse and homogenize cells" step. After completion of the remaining protocol, the resulting RNA was stored at -20°C.

Complementary DNA (cDNA) was made with the SuperScript VILO cDNA Synthesis Kit (Invitrogen). Briefly, 4 µL of 5X VILO Reaction Mix and 2 µL of SuperScript Enzyme Mix were added to each PCR reaction tube. Template RNA (5-8 µL) was then added, and finally ultrapure water (RNase, DNase Free, Gibco) was added to a final working volume of 20 µL. Samples were then capped, mixed gently and centrifuged. These tubes were then incubated for 10 minutes at 25°C followed by 120 min at 42°C. This reaction was terminated by incubation at 85°C for 5 minutes and then held at 4°C overnight.

The TaqMan hPSC Scorecard Assay was used to determine relative gene expression of iPSCs differentiated incubated on the varying topographies. This analysis measures differentiation based upon 93 genes, which correlates to each of the three germ layers. In a 1.5 mL microcentrifuge tube (RNase free), a 1:1 solution

consisting of one part TaqMan Gene Expression Master Mix (Applied Biosystems, ThermoFisher Scientific) to one part cDNA + ultrapure water for a total of 960 µL for each sample. Then 10 µL of this solution was added to each well in a 384-well TaqMan hPSC Scorecard Plate (Applied Biosystems, 4 samples per plate, 96 wells per sample). Each plate was covered with an adhesive optical cover and centrifuged at 600 x g for 5 minutes. Quantitative PCR was performed using a QuantStudio 6 Flex Real-Time PCR System (Thermo Fisher). The run consisted of a hold at 50°C for 2 minutes, then 95°C for 10 minutes, followed by 15 seconds of melting at 95°C, and annealing/extending at 60°C for 40 cycles. The resulting data were transferred to and analyzed using the Thermo Fisher Cloud, specifically the hPSC Scorecard Analysis feature.

Cellular differentiation analysis and statistical analysis

Gene expression data was exported from the hPSC Scorecard Analysis provided by Thermo Fisher Cloud and data was filtered to exclude data that had a cycle threshold not between 38-40, which is indicative of weak reaction and would not yield viable data due the lack of accumulation of a fluorescent signal. Once the data was filtered, it was compared both to the internal standard of the software (undifferentiated human iPSCs) and to the control (glass coverslip). Normal distribution was analyzed through the D'Agostino & Pearson normality test and the values were then compared using the Wilcoxon signed-Rank test that compared the values to the undifferentiated iPSCs at a value of "1" (internal standard) or compared after normalizing the data to the control group, also designated at a value of "1." A Kruskal-Wallis test was also performed to determine if groups were statistically

different from one another. All statistical analyses were done based on a 95% confidence interval.

RESULTS AND DISCUSSION

To ensure that the material used for the 3D printed topographies did not have any detrimental effects on iPSCs when performing our differentiation studies, the cell viabilities of iPSCs were analyzed for 7 days with conditioned media correlating to the 7 days to which the cells were incubated with each topographical cue (see methods section **"Material cytotoxicity"**). A concern when using photopolymerization is the presence of free radicals and residual monomers[280], and this experiment aims to address any potential cytotoxicity that the printed material may have on the cells. Any potential byproducts released from the photoresist material showed no cytotoxic effects when incubated with iPSCs for 7 days (**Figure 5-1**). These results indicate that this material is safe to be used as a means for promoting cellular differentiation.

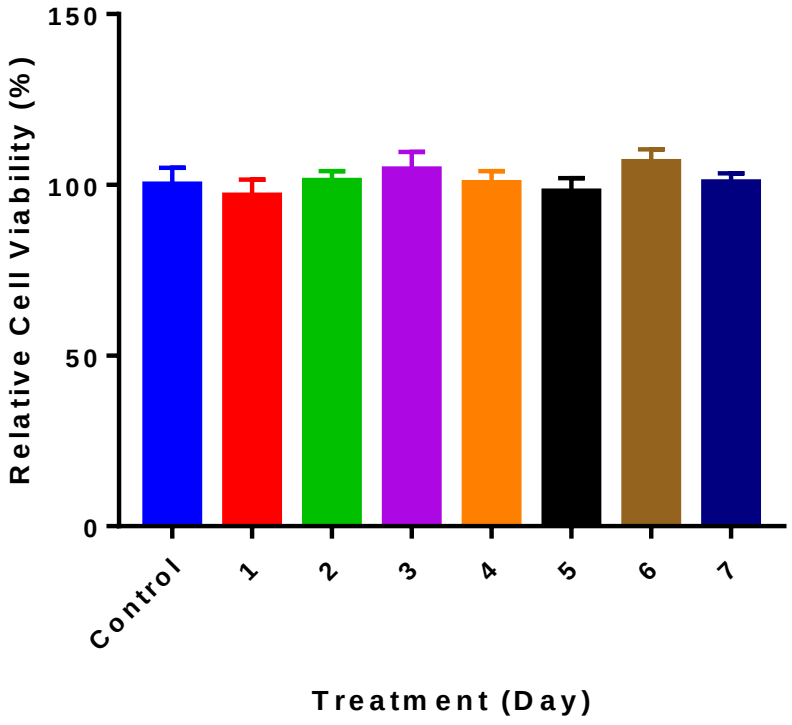

Figure 5-1 : Biocompatibility of photopolymerized photoresist. Cell viabilities of iPSCs incubated with conditioned media that was incubated for 1 through 7 days with 2PP printed photoresist in differentiation media. Error bar represents standard deviation (n= 4).

Characterization of topography using SEM and AFM

The SEM images of 2PP printed topographies show that under these conditions, 2PP can be used to print at high resolution, but that shape definition begins to fail for stars with widths less than 3 μm. The spacing of between each star shape was 10 μm center-to-center in the "x" and "y" directions. The height of the star shapes was determined through AFM and was found to be roughly 7.7, 6.7 or 5.2 μm for the 5, 2, and 1 μm size groups, respectively (**Figure 5-2**). These heights were much larger than anticipated, since photoresist exposure only occurred in one layer. Based on the anticipated star widths (7.59, 3.18 and 1.59 μm), these correspond to approximate aspect ratios (W:H) of 1:1, 1:2 and 1:3, respectively.

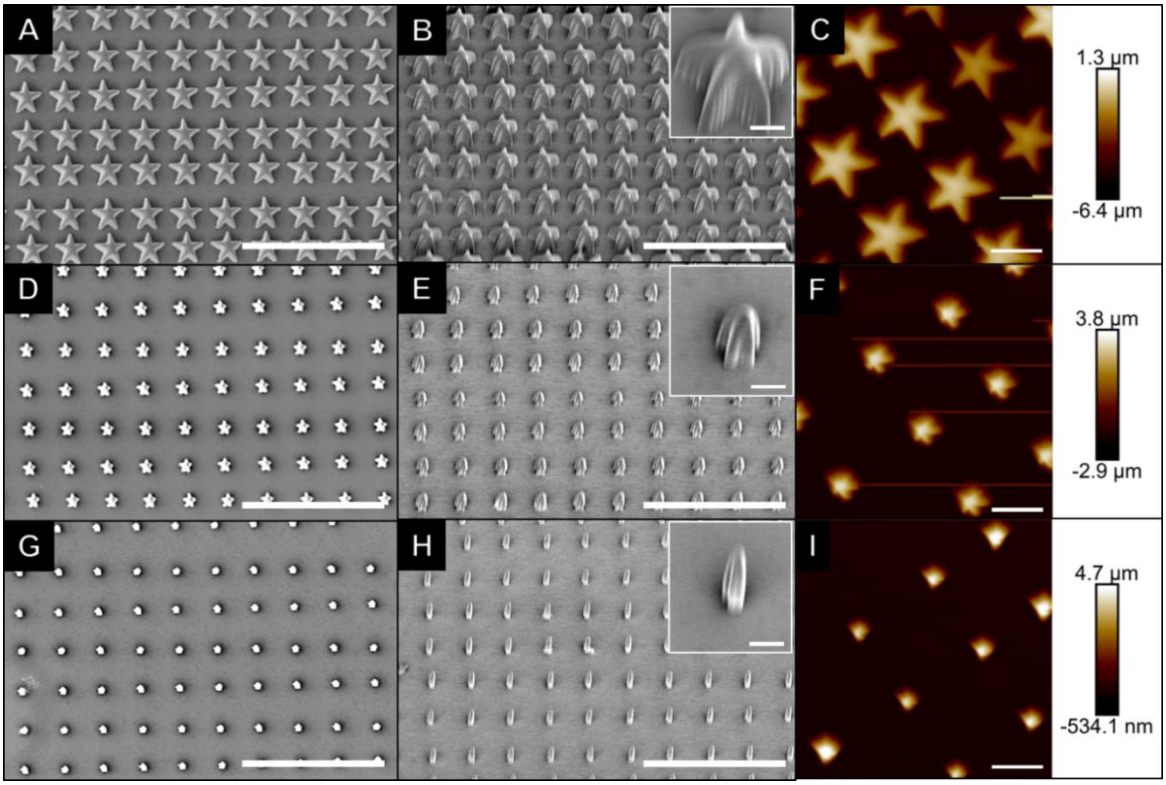

Figure 5-2 : SEM (A-B, D-E, G-H) and AFM (C, F, I) images of topographical arrays of stars with varying size. Scale bars in A-B, D-E and G-H represent 30 µm, with inset scale bars representing 2 µm. Scale bars in C, F and I represent 6 µm and the color corresponds to the sample height, as shown in the scale.

Cellular differentiation from topological cues

In order to study the effects of topological cues on cellular differentiation, human iPSCs were incubated on varying topographies for 7 days and differentiation was analyzed. Specifically, the TaqMan hPSC Scorecard was used to measure 93 different genes correlating to distinct germ layers. The ectoderm gives rise to the central nervous system, which consists of the brain and spinal cord, the peripheral nervous system, the sensory epithelia of the eye, ear and nose, skin, nails and hair, mammary glands, hypophysis, subcutaneous glands, and teeth enamel. The mesoderm is responsible for connective tissue (cartilage and bone), striated and

smooth muscle, heart walls, blood and lymph vessels and cells, kidneys, gonads, and genetical ducts, serous membrane lining the body cavities, spleen, and supernal cortices. The endoderm give rise to the epithelial lining of the gastrointestinal and respiratory tract, parenchyma of the tonsils, liver, thymus, thyroid, parathyroid, pancreas, epithelial lining of urinary bladder and urethra, epithelial lining of the tympanic cavity, tympanic antrum, and auditory tube.[305] Samples for the shape difference did not yield enough RNA for the continuation of assays meant to determine cellular differentiation. Potential factors that could have contributed to this issue include the passage number of iPSCs, where the initial shape experiments were performed with passage 2 cells, which could have contributed to instability and copy number variant deletions, thereby potentially resulting in cell growth and survival disadvantages.[306-307] Another issue may have been the number of available cells for the RNA extraction, where our initial seeding density may have been lower than the second since the process of passaging is directly related to the visual confluency of the cells. In our second experiment, where we examined effects of differently sized star shapes (1, 2, and 5 μm), the passage number was higher and thus the seeding density was higher due to the confluency compensation of the iPSCs. The 2 μm size stars did not provide quality RNA/cDNA, so this dataset was excluded from analysis.

The gene expression datasets of all samples were found to be nonparametric, mostly due to low sample size. The Wilcoxon test showed there were no significant differences between expression of self-renewal markers of the test samples and that of the pluripotent control (**Figure 5-3**). Self-renewal is the ability of cells to go through numerous cycles of cell division without differentiating. Our results show that all

groups were negative for self-renewal, which is indicative of continued viability and perhaps multipotency of the cells grown on our samples. However, the 1 μm size encouraged statistically significant differentiation towards both mesoderm ($p < 0.01$) and endoderm at ($p < 0.05$) compared to the pluripotent control while glass alone also facilitated significant upregulation of mesoderm ($p < 0.0001$) (**Figure 5-3**). The Kruskal-Wallis test did not reveal significant differences between groups. When groups were compared to the glass control, there were no statistically significant differences in the gene expression associated with any of the germ layers nor self-renewal (**Figure 5-4**). Due to the dearth of data, possibly because of the potential lower quality and amount of RNA, the statistical power of this study could be further supplemented in the future by increasing the sample size and/or initial cell seeding density. Nonetheless, the data does suggest that these 2PP topographies can upregulate ectoderm, mesoderm, and endoderm differentiation when compared to the pluripotent scorecard control. Interestingly, 1 μm stars seemed to encourage upregulation in self-renewal (*NANOG, TRIM22*), mesoderm (*COLEC10, IL6ST, SNAI2*), and ectoderm (*MAP2, NR2F2*) genes, with equal levels of regulation of endoderm compared to the relatively flat glass coverslip control. Conversely, 5 μm stars seemed to facilitate downregulation of self-renewal (*CXCL5, DNMT3B, NANOG, POU5F1, SOX2*), mesoderm (*COLEC10, IL6ST*), endoderm (*CLDN1, EOMES*), and ectoderm (*MAP2, SDC2*) genes compared to a flat glass coverslip sample. A complete list of genes expressed for each germ layer can be found in **Table 5-2** for comparison to the pluripotent scorecard control, while the gene expression compared to the glass control can be found in **Table 5-3**. The specific gene names can also be found in **Table 5-4**.

Up-regulation of genes associated with any of the germ layers could provide clues to a means to enhancing differentiation towards specific cell phenotypes desired for tissue engineering. Meanwhile, down-regulation of genes associated with the three germ layers may facilitate efficient long-term pluripotency *in vitro* or prevent differentiation towards undesirable cell types *in vitro* or *in vivo*. An example of this would be the prevention of ectopic bone formation, where scaffolds could be tailored specifically to prevent new bone growth outside of the defect area. This system could in turn deliver therapeutics such as protein BMP-2, which has been shown to elicit ectopic bone formation,[308-309] to be a more viable option for bone regeneration. As for comparison to the pluripotent control, the glass control and the 1 μm group were shown to have significant differentiation towards a mesodermal phenotype, with the 1 μm also differentiating towards an endodermal phenotype. The reason for the ability for human iPSCs to differentiate on the glass coverslip is due to the potential for random spontaneous differentiation after switching away from pluripotency media, or due to overgrown colonies contacting each other.[310-311] The star size of 1 μm causing differentiation towards the mesodermal and endodermal germ layers when compared to the pluripotent scorecard control and the upregulation of gene expression in the mesodermal and ectodermal germ layer when compared to the flat coverslip control are aligned with nanoscale topography studies of differentiation of pluripotent cells such as embryonic stem cells.[304, 312-314]

Cellular differentiation being influenced by differently sized topographies can be attributed to focal adhesion points, which are protein complexes to which the cytoskeleton of the cells connects to the ECM via cell surface integrins.[315] The smaller size constructs (1 μm) may have provided the ideal size for cellular

attachment, resulting in higher levels of cellular differentiation versus the larger 5 μm constructs, which generally caused downregulation when the samples were compared to the control glass samples. It should not be ruled out that varying the geometric shapes could have influence the level of focal adhesion anchoring, where the star shape could have contributed to better anchorage of cells to the shape topography to provide greater focal adhesion anchoring, thus helping to mediate mechanical and biochemical signaling to allow cells to differentiate towards a specific germ layer.[283, 316] Another parameter that could contribute to cellular differentiation could be the aspect ratio[317], since it has been shown that an increase in the aspect ratio can cause increased osteogenesis when geometric cues (rectangles) were used to differentiate mesenchymal stem cells.[318] In order to assess these effects, topological cues utilizing varying shapes and elevations may need to be repeated to normalize the effects of shapes and aspect ratios on differentiation. Overall, the topography of stars with a size of 1 μm provided the best platform for cellular differentiation, with the ability to induce human iPSCs differentiate towards the mesoderm and endoderm germ layers.

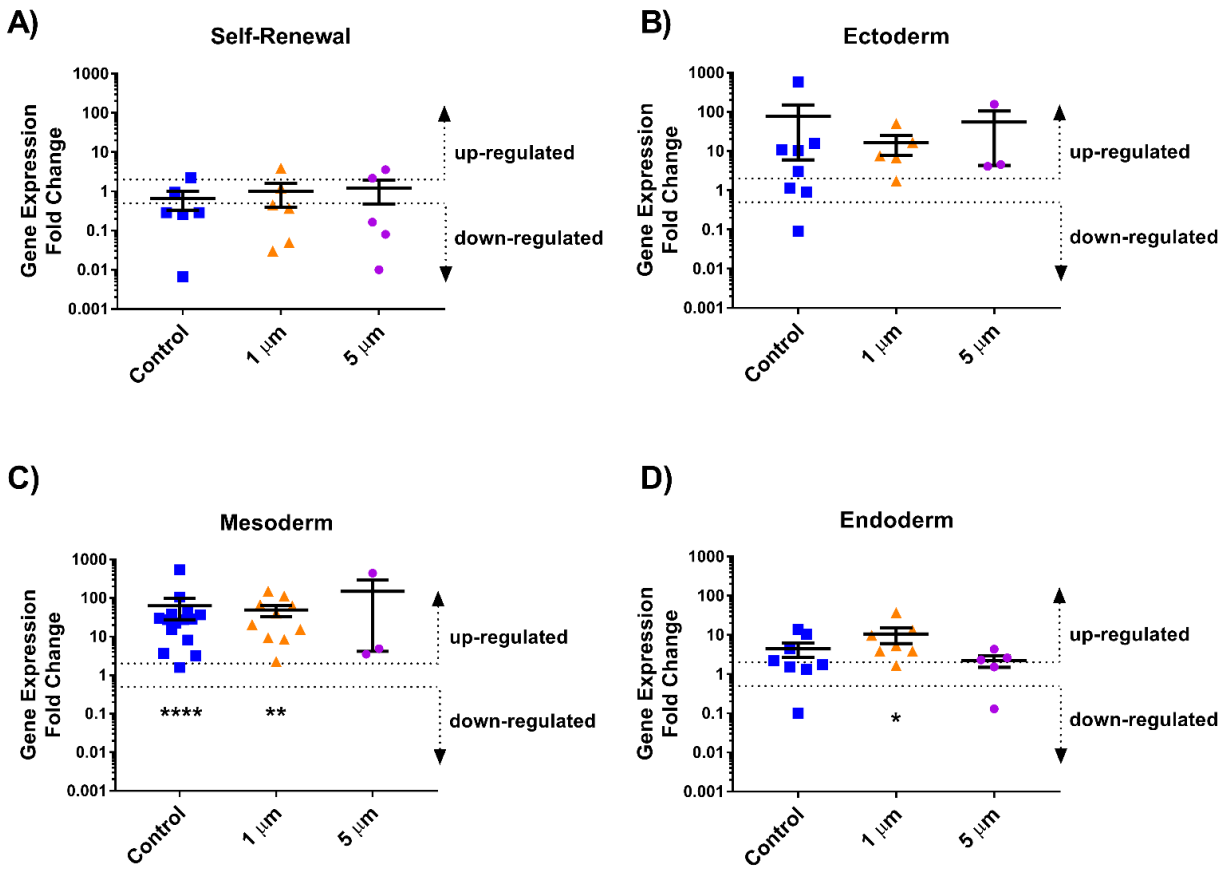

Figure 5-3 : Germ layer gene expression of cells grown on topographies consisting of different sized stars. Human iPSCs were incubated with varying size topographies and analyzed using a TaqMan hPSC Scorecard to determine germ layer gene expression. A) Self-renewal, B) Ectoderm, C) Mesoderm, and D) Endoderm differentiation were analyzed and samples were compared to the internal standard of the pluripotent scorecard control which was normalized to a value of 1. Groups of genes expressed above a 2-fold change were considered to be upregulated while expression below a 0.5-fold change was considered as down regulation of the group of genes. Samples were graphed based upon gene expression filtration (method Cellular differentiation analysis and statistical analysis). Wilcoxon Signed Rank test showed statistical significance in the mesoderm and endoderm gene groups. * $p < 0.05$, ** $p < 0.01$, ****$p < 0.0001$. Error bars represent standard deviation.

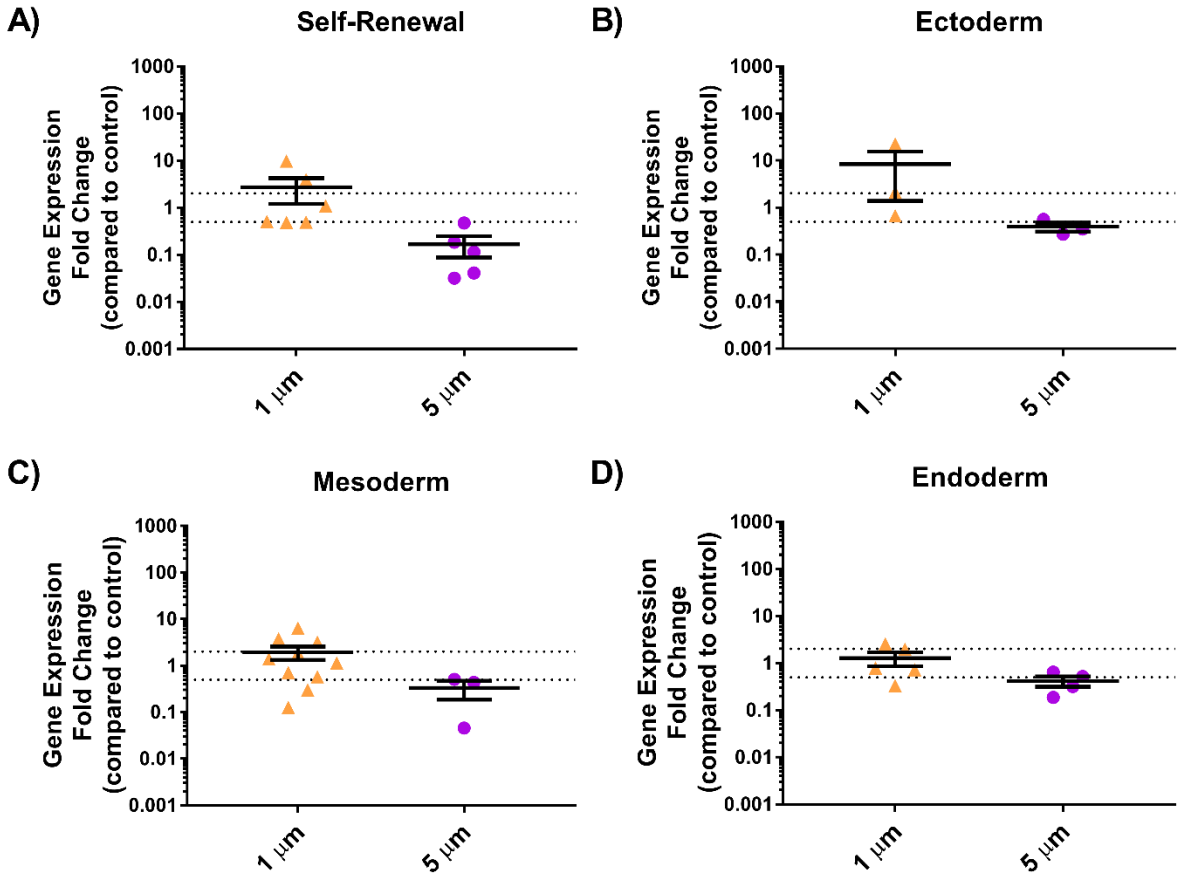

Figure 5-4 : Germ layer gene expression of cells grown on topographies with different sized stars. Human iPSCs were incubated with varying sized topographies and analyzed using a TaqMan hPSC Scorecard to determine germ layer gene expression. A) Self-renewal, B) Ectoderm, C) Mesoderm, and D) Endoderm differentiation were analyzed and samples were compared to glass control, which were normalized to a value of 1. Groups of genes expressed above a 2-fold change were considered to be upregulated while expression below a 0.5-fold change was considered as down regulation of the group of genes. Samples were graphed based upon gene expression filtration (method Cellular differentiation analysis and statistical analysis). Error bars represent standard deviation.

Table 5-2 : Gene expression fold change averages for each germ layer compared to the pluripotent scorecard control.

Target Name	Category	Control - Average	1 µm - Average	5 µm - Average
DRD4	Ectoderm	0.09		
MAP2	Ectoderm	10.80	6.72	4.09
NR2F1/NR2F2	Ectoderm	1.13		
NR2F2	Ectoderm	588.93	50.39	157.37
PAX3	Ectoderm	15.88		
PAX6	Ectoderm		7.64	
PRKCA	Ectoderm	0.9		
SDC2	Ectoderm	10.43	16.79	4.57
ZBTB16	Ectoderm	3.02		
COL2A1	Ectoderm		1.74	
CLDN1	Endoderm	10.42		2.32
EOMES	Endoderm	1.725	5.32	1.52
FOXA1	Endoderm	4.51	13.32	
FOXP2	Endoderm	2.2		
GATA6	Endoderm	1.315	3.86	0.13
KLF5	Endoderm	13.675	36.87	4.35
NODAL	Endoderm	0.1		
PRDM1	Endoderm	1.535	9.69	
HHEX	Endoderm		1.65	
AFP	Endoderm		3.85	
LEFTY2	Endoderm			2.6
COLEC10	Mesoderm		40.41	440.57
ABCA4	Mesoderm	15.06		
CDH5	Mesoderm	28.71		
COLEC10	Mesoderm	44.4		
ESM1	Mesoderm	29.81		
FOXF1	Mesoderm	106.42	150.14	
HAND1	Mesoderm	3.65	15.35	3.49
HEY1	Mesoderm	8.16	113.4	
HOPX	Mesoderm	543.9		
IL6ST	Mesoderm	22.54	8.46	4.85
NKX2-5	Mesoderm	27.61		
PDGFRA	Mesoderm	3.20	2.25	
RGS4	Mesoderm	38.99	67.69	
SNAI2	Mesoderm	37.06	20.56	
TBX3	Mesoderm	1.585	9.31	
TM4SF1	Mesoderm	27.6	62.59	
CXCL5	Self-renewal	0.95	3.89	3.59
DNMT3B	Self-renewal	0.01	0.03	0.01
NANOG	Self-renewal	0.29	0.05	0.08
POU5F1	Self-renewal	0.29	0.45	2.18
SOX2	Self-renewal	0.26	0.37	0.16
TRIM22	Self-renewal	2.24	1.22	

Table 5-3 : Gene expression fold change averages for each germ layer compared to the glass control.

Target Name	Category	1 µm - Average	5 µm - Average
MAP2	Ectoderm	2.13	0.27
NR2F2	Ectoderm	22.39	0.56
SDC2	Ectoderm	0.67	0.35
CLDN1	Endoderm	2.55	0.32
EOMES	Endoderm		0.19
FOXA1	Endoderm	1.97	
GATA6	Endoderm	0.72	0.64
KLF5	Endoderm	0.79	0.52
PRDM1	Endoderm	0.33	
COLEC10	Mesoderm	6.41	0.05
FOXF1	Mesoderm	0.71	
HAND1	Mesoderm	1.39	0.51
HEY1	Mesoderm	0.13	
IL6ST	Mesoderm	3.23	0.44
PDGFRA	Mesoderm	1.86	
RGS4	Mesoderm	1.14	
SNAI2	Mesoderm	3.78	
TBX3	Mesoderm	0.30	
TM4SF1	Mesoderm	0.58	
CXCL5	Self-renewal	0.48	0.04
DNMT3B	Self-renewal	0.49	0.11
NANOG	Self-renewal	9.78	0.47
POU5F1	Self-renewal	1.09	0.03
SOX2	Self-renewal	0.51	0.18
TRIM22	Self-renewal	3.92	

Table 5-4 : Target name and their gene names.

Target Name	Category	Gene Name
DRD4	Ectoderm	Dopamine Receptor D4
MAP2	Ectoderm	Microtubule-associated protein 2
NR2F1/NR2F2	Ectoderm	Nuclear Receptor Subfamily 2 Group F Member 1
NR2F2	Ectoderm	Nuclear Receptor Subfamily 2 Group F Member 2
PAX3	Ectoderm	Paired Box 3
PRKCA	Ectoderm	Protein Kinase C Alpha
SDC2	Ectoderm	Syndecan 2
ZBTB16	Ectoderm	Zinc Finger And BTB Domain Containing 16
COL2A1	Ectoderm	Collagen Type II Alpha 1 Chain
PAX6	Ectoderm	Paired Box 6
AFP	Endoderm	Alpha Fetoprotein
CLDN1	Endoderm	Claudin 1
FOXA1	Endoderm	Forkhead Box A1
GATA6	Endoderm	GATA Binding Protein 6
HHEX	Endoderm	Hematopoietically Expressed Homeobox
KLF5	Endoderm	Kruppel Like Factor 5
PRDM1	Endoderm	PR/SET Domain 1
EOMES	Endoderm	Eomesodermin
LEFTY2	Endoderm	Left-Right Determination Factor 2
FOXP2	Endoderm	Forkhead Box P2
NODAL	Endoderm	Nodal Growth Differentiation Factor
ABCA4	Mesoderm	ATP Binding Cassette Subfamily A Member 4
CDH5	Mesoderm	Cadherin 5
COLEC10	Mesoderm	Collectin Subfamily Member 10
ESM1	Mesoderm	Endothelial Cell Specific Molecule 1
FOXF1	Mesoderm	Forkhead Box F1
HAND1	Mesoderm	Heart And Neural Crest Derivatives Expressed 1
HEY1	Mesoderm	Hes Related Family BHLH Transcription Factor With YRPW Motif 1
HOPX	Mesoderm	HOP Homeobox
IL6ST	Mesoderm	Interleukin 6 Signal Transducer
NKX2-5	Mesoderm	NK2 Homeobox 5
PDGFRA	Mesoderm	Platelet Derived Growth Factor Receptor Alpha
RGS4	Mesoderm	Regulator Of G Protein Signaling 4
SNAI2	Mesoderm	Snail Family Transcriptional Repressor 2
TBX3	Mesoderm	T-Box 3
TM4SF1	Mesoderm	Transmembrane 4 L Six Family Member 1
CXCL5	Self-renewal	C-X-C Motif Chemokine Ligand 5
DNMT3B	Self-renewal	DNA Methyltransferase 3 Beta
NANOG	Self-renewal	Nanog Homeobox
POU5F1	Self-renewal	POU Class 5 Homeobox 1
SOX2	Self-renewal	SRY-Box 2
TRIM22	Self-renewal	Tripartite Motif Containing 22

CONCLUSION

With the low sample size, these data presented here are not definitive in establishing that any specific framework significantly affected cellular differentiation. However, these results indicate a trend of the effect of topography size on human iPSC differentiation, which will hopefully become significant once the sample size is increased upon repetition of the study. In addition, experiments investigating the influence of geometric shapes while maintaining size also need to be repeated to provide insight into other potential effects of shapes that may influence cell fate. Other points of improvement would be to seed at higher cell densities and perform quality control analysis and maintenance throughout the experiment. Future studies will focus on repeating these experiments and exploring other physical topological cues such as spacing and elevation effects to provide an all-inclusive list for optimal cellular differentiation. Once the germ layer differentiation is established, a more in-depth analysis of specific gene expression will be investigated to confirm the effects of these physical topographies on promoting specialized tissue regeneration. Nevertheless, our data shows the ability of 1 μm sized star shapes to differentiate iPSCs towards the mesodermal and endodermal germ layers when compared to the pluripotent scorecard control, while also having upregulated genes associated mesoderm and ectoderm germ layers when compared to the glass control. From this data, the combination of topological cues for cellular differentiation and the controlled drug release described in Chapter 4 could enable efficient differentiation into a desired cell type while controllably delivering drugs that enhance rates of tissue regeneration.

CHAPTER 6 : CONCLUSION AND FUTURE DIRECTIONS

Controlled drug delivery systems that include sequential and/or sustained drug delivery have been utilized to enhance the therapeutic effects of many current drugs by effectively delivering drugs in a time-dependent and repeatable manner. In the work presented here, controlled drug delivery systems were successfully integrated into 3D printed constructs, yielding controlled drug delivery vehicles. Additional studies using 3D printing also investigated the ability of topographical cues to direct cellular differentiation that, in future studies, could be combined with our controlled drug delivery vehicles for purposes of tissue regeneration. Our initial success with controlled drug delivery systems for the treatment of melanoma helped to pave the way towards investigating more novel controlled drug delivery technologies such as 3D printing. Using bioprinting and stereolithography, specifically two-photon polymerization (2PP), we were able to appraise the ability of the printed constructs to provide sustained and sequential drug delivery. In order to increase scaffolding versatility from 3D printed technologies, 2PP was further employed to study the effects of topological cues on cellular differentiation at micro- and nano-scale precision. Using 2PP to generate devices that possess both topological cues for cellular differentiation and incorporated controlled drug release would be a significant boon to the field of tissue engineering.

Initially, in this thesis, the results from investigating a controlled drug delivery system for the treatment of melanoma were presented. Using a murine melanoma model, the antitumor potential of combining ultrasound (US) with poly(lactic-co-glycolic acid) (PLGA) microspheres loaded with doxorubicin (DOX) was investigated. The aim was to achieve synergistic tumoricidal activity through direct and indirect US-

mediated damage of tumor cells combined with sustained and potentially controllable release (when combined with US) of DOX from microspheres. An *in vitro* release assay demonstrated the ability of US to affect the release kinetics of DOX from DOX-loaded PLGA microspheres by inducing a 12% increase in rate of release. *In vitro* viability assays demonstrated that combining US with DOX-loaded PLGA microspheres resulted in synergistic tumor cell (B16-F10 melanoma cells) killing. Melanoma-bearing mice were treated intratumorally with DOX (8 μg)-loaded microspheres and subjected to US treatment at the tumor site. This treatment could significantly extend survival (mean survival (MS) = 22.1 days) compared to untreated mice (MS = 10.4 days) and most other treatments, such as blank microspheres plus US (MS = 11.5 days) and DOX (8 μg)-loaded microspheres alone (MS = 13 days). The findings that immune checkpoint blockade did not significantly extend survival of mice treated with DOX (8 μg)-loaded microspheres plus US, and that tumor-free ("cured") mice were not protected from subsequent tumor rechallenge suggested minimal involvement of the adaptive immune response in the observed antitumor activity. Nevertheless, the synergistic increase in survival of melanoma-challenged mice treated with the combination of US and DOX-loaded microspheres implicates such a treatment methodology as a promising additional tool for combatting otherwise currently incurable cancers.

In the following study, with the aid of 3D bioprinting technology, a novel drug delivery device was fabricated and tested to evaluate sequential delivery functionality. With an alginate shell and a PLGA core, the fabricated tubes displayed sequential release of distinct fluorescent dyes and showed no cytotoxicity when incubated with the human embryonic kidney (HEK293) cell line or bone marrow

stromal stem cells (BMSC). The controlled differential release of drugs or proteins through such a delivery system has the potential for use in a wide variety of biomedical applications from treating cancer to regenerative medicine.

To see if controlled drug delivery systems could be fabricated with microscale precision using alternative 3D printing methods, 2PP was investigated. With 2PP, novel drug delivery devices were fabricated and tested using a model drug (fluorophore: rhodamine B). Poly(ethylene glycol) dimethacrylate (PEGDMA) devices were fabricated using a Photonic Professional GT two-photon polymerization system and rhodamine B was homogenously entrapped inside the polymer matrix during photopolymerization. These devices were printed with varying porosity and morphology and using varying printing parameters such as slicing and hatching distance. The effects of these variables on drug release kinetics were determined by evaluating device fluorescence over the course of one week. These PEGDMA-based structures were then investigated for toxicity and biocompatibility *in vitro*, where MTS assays were performed using a range of cell types including induced pluripotent stem cells (iPSCs). Overall, tuning the hatching distance, slicing distance, and pore size of the fabricated devices provided control of rhodamine B release, in each case presumably due to resulting changes in the motility of the small molecule and its access to structure edges. In general, increased spacing provided higher drug release while smaller spacing resulted in some occlusion, preventing media infiltration and thus resulting in reduced drug release. The devices had no cytotoxic effects on HEK293, BMSCs or iPSCs. Thus, we demonstrated the utility of 2PP to create biocompatible, complex miniature devices with fine details and tunable release of a model drug. When honed to a specific application, such materials could

be used as functional patient-matched grafts that promote healing and fight infections and pain or help direct cell or tissue growth *in vitro* using multiple chemical and physical cues.

In addition to the ability to release chemical cues, physical cues were investigated through 2PP printing in order to provide enhanced tissue regeneration. A Photonic Professional GT two-photon polymerization system was used to print differently sized topographies using an iPL-780 photoresist material. These samples were coated with matrigel and incubated with iPSCs for 7 days and cellular differentiation was analysed using a TaqMan hPSC scorecard for different germ layer differentitaion. The 1 µm size stars arrays were shown to differentiate iPSCs towards mesodermal and endodermal germ layers to a statistically greater extent when compared to the pluripotent scorecard controls. The gene expression in the mesoderm (*COLEC10, IL6ST, SNAI2*) and ectoderm (*MAP2, NR2F2*) germ layers was shown to be upregulated compared to the glass control, while with 5 µm size stars, gene expression was shown to be downregulated for ectoderm (*MAP2, SDC2*), mesoderm (*COLEC10, IL6ST*) and endoderm (*CLDN1*, *EOMES*). In addition, the photopolymerized iPL-780 material was shown to be nontoxic towards iPSCs for all 7 days of cell incubation. These systems allow for the potential provision of another tool for scaffolding, where tailoring and strategically designing surface topographies can assist in yielding a higher rate of tissue formation without overgrowth, such as the reduction of ectopic bone formation in bone tissue engineering. The ability of scaffolds to promote cellular differentiation via topographical cues as well as provide controlled drug release may lead to a new generation of scaffolds capable of inducing enhanced tissue regeneration.

The marriage of controlled drug delivery with 3D printing technologies provides a promising solution to the constant need for harvesting organs and tissues from the same patient or from donors. In the studies presented here, devices were fabricated that harbored the facility for controlled drug release and/or provided potential differentiation cues through physical topographies. These tools will help to increase the versatility of 3D printing as a means to create a plethora of devices such as improved scaffolds for tissue engineering or implants with drug releasing capabilities to treat diseases such as cancer. The future directions for these studies will be the implementation of devices manufactured from 3D technology in an *in vivo* setting to investigate their potential to enhance tissue regeneration. With these future studies, the combination of 3D printing with controlled drug delivery systems and cellular differentiation cues will aid in designing scaffolds capable of growing viable organs that will ultimately save the lives of millions of people globally.

REFERENCES

1. Uhrich, K. E.; Cannizzaro, S. M.; Langer, R. S.; Shakesheff, K. M., Polymeric systems for controlled drug release. *Chem Rev* **1999,** *99* (11), 3181-98.
2. Longmire, M.; Choyke, P. L.; Kobayashi, H., Clearance properties of nano-sized particles and molecules as imaging agents: Considerations and Caveats. *Nanomedicine (London, England)* **2008,** *3* (5), 703-717.
3. Blanco, E.; Shen, H.; Ferrari, M., Principles of nanoparticle design for overcoming biological barriers to drug delivery. *Nature Biotechnology* **2015,** *33* (9), 941-951.
4. Langer, R., Invited review polymeric delivery systems for controlled drug release. *Chemical Engineering Communications* **1980,** *6* (1-3), 1-48.
5. Leong, K. W.; Langer, R., Polymeric controlled drug delivery. *Advanced Drug Delivery Reviews* **1988,** *1* (3), 199-233.
6. Jimmy, B.; Jose, J., Patient medication adherence: measures in daily practice. *Oman Medical Journal* **2011,** *26* (3), 155-9.
7. Hixson-Wallace, J. A.; Dotson, J. B.; Blakey, S. A., Effect of regimen complexity on patient satisfaction and compliance with warfarin therapy. *Clinical and applied thrombosis/hemostasis : official journal of the International Academy of Clinical and Applied Thrombosis/Hemostasis* **2001,** *7* (1), 33-7.
8. van den Bemt, B. J.; Zwikker, H. E.; van den Ende, C. H., Medication adherence in patients with rheumatoid arthritis: a critical appraisal of the existing literature. *Expert Review of Clinical Immunology* **2012,** *8* (4), 337-51.
9. http://optn.transplant.hrsa.gov/data/ (accessed March 2nd).
10. Martins, A. M.; Eng, G.; Caridade, S. G.; Mano, J. F.; Reis, R. L.; Vunjak-Novakovic, G., Electrically conductive chitosan/carbon scaffolds for cardiac tissue Engineering. *Biomacromolecules* **2014,** *15* (2), 635-643.
11. Didenko, V. V.; Ngo, H.; Minchew, C. L.; Boudreaux, D. J.; Widmayer, M. A.; Baskin, D. S., Visualization of irreparable ischemic damage in brain by selective labeling of double strand blunt-ended DNA breaks. *Molecular Medicine (Cambridge, Mass.)* **2002,** *8* (12), 818-23.
12. Laumonier, T.; Ménétrey, J., Regenerative medicine for cartilage. In *The Knee Joint*, Springer Paris: 2012; pp 511-516.
13. Association, A. H. Cardiac Medications. http://www.heart.org/HEARTORG/Conditions/HeartAttack/PreventionTreatmentofHeartAttack/Cardiac-Medications_UCM_303937_Article.jsp (accessed June 21).
14. Brandt, K. D.; Mazzuca, S. A.; Buckwalter, K. A., Acetaminophen, like conventional NSAIDs, may reduce synovitis in osteoarthritic knees. *Rheumatology* **2006,** *45* (11), 1389-1394.
15. Balmaceda, C. M., Evolving guidelines in the use of topical nonsteroidal anti-inflammatory drugs in the treatment of osteoarthritis. *BMC Musculoskelet. Disord.* **2014,** *15*, 5.
16. Shakesheff, K., 3D printing and the healthcare revolution. In *Future History Now Talks: Part I*, Zurich: London, 2013.
17. Yang, S.; Leong, K. F.; Du, Z.; Chua, C. K., The design of scaffolds for use in tissue engineering. Part I. Traditional factors. *Tissue Eng* **2001,** *7* (6), 679-89.

18. Ikeda, T.; Ikeda, K.; Yamamoto, K.; Ishizaki, H.; Yoshizawa, Y.; Yanagiguchi, K.; Yamada, S.; Hayashi, Y., Fabrication and characteristics of chitosan sponge as a tissue engineering scaffold. *Biomed Res. Int.* **2014**, 8.
19. Drury, J. L.; Mooney, D. J., Hydrogels for tissue engineering: scaffold design variables and applications. *Biomaterials* **2003,** *24* (24), 4337-4351.
20. Hollister, S. J., Porous scaffold design for tissue engineering. *Nat. Mater.* **2005,** *4*, 518.
21. Langer, R., Perspectives and challenges in tissue engineering and regenerative medicine. *Advanced Materials* **2009,** *21* (32-33), 3235-3236.
22. Ikada, Y., Challenges in tissue engineering. *Journal of the Royal Society Interface* **2006,** *3* (10), 589-601.
23. Yu, J.; Vodyanik, M. A.; Smuga-Otto, K.; Antosiewicz-Bourget, J.; Frane, J. L.; Tian, S.; Nie, J.; Jonsdottir, G. A.; Ruotti, V.; Stewart, R.; Slukvin, I. I.; Thomson, J. A., Induced pluripotent stem cell lines derived from human somatic cells. *Science* **2007,** *318* (5858), 1917-1920.
24. Franz, S.; Rammelt, S.; Scharnweber, D.; Simon, J. C., Immune responses to implants - a review of the implications for the design of immunomodulatory biomaterials. *Biomaterials* **2011,** *32* (28), 6692-709.
25. Vo, T. N.; Kasper, F. K.; Mikos, A. G., Strategies for controlled delivery of growth factors and cells for bone regeneration. *Advanced Drug Delivery Reviews* **2012,** *64* (12), 1292-1309.
26. Jaklenec, A.; Hinckfuss, A.; Bilgen, B.; Ciombor, D. M.; Aaron, R.; Mathiowitz, E., Sequential release of bioactive IGF-I and TGF-beta 1 from PLGA microsphere-based scaffolds. *Biomaterials* **2008,** *29* (10), 1518-25.
27. Bose, S.; Vahabzadeh, S.; Bandyopadhyay, A., Bone tissue engineering using 3D printing. *Materials Today* **2013,** *16* (12), 496-504.
28. Kolesky, D. B.; Truby, R. L.; Gladman, A. S.; Busbee, T. A.; Homan, K. A.; Lewis, J. A., 3D Bioprinting of vascularized, heterogeneous cell-laden tissue constructs. *Advanced Materials* **2014,** *26* (19), 3124-3130.
29. Yu, T.; Dylan, J. R.; Thomas, C. T.; Richard, P. V.; Michael, J. Y.; Mark, S. K.; Christopher, J. D.; William Scott, A.; Roger, R. M.; Ying, M., 3D printing facilitated scaffold-free tissue unit fabrication. *Biofabrication* **2014,** *6* (2), 024111.
30. Ingber, D. E., Mechanical signaling and the cellular response to extracellular matrix in angiogenesis and cardiovascular physiology. *Circulation Research* **2002,** *91* (10), 877-887.
31. Bianco, P.; Robey, P. G., Stem cells in tissue engineering. *Nature* **2001,** *414*, 118.
32. Do, A.-V.; Khorsand, B.; Geary, S. M.; Salem, A. K., 3D Printing of scaffolds for tissue regeneration applications. *Advanced Healthcare Materials* **2015,** *4* (12), 1742-1762.
33. Ventola, C. L., Medical applications for 3D printing: current and projected uses. *Pharmacy and Therapeutics* **2014,** *39* (10), 704-711.
34. Tiwari, G.; Tiwari, R.; Sriwastawa, B.; Bhati, L.; Pandey, S.; Pandey, P.; Bannerjee, S. K., Drug delivery systems: An updated review. *International Journal of Pharmaceutical Investigation* **2012,** *2* (1), 2-11.
35. Murphy, S. V.; Atala, A., 3D bioprinting of tissues and organs. *Nature Biotechnology* **2014,** *32* (8), 773-85.

36. Cui, H.; Nowicki, M.; Fisher, J. P.; Zhang, L. G., 3D bioprinting for organ regeneration. *Advanced Healthcare Materials* **2016**.
37. Aw, M. S.; Addai-Mensah, J.; Losic, D., A multi-drug delivery system with sequential release using titania nanotube arrays. *Chemical Communications* **2012,** *48* (27), 3348-3350.
38. Journé, F.; Chaboteaux, C.; Laurent ∗, G.; Body, J. J., Sequence-dependent synergistic effects of ibandronate in combination with antiestrogens on growth inhibition of estrogen receptor-positive breast cancer cells. *Bone* **2006,** *38* (3, Supplement 1), 52-53.
39. Lee, S. S.; Hughes, P.; Ross, A. D.; Robinson, M. R., Biodegradable implants for sustained drug release in the eye. *Pharmaceutical Research* **2010,** *27* (10), 2043-2053.
40. Musch, D. C.; Martin, D. F.; Gordon, J. F.; Davis, M. D.; Kuppermann, B. D., Treatment of cytomegalovirus retinitis with a sustained-release ganciclovir implant. *New England Journal of Medicine* **1997,** *337* (2), 83-90.
41. Makkouk, A.; Joshi, V. B.; Wongrakpanich, A.; Lemke, C. D.; Gross, B. P.; Salem, A. K.; Weiner, G. J., Biodegradable microparticles loaded with doxorubicin and CpG ODN for in situ immunization against cancer. *AAPS J* **2015,** *17* (1), 184-93.
42. Lee, J.-H.; Chen, K.-J.; Noh, S.-H.; Garcia, M. A.; Wang, H.; Lin, W.-Y.; Jeong, H.; Kong, B. J.; Stout, D. B.; Cheon, J.; Tseng, H.-R., On-Demand drug release system for in vivo cancer treatment through self-assembled magnetic nanoparticles. *Angewandte Chemie International Edition* **2013,** *52* (16), 4384-4388.
43. Richardson, T. P.; Peters, M. C.; Ennett, A. B.; Mooney, D. J., Polymeric system for dual growth factor delivery. *Nature Biotechnology* **2001,** *19* (11), 1029-34.
44. Chen, R. R.; Silva, E. A.; Yuen, W. W.; Mooney, D. J., Spatio-temporal VEGF and PDGF delivery patterns blood vessel formation and maturation. *Pharmaceutical Research* **2007,** *24* (2), 258-64.
45. Suciati, T.; Howard, D.; Barry, J.; Everitt, N. M.; Shakesheff, K. M.; Rose, F. R., Zonal release of proteins within tissue engineering scaffolds. *Journal of Materials Science. Materials in Medicine* **2006,** *17* (11), 1049-56.
46. Sachlos, E.; Czernuszka, J. T., Making tissue engineering scaffolds work. Review: the application of solid freeform fabrication technology to the production of tissue engineering scaffolds. *Eur Cell Mater* **2003,** *5*, 29-39; discussion 39-40.
47. Wust, S.; Muller, R.; Hofmann, S., Controlled positioning of cells in biomaterials-approaches towards 3D tissue printing. *Journal of Functional Biomaterials* **2011,** *2* (3), 119-54.
48. Thomson, R. C.; Shung, A. K.; Yaszemski, M. J.; Mikos, A. G., CHAPTER 21 - POLYMER SCAFFOLD PROCESSING. In *Principles of Tissue Engineering (Second Edition)*, Academic Press: San Diego, 2000; pp 251-262.
49. Correlo, V. M.; Boesel, L. F.; Pinho, E.; Costa-Pinto, A. R.; Alves da Silva, M. L.; Bhattacharya, M.; Mano, J. F.; Neves, N. M.; Reis, R. L., Melt-based compression-molded scaffolds from chitosan-polyester blends and composites: Morphology and mechanical properties. *J Biomed Mater Res A* **2009,** *91* (2), 489-504.
50. Garg, T.; Singh, O.; Arora, S.; Murthy, R., Scaffold: a novel carrier for cell and drug delivery. *Critical Reviews in Therapeutic Drug Carrier Systems* **2012,** *29* (1), 1-63.

51. Leong, K. F.; Cheah, C. M.; Chua, C. K., Solid freeform fabrication of three-dimensional scaffolds for engineering replacement tissues and organs. *Biomaterials* **2003,** *24* (13), 2363-78.
52. Mikos, A. G.; Temenoff, J. S., Formation of highly porous biodegradable scaffolds for tissue engineering. *Electronic Journal of Biotechnology* **2000,** *3*, 23-24.
53. Kim, B. S.; Mooney, D. J., Engineering smooth muscle tissue with a predefined structure. *J Biomed Mater Res* **1998,** *41* (2), 322-32.
54. Lee, S. J.; Oh, S. H.; Liu, J.; Soker, S.; Atala, A.; Yoo, J. J., The use of thermal treatments to enhance the mechanical properties of electrospun poly(ε-caprolactone) scaffolds. *Biomaterials* **2008,** *29* (10), 1422-1430.
55. Peltola, S. M.; Melchels, F. P. W.; Grijpma, D. W.; Kellomäki, M., A review of rapid prototyping techniques for tissue engineering purposes. *Annals of Medicine* **2008,** *40* (4), 268-280.
56. Hribar, K. C.; Soman, P.; Warner, J.; Chung, P.; Chen, S., Light-assisted direct-write of 3D functional biomaterials. *Lab on a chip* **2014,** *14* (2), 268-75.
57. Rucker, M.; Laschke, M. W.; Junker, D.; Carvalho, C.; Schramm, A.; Mulhaupt, R.; Gellrich, N. C.; Menger, M. D., Angiogenic and inflammatory response to biodegradable scaffolds in dorsal skinfold chambers of mice. *Biomaterials* **2006,** *27* (29), 5027-38.
58. Dhandayuthapani, B.; Yoshida, Y.; Maekawa, T.; Kumar, D. S., Polymeric scaffolds in tissue engineering application: a review. International journal of polymer science 2011, 2011.
59. Chen, M.; Le, D. Q.; Baatrup, A.; Nygaard, J. V.; Hein, S.; Bjerre, L.; Kassem, M.; Zou, X.; Bunger, C., Self-assembled composite matrix in a hierarchical 3-D scaffold for bone tissue engineering. *Acta Biomaterialia* **2011,** *7* (5), 2244-55.
60. Peter, S. J.; Miller, M. J.; Yasko, A. W.; Yaszemski, M. J.; Mikos, A. G., Polymer concepts in tissue engineering. *Journal of Biomedical Materials Research* **1998,** *43* (4), 422-427.
61. Zhu, Y.; Gao, C.; Shen, J., Surface modification of polycaprolactone with poly(methacrylic acid) and gelatin covalent immobilization for promoting its cytocompatibility. *Biomaterials* **2002,** *23* (24), 4889-4895.
62. Spath, S.; Seitz, H., Influence of grain size and grain-size distribution on workability of granules with 3D printing. *Int J Adv Manuf Technol* **2014,** *70* (1-4), 135-144.
63. Cook, J. R.; Crute, B. E.; Patrone, L. M.; Gabriels, J.; Lane, M. E.; Van Buskirk, R. G., Microporosity of the substratum regulates differentiation of MDCK cells in vitro. *In vitro Cellular & Developmental Biology : Journal of the Tissue Culture Association* **1989,** *25* (10), 914-22.
64. Lawrence, B. J.; Madihally, S. V., Cell colonization in degradable 3D porous matrices. *Cell Adhesion & Migration* **2008,** *2* (1), 9-16.
65. Lee, H.; Ahn, S.; Bonassar, L. J.; Kim, G., Cell(MC3T3-E1)-printed poly(ϵ-caprolactone)/alginate hybrid scaffolds for tissue regeneration. *Macromolecular Rapid Communications* **2013,** *34* (2), 142-149.
66. Shim, J. H.; Kim, J. Y.; Park, M.; Park, J.; Cho, D. W., Development of a hybrid scaffold with synthetic biomaterials and hydrogel using solid freeform fabrication technology. *Biofabrication* **2011,** *3* (3), 034102.

67. Lee, J. S.; Hong, J. M.; Jung, J. W.; Shim, J. H.; Oh, J. H.; Cho, D. W., 3D printing of composite tissue with complex shape applied to ear regeneration. *Biofabrication* **2014,** *6* (2), 024103.
68. Wei GB, M. P., Nanostructured biomaterials for regeneration. *Adv Funct Mater.* **2008,** *18*, 3568–3582.
69. Korossis S, B. F., Southgate J, Ingham E, Fisher J., Regional biomechanical and histological characterisation of the passive porcine urinary bladder: implications for augmentation and tissue engineering strategies. *Biomaterials.* **2009,** *30*, 266–275.
70. Groeber F, H. M., Hampel M, Hinderer S, Schenke-Layland K. , Skin tissue engineering – in vivo and in vitro applications. . *Clin Plast Surg.* **2012,** *39*, 33–38.
71. Guoyou, H.; Lin, W.; ShuQi, W.; Yulong, H.; Jinhui, W.; Qiancheng, Z.; Feng, X.; Tian Jian, L., Engineering three-dimensional cell mechanical microenvironment with hydrogels. *Biofabrication* **2012,** *4* (4), 042001.
72. Nichol, J. W.; Khademhosseini, A., Modular tissue engineering: engineering biological tissues from the bottom up. *Soft Matter* **2009,** *5* (7), 1312-1319.
73. Napolitano AP, C. P., Dean DM, Morgan JR., Dynamics of the self-assembly of complex cellular aggregates on micromolded nonadhesive hydrogels. *Tissue Eng.* **2007,** *13*, 2087–2094
74. Chung SE, P. W., Shin S, Lee SA, Kwon S. , Guided and fluidic self-assembly of microstructures using railed microfluidic channels. *Nat Mater.* **2008,** *7*, 581–587.
75. Xu F, W. C., Rengarajan V, Finley TD, Keles HO, Sung Y, Li B, Gurkan UA, Demirci U., Three-dimensional magnetic assembly of microscale hydrogels. *Adv Mater.* **2011,** *23:* , 4254–4460.
76. Xu, F.; Finley, T. D.; Turkaydin, M.; Sung, Y.; Gurkan, U. A.; Yavuz, A. S.; Guldiken, R. O.; Demirci, U., The assembly of cell-encapsulating microscale hydrogels using acoustic waves. *Biomaterials* **2011,** *32* (31), 7847-55.
77. Geckil, H.; Xu, F.; Zhang, X.; Moon, S.; Demirci, U., Engineering hydrogels as extracellular matrix mimics. *Nanomedicine (London, England)* **2010,** *5* (3), 469-84.
78. Lee, K. W.; Wang, S.; Lu, L.; Jabbari, E.; Currier, B. L.; Yaszemski, M. J., Fabrication and characterization of poly(propylene fumarate) scaffolds with controlled pore structures using 3-dimensional printing and injection molding. *Tissue Eng* **2006,** *12* (10), 2801-11.
79. Li, X.; Cui, R.; Sun, L.; Aifantis, K. E.; Fan, Y.; Feng, Q.; Cui, F.; Watari, F., 3D-Printed biopolymers for tissue engineering application. *International Journal of Polymer Science* **2014,** *2014*, 13.
80. Wu, B.; Klatzky, R. L.; Stetten, G., Visualizing 3D objects from 2D cross sectional images displayed in-situ versus ex-situ. *Journal of Experimental Psychology. Applied* **2010,** *16* (1), 45-59.
81. Talib, M.; Covington, J. A.; Bolarinwa, A., Characterization of fabricated three dimensional scaffolds of bioceramic-polymer composite via microstereolithography technique. *AIP Conference Proceedings* **2014,** *1584* (1), 129-135.
82. Tonomura, A.; Mizuno, D.; Hisada, A.; Kuno, N.; Ando, Y.; Sumita, Y.; Honda, M. J.; Satomura, K.; Sakurai, H.; Ueda, M.; Kagami, H., Differential effect of scaffold shape on dentin regeneration. *Annals of Biomedical Engineering* **2010,** *38* (4), 1664-71.

83. Berger, A., Magnetic resonance imaging. *BMJ (Clinical research ed.)* **2002,** *324* (7328), 35.
84. Bioengineering, N. I. o. B. I. a. Computed Tomography (CT). http://www.nibib.nih.gov/science-education/science-topics/computed-tomography-ct (accessed October 13th).
85. Sachs, E. M.; Haggerty, J. S.; Cima, M. J.; Williams, P. A., Three-dimensional printing techniques. Google Patents: **1993**.
86. Cima, M.; Sachs, E.; Fan, T.; Bredt, J. F.; Michaels, S. P.; Khanuja, S.; Lauder, A.; Lee, S. J. J.; Brancazio, D.; Curodeau, A., Three-dimensional printing techniques. Google Patents: **1995**.
87. Yousefi, A.-M.; Gauvin, C.; Sun, L.; DiRaddo, R. W.; Fernandes, J., Design and fabrication of 3D-plotted polymeric scaffolds in functional tissue engineering. *Polymer Engineering & Science* **2007,** *47* (5), 608-618.
88. Ozbolat, I. T.; Chen, H.; Yu, Y., Development of 'Multi-arm Bioprinter' for hybrid biofabrication of tissue engineering constructs. *Robot. Comput.-Integr. Manuf.* **2014,** *30* (3), 295-304.
89. Billiet, T.; Gevaert, E.; De Schryver, T.; Cornelissen, M.; Dubruel, P., The 3D printing of gelatin methacrylamide cell-laden tissue-engineered constructs with high cell viability. *Biomaterials* **2014,** *35* (1), 49-62.
90. Bertassoni, L. E.; Cardoso, J. C.; Manoharan, V.; Cristino, A. L.; Bhise, N. S.; Araujo, W. A.; Zorlutuna, P.; Vrana, N. E.; Ghaemmaghami, A. M.; Dokmeci, M. R.; Khademhosseini, A., Direct-write bioprinting of cell-laden methacrylated gelatin hydrogels. *Biofabrication* **2014,** *6* (2), 024105.
91. Serra, T.; Ortiz-Hernandez, M.; Engel, E.; Planell, J. A.; Navarro, M., Relevance of PEG in PLA-based blends for tissue engineering 3D-printed scaffolds. *Materials Science & Engineering. C, Materials for Biological Applications* **2014,** *38*, 55-62.
92. Fedorovich, N. E.; De Wijn, J. R.; Verbout, A. J.; Alblas, J.; Dhert, W. J., Three-dimensional fiber deposition of cell-laden, viable, patterned constructs for bone tissue printing. *Tissue Eng Part A* **2008,** *14* (1), 127-33.
93. Matsuda, T.; Mizutani, M., Liquid acrylate-endcapped biodegradable poly(epsilon-caprolactone-co-trimethylene carbonate). II. Computer-aided stereolithographic microarchitectural surface photoconstructs. *J Biomed Mater Res* **2002,** *62* (3), 395-403.
94. Griffith, M. L.; Halloran, J. W., Freeform fabrication of ceramics via stereolithography. *Journal of the American Ceramic Society* **1996,** *79* (10), 2601-2608.
95. Dhariwala, B.; Hunt, E.; Boland, T., Rapid prototyping of tissue-engineering constructs, using photopolymerizable hydrogels and stereolithography. *Tissue Eng* **2004,** *10* (9-10), 1316-22.
96. Cooke, M. N.; Fisher, J. P.; Dean, D.; Rimnac, C.; Mikos, A. G., Use of stereolithography to manufacture critical-sized 3D biodegradable scaffolds for bone ingrowth. *J Biomed Mater Res B Appl Biomater* **2003,** *64* (2), 65-9.
97. Worthington, K. S.; Wiley, L. A.; Kaalberg, E. E.; Collins, M. M.; Mullins, R. F.; Stone, E. M.; Tucker, B. A., Two-photon polymerization for production of human iPSC-derived retinal cell grafts. *Acta Biomaterialia* **2017,** *55*, 385-395.

98. Schuster, M.; Chen, S.-X.; Liska, R.; Rumpler, M.; Turecek, C.; Varga, F.; Stampfl, J., Development of biodegradable photopolymers for bone tissue engineering. RadTech Europe 2005 Conference & Exhibition: **2005**.
99. Lee, S. J.; Nowicki, M.; Harris, B.; Zhang, L. G., Fabrication of a highly aligned neural scaffold via a table top stereolithography 3D printing and clectrospinning. *Tissue Engineering. Part A* **2017,** *23* (11-12), 491-502.
100. Lee, K.-S.; Kim, R.; Prabhakaran, P.; Yang, D. Y.; Woo Lim, T.; Hu Park, S., Two-photon stereolithography. *J Nonlinear Opt Phys* **2007**; Vol. 16, p 59-74.
101. Fischer, A. C.; Mäntysalo, M.; Niklaus, F., Chapter 26 - Inkjet printing, laser-based micromachining and micro 3D printing technologies for MEMS. In *Handbook of Silicon Based MEMS Materials and Technologies (Second Edition)*, William Andrew Publishing: Boston, 2015; pp 550-564.
102. Zhou, X.; Hou, Y.; Lin, J., A review on the processing accuracy of two-photon polymerization. *AIP Advances* **2015,** *5* (3), 030701.
103. Li, J.; He, L.; Zhou, C.; Zhou, Y.; Bai, Y.; Lee, F. Y.; Mao, J. J., 3D printing for regenerative medicine: From bench to bedside. *MRS Bulletin* **2015,** *40* (02), 145-154.
104. Tamimi, F.; Torres, J.; Al-Abedalla, K.; Lopez-Cabarcos, E.; Alkhraisat, M. H.; Bassett, D. C.; Gbureck, U.; Barralet, J. E., Osseointegration of dental implants in 3D-printed synthetic onlay grafts customized according to bone metabolic activity in recipient site. *Biomaterials* **2014,** *35* (21), 5436-45.
105. Tarafder, S.; Davies, N. M.; Bandyopadhyay, A.; Bose, S., 3D printed tricalcium phosphate scaffolds: Effect of SrO and MgO doping on osteogenesis in a rat distal femoral defect model. *Biomater Sci* **2013,** *1* (12), 1250-1259.
106. Fielding, G.; Bose, S., SiO2 and ZnO dopants in three-dimensionally printed tricalcium phosphate bone tissue engineering scaffolds enhance osteogenesis and angiogenesis in vivo. *Acta Biomaterialia* **2013,** *9* (11), 9137-48.
107. Strobel, L. A.; Rath, S. N.; Maier, A. K.; Beier, J. P.; Arkudas, A.; Greil, P.; Horch, R. E.; Kneser, U., Induction of bone formation in biphasic calcium phosphate scaffolds by bone morphogenetic protein-2 and primary osteoblasts. *J Tissue Eng Regen Med* **2014,** *8* (3), 176-85.
108. Choi, H. J.; Kim, J. M.; Kwon, E.; Che, J. H.; Lee, J. I.; Cho, S. R.; Kang, S. K.; Ra, J. C.; Kang, B. C., Establishment of efficacy and safety assessment of human adipose tissue-derived mesenchymal stem cells (hATMSCs) in a nude rat femoral segmental defect model. *J Korean Med Sci* **2011,** *26* (4), 482-91.
109. Shim, J. H.; Kim, S. E.; Park, J. Y.; Kundu, J.; Kim, S. W.; Kang, S. S.; Cho, D. W., Three-dimensional printing of rhBMP-2-loaded scaffolds with long-term delivery for enhanced bone regeneration in a rabbit diaphyseal defect. *Tissue Eng Part A* **2014,** *20* (13-14), 1980-92.
110. Poldervaart, M. T.; Wang, H.; van der Stok, J.; Weinans, H.; Leeuwenburgh, S. C.; Oner, F. C.; Dhert, W. J.; Alblas, J., Sustained release of BMP-2 in bioprinted alginate for osteogenicity in mice and rats. *PLoS One* **2013,** *8* (8), e72610.
111. Poldervaart, M. T.; Gremmels, H.; van Deventer, K.; Fledderus, J. O.; Oner, F. C.; Verhaar, M. C.; Dhert, W. J.; Alblas, J., Prolonged presence of VEGF promotes vascularization in 3D bioprinted scaffolds with defined architecture. *J Control Release* **2014,** *184*, 58-66.

112. Xu, T.; Binder, K. W.; Albanna, M. Z.; Dice, D.; Zhao, W.; Yoo, J. J.; Atala, A., Hybrid printing of mechanically and biologically improved constructs for cartilage tissue engineering applications. *Biofabrication* **2013,** *5* (1), 015001.
113. Pati, F.; Jang, J.; Ha, D.-H.; Won Kim, S.; Rhie, J.-W.; Shim, J.-H.; Kim, D.-H.; Cho, D.-W., Printing three-dimensional tissue analogues with decellularized extracellular matrix bioink. *Nat Commun* **2014,** *5*.
114. Chang, J. W.; Park, S. A.; Park, J. K.; Choi, J. W.; Kim, Y. S.; Shin, Y. S.; Kim, C. H., Tissue-engineered tracheal reconstruction using three-dimensionally printed artificial tracheal graft: preliminary report. *Artif Organs* **2014,** *38* (6), E95-E105.
115. Lee, C. H.; Cook, J. L.; Mendelson, A.; Moioli, E. K.; Yao, H.; Mao, J. J., Regeneration of the articular surface of the rabbit synovial joint by cell homing: a proof of concept study. *Lancet* **2010,** *376* (9739), 440-8.
116. Lee, C. H.; Marion, N. W.; Hollister, S.; Mao, J. J., Tissue formation and vascularization in anatomically shaped human joint condyle ectopically in vivo. *Tissue Eng Part A* **2009,** *15* (12), 3923-30.
117. Fedorovich, N. E.; Schuurman, W.; Wijnberg, H. M.; Prins, H. J.; van Weeren, P. R.; Malda, J.; Alblas, J.; Dhert, W. J., Biofabrication of osteochondral tissue equivalents by printing topologically defined, cell-laden hydrogel scaffolds. *Tissue Eng Part C Methods* **2012,** *18* (1), 33-44.
118. Lee, C. H.; Hajibandeh, J.; Suzuki, T.; Fan, A.; Shang, P.; Mao, J. J., Three-dimensional printed multiphase scaffolds for regeneration of periodontium complex. *Tissue Eng Part A* **2014,** *20* (7-8), 1342-51.
119. Skardal, A.; Mack, D.; Kapetanovic, E.; Atala, A.; Jackson, J. D.; Yoo, J.; Soker, S., Bioprinted amniotic fluid-derived stem cells accelerate healing of large skin wounds. *Stem Cells Transl Med* **2012,** *1* (11), 792-802.
120. Hong, J. M.; Kim, B. J.; Shim, J. H.; Kang, K. S.; Kim, K. J.; Rhie, J. W.; Cha, H. J.; Cho, D. W., Enhancement of bone regeneration through facile surface functionalization of solid freeform fabrication-based three-dimensional scaffolds using mussel adhesive proteins. *Acta biomaterialia* **2012,** *8* (7), 2578-86.
121. Gross, B. C.; Erkal, J. L.; Lockwood, S. Y.; Chen, C.; Spence, D. M., Evaluation of 3D printing and its potential impact on biotechnology and the chemical sciences. *Analytical Chemistry* **2014,** *86* (7), 3240-3253.
122. Wong, K. V.; Hernandez, A., A review of additive manufacturing. *ISRN Mechanical Engineering* **2012,** *2012*, 10.
123. Jensen, J.; Rolfing, J. H.; Le, D. Q.; Kristiansen, A. A.; Nygaard, J. V.; Hokland, L. B.; Bendtsen, M.; Kassem, M.; Lysdahl, H.; Bunger, C. E., Surface-modified functionalized polycaprolactone scaffolds for bone repair: in vitro and in vivo experiments. *J Biomed Mater Res A* **2014,** *102* (9), 2993-3003.
124. Costa, P. F.; Vaquette, C.; Zhang, Q.; Reis, R. L.; Ivanovski, S.; Hutmacher, D. W., Advanced tissue engineering scaffold design for regeneration of the complex hierarchical periodontal structure. *Journal of Clinical Periodontology* **2014,** *41* (3), 283-94.
125. Gibson, I.; Shi, D., Material properties and fabrication parameters in selective laser sintering process. *Rapid Prototyping Journal* **1997,** *3* (4), 129-136.
126. Duan, B.; Cheung, W. L.; Wang, M., Optimized fabrication of Ca-P/PHBV nanocomposite scaffolds via selective laser sintering for bone tissue engineering. *Biofabrication* **2011,** *3* (1), 015001.

127. Liu, F.-H., Synthesis of biomedical composite scaffolds by laser sintering: Mechanical properties and in vitro bioactivity evaluation. *Applied Surface Science* **2014,** *297* (0), 1-8.
128. Keriquel, V.; Guillemot, F.; Arnault, I.; Guillotin, B.; Miraux, S.; Amedee, J.; Fricain, J. C.; Catros, S., In vivo bioprinting for computer- and robotic-assisted medical intervention: preliminary study in mice. *Biofabrication* **2010,** *2* (1), 014101.
129. Zieber, L.; Or, S.; Ruvinov, E.; Cohen, S., Microfabrication of channel arrays promotes vessel-like network formation in cardiac cell construct and vascularization in vivo. *Biofabrication* **2014,** *6* (2), 024102.
130. Tarafder, S.; Balla, V. K.; Davies, N. M.; Bandyopadhyay, A.; Bose, S., Microwave-sintered 3D printed tricalcium phosphate scaffolds for bone tissue engineering. *J Tissue Eng Regen Med* **2013,** *7* (8), 631-41.
131. Killat, J.; Reimers, K.; Choi, C. Y.; Jahn, S.; Vogt, P. M.; Radtke, C., Cultivation of keratinocytes and fibroblasts in a three-dimensional bovine collagen-elastin matrix (Matriderm(R)) and application for full thickness wound coverage in vivo. *Int J Mol Sci* **2013,** *14* (7), 14460-74.
132. Gaebel, R.; Ma, N.; Liu, J.; Guan, J.; Koch, L.; Klopsch, C.; Gruene, M.; Toelk, A.; Wang, W.; Mark, P.; Wang, F.; Chichkov, B.; Li, W.; Steinhoff, G., Patterning human stem cells and endothelial cells with laser printing for cardiac regeneration. *Biomaterials* **2011,** *32* (35), 9218-30.
133. Tumbleston, J. R.; Shirvanyants, D.; Ermoshkin, N.; Janusziewicz, R.; Johnson, A. R.; Kelly, D.; Chen, K.; Pinschmidt, R.; Rolland, J. P.; Ermoshkin, A.; Samulski, E. T.; DeSimone, J. M., Additive manufacturing. Continuous liquid interface production of 3D objects. *Science* **2015,** *347* (6228), 1349-52.
134. Stampfl, J.; Baudis, S.; Heller, C.; Liska, R.; Neumeister, A.; Kling, R.; Ostendorf, A.; Spitzbart, M., Photopolymers with tunable mechanical properties processed by laser-based high-resolution stereolithography. *Journal of Micromechanics and Microengineering* **2008,** *18* (12), 125014.
135. Lee, J. W.; Kang, K. S.; Lee, S. H.; Kim, J. Y.; Lee, B. K.; Cho, D. W., Bone regeneration using a microstereolithography-produced customized poly(propylene fumarate)/diethyl fumarate photopolymer 3D scaffold incorporating BMP-2 loaded PLGA microspheres. *Biomaterials* **2011,** *32* (3), 744-52.
136. Park, J. H.; Jung, J. W.; Kang, H. W.; Joo, Y. H.; Lee, J. S.; Cho, D. W., Development of a 3D bellows tracheal graft: mechanical behavior analysis, fabrication and an in vivo feasibility study. *Biofabrication* **2012,** *4* (3), 035004.
137. Li, X.; He, J.; Bian, W.; Li, Z.; Li, D.; Snedeker, J. G., A novel silk-TCP-PEEK construct for anterior cruciate ligament reconstruction: an off-the shelf alternative to a bone-tendon-bone autograft. *Biofabrication* **2014,** *6* (1), 015010.
138. Jayasinghe, S. N., Cell electrospinning: a novel tool for functionalising fibres, scaffolds and membranes with living cells and other advanced materials for regenerative biology and medicine. *Analyst* **2013,** *138* (8), 2215-23.
139. Ng, K. E.; Joly, P.; Jayasinghe, S. N.; Vernay, B.; Knight, R.; Barry, S. P.; McComick, J.; Latchman, D.; Stephanou, A., Bio-electrospraying primary cardiac cells: in vitro tissue creation and functional study. *Biotechnol J* **2011,** *6* (1), 86-95.
140. Jayasinghe, S. N., Bio-electrosprays: from bio-analytics to a generic tool for the health sciences. *Analyst* **2011,** *136* (5), 878-90.

141. Li, W.-J.; Laurencin, C. T.; Caterson, E. J.; Tuan, R. S.; Ko, F. K., Electrospun nanofibrous structure: A novel scaffold for tissue engineering. *Journal of Biomedical Materials Research* **2002,** *60* (4), 613-621.
142. Casper, C. L.; Stephens, J. S.; Tassi, N. G.; Chase, D. B.; Rabolt, J. F., Controlling surface morphology of electrospun polystyrene fibers: Effect of Humidity and Molecular Weight in the Electrospinning Process. *Macromolecules* **2004,** *37* (2), 573-578.
143. Niu, H.; Lin, T., Fiber generators in needleless electrospinning. *Journal of Nanomaterials* **2012,** *2012*, 13.
144. Li, D.; Xia, Y., Electrospinning of nanofibers: reinventing the wheel? *Advanced Materials* **2004,** *16* (14), 1151-1170.
145. Jayasinghe, S. N.; Warnes, G.; Scotton, C. J., Bio-electrosprayed living composite matrix implanted into mouse models. *Macromol Biosci* **2011,** *11* (10), 1364-9.
146. Sampson, S. L.; Saraiva, L.; Gustafsson, K.; Jayasinghe, S. N.; Robertson, B. D., Cell electrospinning: An in vitro and in vivo study. *Small* **2014,** *10* (1), 78-82.
147. Shin, M.; Yoshimoto, H.; Vacanti, J. P., In vivo bone tissue engineering using mesenchymal stem cells on a novel electrospun nanofibrous scaffold. *Tissue Eng* **2004,** *10* (1-2), 33-41.
148. Srouji, S.; Ben-David, D.; Lotan, R.; Livne, E.; Avrahami, R.; Zussman, E., Slow-release human recombinant bone morphogenetic protein-2 embedded within electrospun scaffolds for regeneration of bone defect: in vitro and in vivo evaluation. *Tissue Eng Part A* **2011,** *17* (3-4), 269-77.
149. Tillman, B. W.; Yazdani, S. K.; Lee, S. J.; Geary, R. L.; Atala, A.; Yoo, J. J., The in vivo stability of electrospun polycaprolactone-collagen scaffolds in vascular reconstruction. *Biomaterials* **2009,** *30* (4), 583-588.
150. Taboas, J. M.; Maddox, R. D.; Krebsbach, P. H.; Hollister, S. J., Indirect solid free form fabrication of local and global porous, biomimetic and composite 3D polymer-ceramic scaffolds. *Biomaterials* **2003,** *24* (1), 181-194.
151. Sachlos, E.; Reis, N.; Ainsley, C.; Derby, B.; Czernuszka, J. T., Novel collagen scaffolds with predefined internal morphology made by solid freeform fabrication. *Biomaterials* **2003,** *24* (8), 1487-1497.
152. Chia, H. Improvement of 3D printing resolution by the development of shrinkable materials. University of California, eScholarship, 2014.
153. Lee, M.; Wu, B., Recent advances in 3D printing of tissue engineering scaffolds. In *Computer-Aided Tissue Engineering*, Liebschner, M. A. K., Ed. Humana Press: 2012; Vol. 868, pp 257-267.
154. Temple, J. P.; Hutton, D. L.; Hung, B. P.; Huri, P. Y.; Cook, C. A.; Kondragunta, R.; Jia, X.; Grayson, W. L., Engineering anatomically shaped vascularized bone grafts with hASCs and 3D-printed PCL scaffolds. *J Biomed Mater Res A* **2014,** *102* (12), 4317-25.
155. Park, C. H.; Rios, H. F.; Jin, Q.; Bland, M. E.; Flanagan, C. L.; Hollister, S. J.; Giannobile, W. V., Biomimetic hybrid scaffolds for engineering human tooth-ligament interfaces. *Biomaterials* **2010,** *31* (23), 5945-52.
156. Raya-Rivera, A.; Esquiliano, D. R.; Yoo, J. J.; Lopez-Bayghen, E.; Soker, S.; Atala, A., Tissue-engineered autologous urethras for patients who need reconstruction: an observational study. *Lancet* **2011,** *377* (9772), 1175-1182.

157. Raya-Rivera, A. M.; Esquiliano, D.; Fierro-Pastrana, R.; Lopez-Bayghen, E.; Valencia, P.; Ordorica-Flores, R.; Soker, S.; Yoo, J. J.; Atala, A., Tissue-engineered autologous vaginal organs in patients: a pilot cohort study. *Lancet* **2014,** *384* (9940), 329-36.
158. Prevention, C. f. D. C. a., National Center for Health Statistics. Services, U. S. D. o. H. a. H., Ed. Centers for Disease Control and Prevention: CDC/National Center for Health Statistics, 2016.
159. Goldblatt, E. M.; Lee, W.-H., From bench to bedside: the growing use of translational research in cancer medicine. *American Journal of Translational Research* **2010,** *2* (1), 1-18.
160. Liang, X.-J.; Chen, C.; Zhao, Y.; Wang, P. C., Circumventing tumor resistance to chemotherapy by nanotechnology. *Methods in Molecular Biology (Clifton, N.J.)* **2010,** *596*, 467-488.
161. Fletcher, J. I.; Haber, M.; Henderson, M. J.; Norris, M. D., ABC transporters in cancer: more than just drug efflux pumps. *Nat Rev Cancer* **2010,** *10* (2), 147-156.
162. Rivankar, S., An overview of doxorubicin formulations in cancer therapy. *Journal of cancer research and therapeutics* **2014,** *10* (4), 853-8.
163. Ngan, Y.; Gupta, M., A comparison between liposomal and nonliposomal formulations of doxorubicin in the treatment of cancer: An updated review. *Archives of Pharmacy Practice* **2016,** *7* (1), 1-13.
164. Vici, P.; Colucci, G.; Giotta, F.; Sergi, D.; Filippelli, G.; Perri, P.; Botti, C.; Vizza, E.; Carpino, A.; Pizzuti, L.; Latorre, A.; Giannarelli, D.; Lopez, M.; Di Lauro, L., A multicenter prospective phase II randomized trial of epirubicin/vinorelbine versus pegylated liposomal doxorubicin/vinorelbine as first-line treatment in advanced breast cancer. A GOIM study. *Journal of Experimental & Clinical Cancer Research* **2011,** *30* (1), 39.
165. Wasle, I.; Gamerith, G.; Kocher, F.; Mondello, P.; Jaeger, T.; Walder, A.; Auberger, J.; Melchardt, T.; Linkesch, W.; Fiegl, M.; Mian, M., Non-pegylated liposomal doxorubicin in lymphoma: patterns of toxicity and outcome in a large observational trial. *Annals of Hematology* **2015,** *94* (4), 593-601.
166. Makadia, H. K.; Siegel, S. J., Poly Lactic-co-Glycolic Acid (PLGA) as biodegradable controlled drug delivery carrier. *Polymers* **2011,** *3* (3), 1377.
167. Anderson, J. M.; Shive, M. S., Biodegradation and biocompatibility of PLA and PLGA microspheres. *Advanced Drug Delivery Reviews* **1997,** *28* (1), 5-24.
168. Joshi, V. B.; Geary, S. M.; Salem, A. K., Biodegradable particles as vaccine delivery systems: size matters. *Aaps j* **2013,** *15* (1), 85-94.
169. Kang, J.; Wu, F.; Cai, Y.; Xu, M.; He, M.; Yuan, W., Development of Recombinant Human Growth Hormone (rhGH) sustained-release microspheres by a low temperature aqueous phase/aqueous phase emulsion method. *European journal of Pharmaceutical Sciences : official Journal of the European Federation for Pharmaceutical Sciences* **2014,** *62*, 141-7.
170. Zhao, H.; Wu, F.; Cai, Y.; Chen, Y.; Wei, L.; Liu, Z.; Yuan, W., Local antitumor effects of intratumoral delivery of rIL-2 loaded sustained-release dextran/PLGA-PLA core/shell microspheres. *International Journal of Pharmaceutics* **2013,** *450* (1-2), 235-40.

171. Yuan, W.; Liu, Z., Controlled-release and preserved bioactivity of proteins from (self-assembled) core-shell double-walled microspheres. *Int J Nanomedicine* **2012,** *7*, 257-70.
172. Yuan, W.; Zhang, Y.; Wu, F.; Li, H.; Cai, Y.; Zhang, Y.; Han, M.; Jin, T., Preparation of protein-loaded sustained-release microspheres via 'solid-in-oil-in-hydrophilic oil-in-ethanol (S/O/hO/E)' emulsification. *Colloids and Surfaces. B, Biointerfaces* **2010,** *79* (2), 326-33.
173. Deng, C. X.; Xu, Q.; Apfel, R. E.; Holland, C. K., Inertial cavitation produced by pulsed ultrasound in controlled host media. *The Journal of the Acoustical Society of America* **1996,** *100* (2), 1199-1208.
174. Frenkel, V.; Kimmel, E.; Iger, Y., Ultrasound-induced cavitation damage to external epithelia of fish skin. *Ultrasound in Medicine & Biology* **1999,** *25* (8), 1295-1303.
175. Miller, D. L.; Thomas, R. M., Ultrasound contrast agents nucleate inertial cavitation in vitro. *Ultrasound in Medicine & Biology* **1995,** *21* (8), 1059-1065.
176. Doktycz, S.; Suslick, K., Interparticle collisions driven by ultrasound. *Science* **1990,** *247* (4946), 1067-1069.
177. Suslick, K. S. In *Sonoluminescence and sonochemistry*, 1997 IEEE Ultrasonics Symposium Proceedings. An International Symposium (Cat. No.97CH36118), 5-8 Oct 1997; 1997; pp 523-532 vol.1.
178. Gâmbuteanu, C.; Alexe, P., Principles and effects of acoustic cavitation. *The Annals of the University of Dunarea de Jos of Galati. Fascicle VI. Food Technology* **2013,** *37* (2), 9-17.
179. Jang, K. W.; Seol, D.; Ding, L.; Heo, D. N.; Lee, S. J.; Martin, J. A.; Kwon, I. K., Ultrasound-triggered PLGA microparticle destruction and degradation for controlled delivery of local cytotoxicity and drug release. *International Journal of Biological Macromolecules* **2017**.
180. Figueiredo, M.; Esenaliev, R., PLGA Nanoparticles for Ultrasound-mediated gene delivery to solid tumors. *J Drug Deliv* **2012,** *2012*, 767839.
181. Casares, N.; Pequignot, M. O.; Tesniere, A.; Ghiringhelli, F.; Roux, S.; Chaput, N.; Schmitt, E.; Hamai, A.; Hervas-Stubbs, S.; Obeid, M.; Coutant, F.; Métivier, D.; Pichard, E.; Aucouturier, P.; Pierron, G.; Garrido, C.; Zitvogel, L.; Kroemer, G., Caspase-dependent immunogenicity of doxorubicin-induced tumor cell death. *The Journal of Experimental Medicine* **2005,** *202* (12), 1691-1701.
182. Tongu, M.; Harashima, N.; Yamada, T.; Harada, T.; Harada, M., Immunogenic chemotherapy with cyclophosphamide and doxorubicin against established murine carcinoma. *Cancer Immunology, Immunotherapy : CII* **2010,** *59* (5), 769-77.
183. Demaria, S.; Formenti, S. C., Role of T lymphocytes in tumor response to radiotherapy. *Frontiers in Oncology* **2012,** *2*, 95.
184. Choi, Y. W. W. Q. S. H. FDA's Regulatory Science Program for Generic PLA/PLGA-Based Drug Products. https://www.americanpharmaceuticalreview.com/Featured-Articles/339677-FDA-s-Regulatory-Science-Program-for-Generic-PLA-PLGA-Based-Drug-Products/ (accessed May 30th).
185. Dlugi, A. M.; Miller, J. D.; Knittle, J., Lupron* depot (leuprolide acetate for depot suspension) in the treatment of endometriosis: a randomized, placebo-controlled, double-blind study. *Fertility and Sterility* **1990,** *54* (3), 419-427.

186. Bala, I.; Hariharan, S.; Kumar, M. R., PLGA nanoparticles in drug delivery: the state of the art. *Critical Reviews™ in Therapeutic Drug Carrier Systems* **2004,** *21* (5).
187. LUPRON DEPOT [package insert]. North Chicago, IL: AbbVie Inc. **2014**.
188. Crotts, G.; Park, T. G., Protein delivery from poly(lactic-co-glycolic acid) biodegradable microspheres: Release kinetics and stability issues. *Journal of Microencapsulation* **1998,** *15* (6), 699-713.
189. Gu, B.; Burgess, D. J., Chapter 20 - Polymeric materials in drug delivery A2 - Kumbar, Sangamesh G. In *Natural and Synthetic Biomedical Polymers*, Laurencin, C. T.; Deng, M., Eds. Elsevier: Oxford, 2014; pp 333-349.
190. Croll, T. I.; O'Connor, A. J.; Stevens, G. W.; Cooper-White, J. J., Controllable surface modification of poly(lactic-co-glycolic acid) (PLGA) by hydrolysis or aminolysis I: Physical, Chemical, and Theoretical Aspects. *Biomacromolecules* **2004,** *5* (2), 463-473.
191. Hans, M. L.; Lowman, A. M., Biodegradable nanoparticles for drug delivery and targeting. *Current Opinion in Solid State and Materials Science* **2002,** *6* (4), 319-327.
192. Kocbek, P.; Obermajer, N.; Cegnar, M.; Kos, J.; Kristl, J., Targeting cancer cells using PLGA nanoparticles surface modified with monoclonal antibody. *Journal of Controlled Release* **2007,** *120* (1-2), 18-26.
193. Kirby, G. T.; White, L. J.; Rahman, C. V.; Cox, H. C.; Qutachi, O.; Rose, F. R.; Hutmacher, D. W.; Shakesheff, K. M.; Woodruff, M. A., PLGA-based microparticles for the sustained release of BMP-2. *Polymers* **2011,** *3* (1), 571-586.
194. Institute, N. C. Melanoma Treatment (PDQ®)–Patient Version. https://www.cancer.gov/types/skin/patient/melanoma-treatment-pdq#section/all (accessed May 30th).
195. Garbe, C.; Peris, K.; Hauschild, A.; Saiag, P.; Middleton, M.; Bastholt, L.; Grob, J.-J.; Malvehy, J.; Newton-Bishop, J.; Stratigos, A. J.; Pehamberger, H.; Eggermont, A. M., Diagnosis and treatment of melanoma. European consensus-based interdisciplinary guideline; Update 2016. *European Journal of Cancer* **2016,** *63*, 201-217.
196. Rastrelli, M.; Alaibac, M.; Stramare, R.; Chiarion Sileni, V.; Montesco, M. C.; Vecchiato, A.; Campana, L. G.; Rossi, C. R., Melanoma M (Zero): Diagnosis and Therapy. *ISRN Dermatology* **2013,** *2013*, 10.
197. Joshi, V. B. Biodegradable particles as vaccine delivery systems. Doctoral dissertation, The University of Iowa, The University of Iowa's Insitutional Repository, 2014.
198. Lentacker, I.; De Smedt, S. C.; Sanders, N. N., Drug loaded microbubble design for ultrasound triggered delivery. *Soft Matter* **2009,** *5* (11), 2161-2170.
199. Bouakaz, A.; Versluis, M.; de Jong, N., High-speed optical observations of contrast agent destruction. *Ultrasound in Medicine & Biology* **2005,** *31* (3), 391-399.
200. Hernot, S.; Klibanov, A. L., Microbubbles in ultrasound-triggered drug and gene delivery. *Adv Drug Deliv Rev* **2008,** *60* (10), 1153-66.
201. Balazsovits, J. A. E.; Mayer, L. D.; Bally, M. B.; Cullis, P. R.; McDonell, M.; Ginsberg, R. S.; Falk, R. E., Analysis of the effect of liposome encapsulation on the vesicant properties, acute and cardiac toxicities, and antitumor efficacy of doxorubicin. *Cancer Chemotherapy and Pharmacology* **1989,** *23* (2), 81-86.

202. Kreidieh, F. Y.; Moukadem, H. A.; El Saghir, N. S., Overview, prevention and management of chemotherapy extravasation. *World Journal of Clinical Oncology* **2016,** *7* (1), 87-97.
203. Hwang, J. H.; Tu, J.; Brayman, A. A.; Matula, T. J.; Crum, L. A., Correlation between inertial cavitation dose and endothelial cell damage in vivo. *Ultrasound in Medicine & Biology* **2006,** *32* (10), 1611-1619.
204. Kim, I.; Byeon, H. J.; Kim, T. H.; Lee, E. S.; Oh, K. T.; Shin, B. S.; Lee, K. C.; Youn, Y. S., Doxorubicin-loaded highly porous large PLGA microparticles as a sustained- release inhalation system for the treatment of metastatic lung cancer. *Biomaterials* **2012,** *33* (22), 5574-5583.
205. Korosoglou, G.; Hardt, S. E.; Bekeredjian, R.; Jenne, J.; Konstantin, M.; Hagenmueller, M.; Katus, H. A.; Kuecherer, H., Ultrasound exposure can increase the membrane permeability of human neutrophil granulocytes containing microbubbles without causing complete cell destruction. *Ultrasound in Medicine & Biology* **2006,** *32* (2), 297-303.
206. Ellwart, J. W.; Brettel, H.; Kober, L. O., Cell membrane damage by ultrasound at different cell concentrations. *Ultrasound in Medicine & Biology* **1988,** *14* (1), 43-50.
207. Hu, Z.; Lv, G.; Li, Y.; Li, E.; Li, H.; Zhou, Q.; Yang, B.; Cao, W., Enhancement of anti-tumor effects of 5-fluorouracil on hepatocellular carcinoma by low-intensity ultrasound. *Journal of Experimental & Clinical Cancer Research* **2016,** *35* (1), 71.
208. Huebsch, N.; Kearney, C. J.; Zhao, X.; Kim, J.; Cezar, C. A.; Suo, Z.; Mooney, D. J., Ultrasound-triggered disruption and self-healing of reversibly cross-linked hydrogels for drug delivery and enhanced chemotherapy. *Proceedings of the National Academy of Sciences of the United States of America* **2014,** *111* (27), 9762-7.
209. Lentacker, I.; Geers, B.; Demeester, J.; De Smedt, S. C.; Sanders, N. N., Design and evaluation of doxorubicin-containing microbubbles for ultrasound-triggered doxorubicin delivery: cytotoxicity and mechanisms involved. *Molecular Therapy* **2010,** *18* (1), 101-108.
210. Kost, J.; Langer, R., Responsive polymeric delivery systems. *Advanced Drug Delivery Reviews* **2012,** *64, Supplement* (0), 327-341.
211. Iskakov, R. M.; Kikuchi, A.; Okano, T., Time-programmed pulsatile release of dextran from calcium-alginate gel beads coated with carboxy-n-propylacrylamide copolymers. *J Control Release* **2002,** *80* (1-3), 57-68.
212. Zhang, Z.; Qi, X.; Li, X.; Xing, J.; Zhu, X.; Wu, Z., A novel pulsatile drug delivery system based on the physiochemical reaction between acrylic copolymer and organic acid: In vitro and in vivo evaluation. *International Journal of Pharmaceutics* **2014,** *462* (1–2), 66-73.
213. Sundararaj, S. C.; Thomas, M. V.; Dziubla, T. D.; Puleo, D. A., Bioerodible system for sequential release of multiple drugs. *Acta Biomaterialia* **2014,** *10* (1), 115-125.
214. Pacheco, H.; Vedantham, K.; Aniket; Young, A.; Marriott, I.; El-Ghannam, A., Tissue engineering scaffold for sequential release of vancomycin and rhBMP2 to treat bone infections. *Journal of Biomedical Materials Research Part A* **2014,** *102* (12), 4213-4223.

215. Schubert, C.; van Langeveld, M. C.; Donoso, L. A., Innovations in 3D printing: a 3D overview from optics to organs. *The British Journal of Ophthalmology* **2014,** *98* (2), 159-61.
216. Ozbolat, I. T.; Hospodiuk, M., Current advances and future perspectives in extrusion-based bioprinting. *Biomaterials* **2016,** *76*, 321-343.
217. Rattanakit, P.; Moulton, S. E.; Santiago, K. S.; Liawruangrath, S.; Wallace, G. G., Extrusion printed polymer structures: A facile and versatile approach to tailored drug delivery platforms. *International Journal of Pharmaceutics* **2012,** *422* (1–2), 254-263.
218. Goyanes, A.; Buanz, A. B. M.; Hatton, G. B.; Gaisford, S.; Basit, A. W., 3D printing of modified-release aminosalicylate (4-ASA and 5-ASA) tablets. *European Journal of Pharmaceutics and Biopharmaceutics* **2015,** *89*, 157-162.
219. Khaled, S. A.; Burley, J. C.; Alexander, M. R.; Yang, J.; Roberts, C. J., 3D printing of tablets containing multiple drugs with defined release profiles. *International Journal of Pharmaceutics* **2015,** *494* (2), 643-650.
220. Jonathan, G.; Karim, A., 3D printing in pharmaceutics: A new tool for designing customized drug delivery systems. *International Journal of Pharmaceutics* **2016,** *499* (1–2), 376-394.
221. Sun, Y.; Soh, S., Printing tablets with fully customizable release profiles for personalized medicine. *Advanced Materials* **2015,** *27* (47), 7847-7853.
222. Dolati, F.; Yu, Y.; Zhang, Y.; De Jesus, A. M.; Sander, E. A.; Ozbolat, I. T., In vitro evaluation of carbon-nanotube-reinforced bioprintable vascular conduits. *Nanotechnology* **2014,** *25* (14), 145101.
223. Ozbolat, I. T., Bioprinting scale-up tissue and organ constructs for transplantation. *Trends in Biotechnology* **2015,** *33* (7), 395-400.
224. Makadia, H. K.; Siegel, S. J., Poly Lactic-co-Glycolic Acid (PLGA) as biodegradable controlled drug delivery carrier. *Polymers* **2011,** *3* (3), 1377-1397.
225. Lu, J. M.; Wang, X.; Marin-Muller, C.; Wang, H.; Lin, P. H.; Yao, Q.; Chen, C., Current advances in research and clinical applications of PLGA-based nanotechnology. *Expert Review of Molecular Diagnostics* **2009,** *9* (4), 325-41.
226. Lee, K. Y.; Mooney, D. J., Alginate: properties and biomedical applications. *Progress in polymer science* **2012,** *37* (1), 106-126.
227. George, M.; Abraham, T. E., Polyionic hydrocolloids for the intestinal delivery of protein drugs: alginate and chitosan--a review. *J Control Release* **2006,** *114* (1), 1-14.
228. Kim, H.-J.; Lee, H.-C.; Oh, J.-S.; Shin, B.-A.; Oh, C.-S.; Park, R.-D.; Yang, K.-S.; Cho, C.-S., Polyelectrolyte complex composed of chitosan and sodium alginate for wound dressing application. *Journal of Biomaterials Science, Polymer Edition* **1999,** *10* (5), 543-556.
229. Tønnesen, H. H.; Karlsen, J., Alginate in drug delivery systems. *Drug Development and Industrial Pharmacy* **2002,** *28* (6), 621-630.
230. Venkatesan, J.; Bhatnagar, I.; Manivasagan, P.; Kang, K.-H.; Kim, S.-K., Alginate composites for bone tissue engineering: A review. *International Journal of Biological Macromolecules* **2015,** *72*, 269-281.
231. Kong, H. J.; Kaigler, D.; Kim, K.; Mooney, D. J., Controlling rigidity and degradation of alginate hydrogels via molecular weight distribution. *Biomacromolecules* **2004,** *5* (5), 1720-1727.

232. Bouhadir, K. H.; Lee, K. Y.; Alsberg, E.; Damm, K. L.; Anderson, K. W.; Mooney, D. J., Degradation of partially oxidized alginate and its potential application for tissue engineering. *Biotechnol Prog* **2001,** *17* (5), 945-50.
233. Zhang, J.; Wang, Q.; Wang, A., In situ generation of sodium alginate/hydroxyapatite nanocomposite beads as drug-controlled release matrices. *Acta Biomaterialia* **2010,** *6* (2), 445-454.
234. Li, Z.; Ramay, H. R.; Hauch, K. D.; Xiao, D.; Zhang, M., Chitosan–alginate hybrid scaffolds for bone tissue engineering. *Biomaterials* **2005,** *26* (18), 3919-3928.
235. Zhang, Y.; Yu, Y.; Dolati, F.; Ozbolat, I. T., Effect of multiwall carbon nanotube reinforcement on coaxially extruded cellular vascular conduits. *Materials Science & Engineering. C, Materials for Biological Applications* **2014,** *39*, 126-33.
236. Elangovan, S.; D'Mello, S. R.; Hong, L.; Ross, R. D.; Allamargot, C.; Dawson, D. V.; Stanford, C. M.; Johnson, G. K.; Sumner, D. R.; Salem, A. K., The enhancement of bone regeneration by gene activated matrix encoding for platelet derived growth factor. *Biomaterials* **2014,** *35* (2), 737-47.
237. Elangovan, S.; Khorsand, B.; Do, A. V.; Hong, L.; Dewerth, A.; Kormann, M.; Ross, R. D.; Rick Sumner, D.; Allamargot, C.; Salem, A. K., Chemically modified RNA activated matrices enhance bone regeneration. *J Control Release* **2015,** *218*, 22-8.
238. Siegel, S. J.; Kahn, J. B.; Metzger, K.; Winey, K. I.; Werner, K.; Dan, N., Effect of drug type on the degradation rate of PLGA matrices. *European Journal of Pharmaceutics and Biopharmaceutics* **2006,** *64* (3), 287-293.
239. Kiortsis, S.; Kachrimanis, K.; Broussali, T.; Malamataris, S., Drug release from tableted wet granulations comprising cellulosic (HPMC or HPC) and hydrophobic component. *European Journal of Pharmaceutics and Biopharmaceutics* **2005,** *59* (1), 73-83.
240. Lu, P.; Takai, K.; Weaver, V. M.; Werb, Z., Extracellular matrix degradation and remodeling in development and disease. *Cold Spring Harbor Perspectives in Biology* **2011,** *3* (12), 10.1101/cshperspect.a005058 a005058.
241. Brown, M. T.; Bussell, J. K., Medication adherence: WHO Cares? *Mayo Clinic Proceedings* **2011,** *86* (4), 304-314.
242. Arap, W.; Pasqualini, R.; Ruoslahti, E., Cancer treatment by targeted drug delivery to tumor vasculature in a mouse model. *Science* **1998,** *279* (5349), 377-380.
243. Sudimack, J.; Lee, R. J., Targeted drug delivery via the folate receptor. *Advanced Drug Delivery Reviews* **2000,** *41* (2), 147-162.
244. Singh, R.; Lillard, J. W., Nanoparticle-based targeted drug delivery. *Experimental and Molecular Pathology* **2009,** *86* (3), 215-223.
245. Pitt, C. G.; Jeffcoat, A. R.; Zweidinger, R. A.; Schindler, A., Sustained drug delivery systems. I. The permeability of poly (ϵ-caprolactone), poly (DL-lactic acid), and their copolymers. *Journal of Biomedical Materials Research Part A* **1979,** *13* (3), 497-507.
246. Pandey, R.; Sharma, A.; Zahoor, A.; Sharma, S.; Khuller, G. K.; Prasad, B., Poly (dl-lactide-co-glycolide) nanoparticle-based inhalable sustained drug delivery system for experimental tuberculosis. *Journal of Antimicrobial Chemotherapy* **2003,** *52* (6), 981-986.

247. Gultepe, E.; Nagesha, D.; Sridhar, S.; Amiji, M., Nanoporous inorganic membranes or coatings for sustained drug delivery in implantable devices. *Advanced Drug Delivery Reviews* **2010,** *62* (3), 305-315.
248. Do, A.-V.; Akkouch, A.; Green, B.; Ozbolat, I.; Debabneh, A.; Geary, S.; Salem, A. K., Controlled and sequential delivery of fluorophores from 3D printed alginate-PLGA Tubes. *Annals of Biomedical Engineering* **2017,** *45* (1), 297-305.
249. Pan, L.; Liu, J.; He, Q.; Shi, J., MSN-Mediated sequential vascular-to-cell nuclear-targeted drug delivery for efficient tumor regression. *Advanced Materials* **2014,** *26* (39), 6742-6748.
250. Kurkuri, M. D.; Aminabhavi, T. M., Poly(vinyl alcohol) and poly(acrylic acid) sequential interpenetrating network pH-sensitive microspheres for the delivery of diclofenac sodium to the intestine. *Journal of Controlled Release* **2004,** *96* (1), 9-20.
251. Chaudhary, S. S.; Patel, H. K.; Parejiya, P. B.; Shelat, P. K., Chronomodulated drug delivery system of urapidil for the treatment of hypertension. *Int J Pharm Investig* **2015,** *5* (2), 107-13.
252. Wang, C. Y.; Yang, C. H.; Lin, Y. S.; Chen, C. H.; Huang, K. S., Anti-inflammatory effect with high intensity focused ultrasound-mediated pulsatile delivery of diclofenac. *Biomaterials* **2012,** *33* (5), 1547-53.
253. Sinha, V. R.; Bhinge, J. R.; Kumria, R.; Kumar, M., Development of pulsatile systems for targeted drug delivery of celecoxib for prophylaxis of colorectal cancer. *Drug Delivery* **2006,** *13* (3), 221-225.
254. Go, D. P.; Gras, S. L.; Mitra, D.; Nguyen, T. H.; Stevens, G. W.; Cooper-White, J. J.; O'Connor, A. J., Multilayered microspheres for the controlled release of growth factors in tissue engineering. *Biomacromolecules* **2011,** *12* (5), 1494-1503.
255. Kaigler, D.; Wang, Z.; Horger, K.; Mooney, D. J.; Krebsbach, P. H., VEGF scaffolds enhance angiogenesis and bone regeneration in irradiated osseous defects. *Journal of bone and mineral research : the official journal of the American Society for Bone and Mineral Research* **2006,** *21* (5), 735-44.
256. Atluri, K.; Seabold, D.; Hong, L.; Elangovan, S.; Salem, A. K., Nanoplex-mediated co-delivery of fibroblast growth factor and bone morphogenetic protein genes promotes osteogenesis in human adipocyte-derived mesenchymal stem cells. *Molecular Pharmaceutics* **2015,** *12* (8), 3032-3042.
257. Jin, Q.; Wei, G.; Lin, Z.; Sugai, J. V.; Lynch, S. E.; Ma, P. X.; Giannobile, W. V., Nanofibrous scaffolds incorporating PDGF-BB microspheres induce chemokine expression and tissue neogenesis in vivo. *PLoS ONE* **2008,** *3* (3), e1729.
258. Yin, J.; Qiu, S.; Shi, B.; Xu, X.; Zhao, Y.; Gao, J.; Zhao, S.; Min, S., Controlled release of FGF-2 and BMP-2 in tissue engineered periosteum promotes bone repair in rats. *Biomedical Materials (Bristol, England)* **2018,** *13* (2), 025001.
259. Hanafy, A. F.; El-Egaky, A. M.; Mortada, S. A.; Molokhia, A. M., Development of implants for sustained release of 5-fluorouracil using low molecular weight biodegradable polymers. *Drug Discoveries & Therapeutics* **2009,** *3* (6), 287-95.
260. Wolinsky, J. B.; Colson, Y. L.; Grinstaff, M. W., Local drug delivery strategies for cancer treatment: gels, nanoparticles, polymeric films, rods, and wafers. *Journal of controlled release : official journal of the Controlled Release Society* **2012,** *159* (1), 10.1016/j.jconrel.2011.11.031.

261. Yang, Y.; Du, T.; Zhang, J.; Kang, T.; Luo, L.; Tao, J.; Gou, Z.; Chen, S.; Du, Y.; He, J.; Jiang, S.; Mao, Q.; Gou, M., A 3D-Engineered conformal implant releases DNA nanocomplexs for eradicating the postsurgery residual glioblastoma. *Advanced Science* **2017,** *4* (8), 1600491.
262. FDA, Statement by FDA Commissioner Scott Gottlieb, M.D., on FDA ushering in new era of 3D printing of medical products; provides guidance to manufacturers of medical devices. Adminstration, U. S. F. D., Ed. U.S. Department of Health and Human Services: https://www.fda.gov/NewsEvents/Newsroom/PressAnnouncements/ucm587547.htm, 2017.
263. Melchels, F. P. W.; Feijen, J.; Grijpma, D. W., A review on stereolithography and its applications in biomedical engineering. *Biomaterials* **2010,** *31* (24), 6121-6130.
264. Timashev, P. S.; Vedunova, M. V.; Guseva, D.; Ponimaskin, E.; Deiwick, A.; Mishchenko, T. A.; Mitroshina, E. V.; Koroleva, A. V.; Pimashkin, A. S.; Mukhina, I. V.; Panchenko, V. Y.; Chichkov, B. N.; Bagratashvili, V. N., 3D in vitro platform produced by two-photon polymerization for the analysis of neural network formation and function. *Biomedical Physics & Engineering Express* **2016,** *2* (3), 035001.
265. Ulasan, M.; Yavuz, E.; Bagriacik, E. U.; Cengeloglu, Y.; Yavuz, M. S., Biocompatible thermoresponsive PEGMA nanoparticles crosslinked with cleavable disulfide-based crosslinker for dual drug release. *Journal of Biomedical Materials Research Part A* **2015,** *103* (1), 243-251.
266. Herzberger, J.; Niederer, K.; Pohlit, H.; Seiwert, J.; Worm, M.; Wurm, F. R.; Frey, H., Polymerization of ethylene oxide, propylene oxide, and other alkylene oxides: synthesis, novel polymer architectures, and bioconjugation. *Chemical Reviews* **2016,** *116* (4), 2170-2243.
267. Sigma, M. Poly(ethylene glycol) methacrylate. https://www.sigmaaldrich.com/catalog/product/aldrich/409537?lang=en&region=US (accessed June 12th).
268. Veronese, F. M.; Mero, A., The impact of PEGylation on biological therapies. *BioDrugs : Clinical Immunotherapeutics, Biopharmaceuticals and Gene Therapy* **2008,** *22* (5), 315-29.
269. Kasko, A. M. Degradable Poly(ethylene glycol) Hydrogels for 2D and 3D Cell Culture. https://www.sigmaaldrich.com/technical-documents/articles/material-matters/degradable-polyethylene-glycol-hydrogels.html (accessed June 12th).
270. Burdick, J. A.; Anseth, K. S., Photoencapsulation of osteoblasts in injectable RGD-modified PEG hydrogels for bone tissue engineering. *Biomaterials* **2002,** *23* (22), 4315-4323.
271. McCloy, R. A.; Rogers, S.; Caldon, C. E.; Lorca, T.; Castro, A.; Burgess, A., Partial inhibition of Cdk1 in G2 phase overrides the SAC and decouples mitotic events. *Cell Cycle* **2014,** *13* (9), 1400-1412.
272. Gavet, O.; Pines, J., Progressive activation of CyclinB1-Cdk1 coordinates entry to mitosis. *Developmental Cell* **2010,** *18* (4), 533-543.
273. Tucker, B. A.; Mullins, R. F.; Streb, L. M.; Anfinson, K.; Eyestone, M. E.; Kaalberg, E.; Riker, M. J.; Drack, A. V.; Braun, T. A.; Stone, E. M., Patient-specific iPSC-derived photoreceptor precursor cells as a means to investigate retinitis pigmentosa. *eLife* **2013,** *2*, e00824.

274. Tucker, B. A.; Anfinson, K. R.; Mullins, R. F.; Stone, E. M.; Young, M. J., Use of a synthetic xeno-free culture substrate for induced pluripotent stem cell induction and retinal differentiation. *Stem Cells Translational Medicine* **2013,** *2* (1), 16-24.
275. Sabree, I.; Gough, J. E.; Derby, B., Mechanical properties of porous ceramic scaffolds: Influence of internal dimensions. *Ceramics International* **2015,** *41* (7), 8425-8432.
276. Horcajada, P.; Rámila, A.; Pérez-Pariente, J.; Vallet, R.; x; M., Influence of pore size of MCM-41 matrices on drug delivery rate. *Microporous and Mesoporous Materials* **2004,** *68* (1), 105-109.
277. Klose, D.; Siepmann, F.; Elkharraz, K.; Krenzlin, S.; Siepmann, J., How porosity and size affect the drug release mechanisms from PLGA-based microparticles. *International Journal of Pharmaceutics* **2006,** *314* (2), 198-206.
278. Schnieders, J.; Gbureck, U.; Vorndran, E.; Schossig, M.; Kissel, T., The effect of porosity on drug release kinetics from vancomycin microsphere/calcium phosphate cement composites. *Journal of Biomedical Materials Research Part B: Applied Biomaterials* **2011,** *99B* (2), 391-398.
279. Wagner, P. J., Type II photoelimination and photocyclization of ketones. *Accounts of Chemical Research* **1971,** *4* (5), 168-177.
280. Platel, R. H.; Hodgson, L. M.; Williams, C. K., Biocompatible initiators for lactide polymerization. *Polymer Reviews* **2008,** *48* (1), 11-63.
281. Bioengineering, N. I. o. B. I. a. Tissue engineering and regenerative medicine. https://www.nibib.nih.gov/science-education/science-topics/tissue-engineering-and-regenerative-medicine (accessed June 12th).
282. Gattazzo, F.; Urciuolo, A.; Bonaldo, P., Extracellular matrix: A dynamic microenvironment for stem cell niche. *Biochimica et Biophysica Acta (BBA) - General Subjects* **2014,** *1840* (8), 2506-2519.
283. Metavarayuth, K.; Sitasuwan, P.; Zhao, X.; Lin, Y.; Wang, Q., Influence of surface topographical cues on the differentiation of mesenchymal stem cells in vitro. *ACS Biomaterials Science & Engineering* **2016,** *2* (2), 142-151.
284. Stumpf, P. S.; Smith, R. C. G.; Lenz, M.; Schuppert, A.; Müller, F.-J.; Babtie, A.; Chan, T. E.; Stumpf, M. P. H.; Please, C. P.; Howison, S. D.; Arai, F.; MacArthur, B. D., Stem cell differentiation as a non-Markov stochastic process. *Cell Systems* **2017,** *5* (3), 268-282.e7.
285. Chambers, I.; Silva, J.; Colby, D.; Nichols, J.; Nijmeijer, B.; Robertson, M.; Vrana, J.; Jones, K.; Grotewold, L.; Smith, A., Nanog safeguards pluripotency and mediates germline development. *Nature* **2007,** *450*, 1230.
286. Abagnale, G.; Sechi, A.; Steger, M.; Zhou, Q.; Kuo, C.-C.; Aydin, G.; Schalla, C.; Müller-Newen, G.; Zenke, M.; Costa, I. G.; van Rijn, P.; Gillner, A.; Wagner, W., Surface Topography guides morphology and spatial patterning of induced pluripotent stem cell colonies. *Stem Cell Reports* **2017,** *9* (2), 654-666.
287. M.J., D.; M.O., R.; H., J.; S., A.; A.S.G, C., Investigating the limits of filopodial sensing: a brief report using SEM to image the interaction between 10 nm high nano-topography and fibroblast filopodia. *Cell Biology International* **2004,** *28* (3), 229-236.
288. Schellenberg, A.; Joussen, S.; Moser, K.; Hampe, N.; Hersch, N.; Hemeda, H.; Schnitker, J.; Denecke, B.; Lin, Q.; Pallua, N.; Zenke, M.; Merkel, R.; Hoffmann, B.; Wagner, W., Matrix elasticity, replicative senescence and DNA methylation patterns of mesenchymal stem cells. *Biomaterials* **2014,** *35* (24), 6351-6358.

289. Gattazzo, F.; Urciuolo, A.; Bonaldo, P., Extracellular matrix: A dynamic microenvironment for stem cell niche(). *Biochimica et Biophysica Acta* **2014,** *1840* (8), 2506-2519.
290. Abagnale, G.; Steger, M.; Nguyen, V. H.; Hersch, N.; Sechi, A.; Joussen, S.; Denecke, B.; Merkel, R.; Hoffmann, B.; Dreser, A.; Schnakenberg, U.; Gillner, A.; Wagner, W., Surface topography enhances differentiation of mesenchymal stem cells towards osteogenic and adipogenic lineages. *Biomaterials* **2015,** *61*, 316-326.
291. Dalby, M. J.; Gadegaard, N.; Tare, R.; Andar, A.; Riehle, M. O.; Herzyk, P.; Wilkinson, C. D. W.; Oreffo, R. O. C., The control of human mesenchymal cell differentiation using nanoscale symmetry and disorder. *Nat. Mater.* **2007,** *6*, 997.
292. Marco, A.; Ada, C. A. E.; Roman, G.; Jacques, B.; Wolfgang, E.; Martin, K.; Horst, K.; P., S. J., Activation of integrin function by nanopatterned adhesive interfaces. *ChemPhysChem* **2004,** *5* (3), 383-388.
293. Takeuchi, K.; Saruwatari, L.; Nakamura, H. K.; Yang, J. M.; Ogawa, T., Enhanced intrinsic biomechanical properties of osteoblastic mineralized tissue on roughened titanium surface. *J Biomed Mater Res A* **2005,** *72* (3), 296-305.
294. M., A. N.; Iva, P.; L., R. R.; F., M. J., Controlling Cell Behavior Through the Design of Polymer Surfaces. *Small* **2010,** *6* (20), 2208-2220.
295. Sun, H.-B.; Kawata, S., Two-Photon Photopolymerization and 3D lithographic microfabrication. In *NMR • 3D Analysis • Photopolymerization*, Springer Berlin Heidelberg: Berlin, Heidelberg, 2004; pp 169-273.
296. Marino, A.; Filippeschi, C.; Genchi, G. G.; Mattoli, V.; Mazzolai, B.; Ciofani, G., The Osteoprint: A bioinspired two-photon polymerized 3-D structure for the enhancement of bone-like cell differentiation. *Acta Biomaterialia* **2014,** *10* (10), 4304-4313.
297. Evans, M. J.; Kaufman, M. H., Establishment in culture of pluripotential cells from mouse embryos. *Nature* **1981,** *292*, 154.
298. Takahashi, K.; Tanabe, K.; Ohnuki, M.; Narita, M.; Ichisaka, T.; Tomoda, K.; Yamanaka, S., Induction of pluripotent stem cells from adult human fibroblasts by defined factors. *Cell* **2007,** *131* (5), 861-72.
299. Bilic, J.; Izpisua Belmonte, J. C., Concise review: Induced pluripotent stem cells versus embryonic stem cells: close enough or yet too far apart? *Stem Cells* **2012,** *30* (1), 33-41.
300. J., R. H.; E., B. A., Embryonic stem cells. *Cell Proliferation* **2004,** *37* (1), 23-34.
301. Klimanskaya, I.; Chung, Y.; Becker, S.; Lu, S.-J.; Lanza, R., Human embryonic stem cell lines derived from single blastomeres. *Nature* **2006,** *444*, 481.
302. Chun, Y. S.; Chaudhari, P.; Jang, Y.-Y., Applications of patient-specific induced pluripotent stem cells; focused on disease modeling, drug screening and therapeutic potentials for liver disease. *International Journal of Biological Sciences* **2010,** *6* (7), 796-805.
303. Diekman, B. O.; Christoforou, N.; Willard, V. P.; Sun, H.; Sanchez-Adams, J.; Leong, K. W.; Guilak, F., Cartilage tissue engineering using differentiated and purified induced pluripotent stem cells. *Proceedings of the National Academy of Sciences of the United States of America* **2012,** *109* (47), 19172-19177.
304. Wang, A.; Tang, Z.; Park, I.-H.; Zhu, Y.; Patel, S.; Daley, G. Q.; Li, S., Induced pluripotent stem cells for neural tissue engineering. *Biomaterials* **2011,** *32* (22), 5023-5032.

305. Pansky, B., *Review of medical embryology*. Macmillan New York: 1982.
306. Hussein, S. M.; Batada, N. N.; Vuoristo, S.; Ching, R. W.; Autio, R.; Narva, E.; Ng, S.; Sourour, M.; Hamalainen, R.; Olsson, C.; Lundin, K.; Mikkola, M.; Trokovic, R.; Peitz, M.; Brustle, O.; Bazett-Jones, D. P.; Alitalo, K.; Lahesmaa, R.; Nagy, A.; Otonkoski, T., Copy number variation and selection during reprogramming to pluripotency. *Nature* **2011,** *471* (7336), 58-62.
307. Lister, R.; Pelizzola, M.; Kida, Y. S.; Hawkins, R. D.; Nery, J. R.; Hon, G.; Antosiewicz-Bourget, J.; O'Malley, R.; Castanon, R.; Klugman, S.; Downes, M.; Yu, R.; Stewart, R.; Ren, B.; Thomson, J. A.; Evans, R. M.; Ecker, J. R., Hotspots of aberrant epigenomic reprogramming in human induced pluripotent stem cells. *Nature* **2011,** *471*, 68.
308. Tachi, K.; Takami, M.; Sato, H.; Mochizuki, A.; Zhao, B.; Miyamoto, Y.; Tsukasaki, H.; Inoue, T.; Shintani, S.; Koike, T.; Honda, Y.; Suzuki, O.; Baba, K.; Kamijo, R., Enhancement of bone morphogenetic protein-2-induced ectopic bone formation by transforming growth factor-β1. *Tissue Engineering Part A* **2011,** *17* (5-6), 597-606.
309. James, A. W.; LaChaud, G.; Shen, J.; Asatrian, G.; Nguyen, V.; Zhang, X.; Ting, K.; Soo, C., A review of the clinical side effects of bone morphogenetic protein-2. *Tissue Engineering. Part B, Reviews* **2016,** *22* (4), 284-297.
310. Kogut, I.; Roop, D. R.; Bilousova, G., Differentiation of human induced pluripotent stem cells into a keratinocyte lineage. *Methods in Molecular Biology (Clifton, N.J.)* **2014,** *1195*, 1-12.
311. Li, T.; Zhao, H.; Han, X.; Yao, J.; Zhang, L.; Guo, Y.; Shao, Z.; Jin, Y.; Lai, D., The spontaneous differentiation and chromosome loss in iPSCs of human trisomy 18 syndrome. *Cell Death & Disease* **2017,** *8* (10), e3149.
312. Emmajayne, K.; Kate, W.; Nikolaj, G.; J., D. M.; C., O. R. O., Nanotopographical cues augment mesenchymal differentiation of human embryonic stem cells. *Small* **2013,** *9* (12), 2140-2151.
313. Massumi, M.; Abasi, M.; Babaloo, H.; Terraf, P.; Safi, M.; Saeed, M.; Barzin, J.; Zandi, M.; Soleimani, M., The effect of topography on differentiation fates of matrigel-coated mouse embryonic stem cells cultured on PLGA nanofibrous scaffolds. *Tissue Eng Part A* **2012,** *18* (5-6), 609-20.
314. Lapointe, V. L.; Fernandes, A. T.; Bell, N. C.; Stellacci, F.; Stevens, M. M., Nanoscale topography and chemistry affect embryonic stem cell self-renewal and early differentiation. *Advanced Healthcare Materials* **2013,** *2* (12), 1644-50.
315. Wu, C., Focal Adhesion: A focal point in current cell biology and molecular medicine. *Cell Adhesion & Migration* **2007,** *1* (1), 13-18.
316. Anh Tuan, N.; Sharvari, R. S.; Evelyn, K. F. Y., From nano to micro: topographical scale and its impact on cell adhesion, morphology and contact guidance. *Journal of Physics: Condensed Matter* **2016,** *28* (18), 183001.
317. Yao, X.; Peng, R.; Ding, J., Effects of aspect ratios of stem cells on lineage commitments with and without induction media. *Biomaterials* **2013,** *34* (4), 930-939.
318. Kilian, K. A.; Bugarija, B.; Lahn, B. T.; Mrksich, M., Geometric cues for directing the differentiation of mesenchymal stem cells. *Proceedings of the National Academy of Sciences of the United States of America* **2010,** *107* (11), 4872-4877.